Cand1-mediated adaptive exchange mechanism enables variation in F-box protein expression

Xing Liu[1], Justin M. Reitsma[1], Jennifer L. Mamrosh[1], Yaru Zhang[1], Ronny Straube[2*], and Raymond J. Deshaies[1,3,4*#]

[1] Division of Biology and Biological Engineering, California Institute of Technology, Pasadena, CA 91125, USA

[2] Max Planck Institute for Dynamics of Complex Technical Systems, Sandtorstr. 1, D-39106 Magdeburg

[3] Howard Hughes Medical Institute, California Institute of Technology, Pasadena, CA 91125, USA

[4] Amgen, One Amgen Center Way, Thousand Oaks, CA 91320, USA

[*] Correspondences: deshaies@caltech.edu; rstraube@mpi-magdeburg.mpg.de

[#] Lead contact

SUMMARY

SCF ubiquitin ligase assembly is regulated by the interplay of substrate binding, reversible Nedd8 conjugation on Cul1, and the F-box protein (FBP) exchange factors Cand1 and Cand2. Detailed investigations into SCF assembly and function in reconstituted systems and Cand1,2 knockout cells informed the development of a mathematical model for how dynamical assembly of SCF complexes is controlled, and how this cycle is coupled to degradation of an SCF substrate. Simulations predicted an unanticipated hypersensitivity of Cand1/2-deficient cells to FBP expression levels, which was experimentally validated. Together, these and prior observations lead us to propose the adaptive exchange hypothesis, which posits that regulation of the koff of an FBP from SCF by the actions of substrate, Nedd8, and Cand1 molds the cellular repertoire of SCF complexes, and that the plasticity afforded by this exchange mechanism may enable large variations in FBP expression during development and in FBP gene number during evolution.

INTRODUCTION

Ubiquitination plays an essential role in cells and organisms, and is achieved by a cascade of enzymes that activate ubiquitin and promote its conjugation to substrate proteins. Cullin-RING ubiquitin ligases (CRLs) comprise the largest family of E3/ubiquitin ligase enzymes that promote the conjugation step and are typified by the Skp1•Cul1•F-box (SCF) complexes (Deshaies and Joazeiro, 2009; Lydeard et al., 2013). SCFs are modular multisubunit complexes composed of the cullin Cul1, the RING domain protein Rbx1/Roc1/Hrt1, the adapter protein Skp1, and an interchangeable substrate receptor protein containing an F-box motif that binds Skp1. The human genome encodes 69 F-box proteins (FBPs) that can potentially form distinct SCFs, at least 54 of which have been detected (Katayama et al., 2013; Pierce et al., 2013; Chen et al., 2015; Jiang et al., 2016; Kamran et al., 2017; Reitsma et al., 2017). Since the substrate specificity of an SCF is determined by which one of the FBPs is recruited to the Cul1 scaffold, it is critical for cells to assemble and activate a specific SCF when its substrates are present.

SCFs are activated by covalent modification of Cul1 with Nedd8, which is mediated by a dedicated set of conjugation enzymes (Lydeard et al., 2013; Enchev et al., 2015). Nedd8 is removed by the COP9 signalosome (CSN), allowing Cul1 to bind the paralogous regulatory factors Cand1 and Cand2. Upon binding, Cand1 disrupts FBP•Skp1 association and inhibits Nedd8 conjugation (Duda et al., 2011). These features imply that Cand1 and Cand2 are negative regulators of SCFs, but studies of Cand1-deficient cells and organisms suggest it plays a positive role (Bosu et al., 2010; Lo and Hannink, 2006; Feng et al., 2004). To explain this paradox, it was hypothesized that Cand1-mediated recycling of SCF is required for optimal SCF function (Schmidt et al., 2009). Through quantitative kinetic studies of SCF subunit interactions, we previously found that the extremely low dissociation rate of an SCF complex was dramatically increased by Cand1 (Pierce et al., 2013), and Cand1 acts as a protein exchange factor that accelerates the equilibration of Cul1 with multiple FBP•Skp1 modules (Pierce et al., 2013; Zemla et al., 2013; Wu et al., 2013). In a recent study, we showed that the Cand proteins promote assembly of a specific SCF complex in response to generation of its cognate substrate (Reitsma et al., 2017). Despite this progress, there remain important gaps in our knowledge of FBP exchange and its role in substrate degradation, and essentially nothing is known about why such a complex system evolved.

Here, using biophysical methods coupled with phenotypic analysis of Cand-deficient cells and mathematical modeling, we develop a quantitative model for the Cand-fueled exchange cycle and pinpoint the defect in SCF substrate degradation in Cand1/2 double knockout cells. We show that mutant cells could not tolerate overexpression of individual FBPs, providing a simple rationale for the evolution of the exchange mechanism.

RESULTS

Quantitative Characterization of Cul1•Cand1 Assembly and Disassembly

We established a fluorescence resonance energy transfer (FRET) assay to directly measure the kinetic parameters of Cand1•Cul1, which is an essential prerequisite to modeling the SCF assembly/disassembly cycle in living cells–a major goal of this study. We employed Cul1 sortase-tagged at its C-terminus with AMC (Cul1^{AMC}), and Cand1 lacking the first alpha helix and labeled with FlAsH via an N-terminal tetracysteine tag ($^{\text{FlAsH}\Delta\text{H1}}\text{Cand1}$) (Fig 1A). Quenching of AMC fluorescence upon binding of $^{\text{FlAsH}\Delta\text{H1}}\text{Cand1}$ was chased by unlabeled Cand1 (Fig 1A), which confirmed that the FRET signal depended on $^{\text{FlAsH}\Delta\text{H1}}\text{Cand1}$ binding to Cul1^{AMC}•Rbx1.

By monitoring the donor Cul1^{AMC}•Rbx1 fluorescence at varying concentrations of $^{\text{FlAsH}\Delta\text{H1}}\text{Cand1}$, the k_{on} was determined to be 1.7×10^{7} M^{-1} s^{-1} (Fig 1B, S1A). This k_{on} together with the k_{off} of 1.2×10^{-5} s^{-1} we measured previously (Pierce et al., 2013) revealed the K_D for Cand1 assembly with Cul1•Rbx1 to be 0.7 pM. We also measured the association of Cand1 with Cul1•Rbx1 that was preassembled with FBP•Skp1, and the k_{on} was 2.0×10^{6} M^{-1} s^{-1} (Fig 1C, S1B).

Consistent with our previous study (Pierce et al., 2013), the dissociation of the stable Cand1•Cul1•Rbx1 complex was dramatically accelerated by FBP•Skp1 complexes (Fig 1D, 1H, S1F), while Skp1 alone showed a much weaker effect (Fig 1D). Increasing the concentration of FBP•Skp1 led to increased observed rates of Cand1 dissociation from Cul1•Rbx1 (Fig 1E, S1C), and the maximal observed rate, 67 s^{-1} (Fig 1E), represents the k_{off} of Cand1 from the transient Cand1•Cul1•Skp1•FBP complex. Since $^{\text{FlAsH}\Delta\text{H1}}\text{Cand1}$ lacks 14 amino acids from the N-terminus, we tested if this deletion affects the k_{off} of Cand1•Cul1 by comparing the k_{off} of Cand1•Cul1^{AMC}•Rbx1 and $^{\Delta H1}$Cand1•Cul1^{AMC}•Rbx1. In Fig S1D, $^{\Delta H1}$Cand1•Cul1^{AMC}•Rbx1 displayed a two-phase dissociation, with the fast phase k_{off} 21 times higher than for wild type (WT) Cand1. Consistently, a GST pulldown assay suggested the K_D increased ~4.5 fold (Fig S1E). These results suggest that truncation of the N-terminal helix of Cand1 modestly destabilized its binding to Cul1•Rbx1, and the k_{off} of 67 s^{-1} measured in Fig 1E was overestimated by 4.5-21 fold. Since this k_{off} was the only unknown constant in the thermodynamic cycle for Cul1, Cand1 and FBP interactions (Fig 1F), we calculated this constant using the principle of detailed balance (see Fig S4C and Computational method) which yielded a value of 2.9 s^{-1} (Fig 1F).

Goldenberg et al. (2004) showed that deletion of the β-loop of Cand1 (Cand1Δβ) that is predicted to sterically clash with Skp1 allowed a stable Cand1Δβ •Cul1•Skp1 complex to form. We confirmed this observation using both FRET (Fig 1G) and pulldown assays (Fig S1G). Skp1ΔΔ•Skp2, which lacks a loop in Skp1 predicted to clash with the β-loop of Cand1, failed to disrupt the Cand1•Cul1 complex (Fig 1H, S1F). This was not due to a failure to bind, because stable ^{GST}Cand1•Cul1•Skp1ΔΔ could form *in vitro* (Fig S1G). These results suggest that Cand1, Cul1, and Skp1•FBP form a ternary complex that is exceptionally unstable due to clash of the Skp1 loop with the Cand1 β-loop. As a consequence, the ternary complex rapidly decays to yield either binary complex, each of which is stable (Fig 1F). This mimics the behavior of Ras, Ras-GEF, and guanine nucleotides (Klebe et al., 1995; Goody and Hofmann-Goody, 2002; Guo et al., 2005).

Cand1/2 promote efficient degradation of SCF substrates

To explore the role of Cand1 under physiological conditions, we generated CRISPR knock-out human cell lines. Because Cand1 knockdown enhanced the recovery of Cand2 in ^{FLAG}Cul1 immunoprecipitates (IP) (Fig S2A), we knocked out both Cand1 and Cand2 using pairs of CRISPR nickases to minimize off-target effects (Fig S2B) (Ran et al., 2013; Shen et al., 2014). We generated Cand1 or Cand2 single knockout (KO) cells (Fig S2C), and three independent double knockout (DKO) cells (Fig S2D).

We first looked at TNFα-induced degradation of IκBα by $SCF^{\beta\text{-}TrCP}$ (Spencer et al., 1999; Kroll et al., 1999), and we found that the $t_{1/2}$ for IκBα elimination was nearly tripled in the DKO lines compared with the WT (Figs 2A, 2C, S2E). To confirm that the deficiency in IκBα degradation was due to the absence of Cand1, we integrated a single copy of the *CAND1* gene into the DKO cell genome through Flp recombinase-mediated insertion. When the Cand1 transgene was induced by tetracycline in DKO cells (Fig 2B), the IκBα degradation defect was fully rescued (Fig 2A, C). Furthermore, IκBα degradation was unaffected in Cand2 KO cells, whereas Cand1 KO had an intermediate effect (Fig S2F), suggesting that Cand1 promotes efficient degradation of IκBα but can be partially substituted by Cand2 upon its deletion. Reduced degradation of IκBα in DKO cells was not due to lack of phosphorylations that trigger IκBα degradation (note the upshift of IκBα in DKO cells at ≥20’ in Fig 2A), nor the lack of β-TrCP (Fig 2B). Also, ubiquitination of phosphorylated IκBα (pIκBα) was greatly reduced in DKO cells relative to WT cells (Fig 2D), suggesting that prolonged IκBα degradation in DKO cells was due to decreased ubiquitination.

Cand1/2 is required for rapid assembly of new SCF in response to substrate availability

Because pIκBα is a substrate of $SCF^{\beta\text{-}TrCP}$, we measured the level of endogenous $SCF^{\beta\text{-}TrCP}$ complex before and after TNFα treatment (Fig 2E). We tagged endogenous Cul1 with a 3xFLAG tag using CRISPR, and we lysed the cells in buffer containing recombinant Cul1•Rbx1 ‘sponge’ protein at 100x excess over endogenous ^{3xFLAG}Cul1, which blocks the Cand-mediated exchange of FBPs and thus preserves endogenous SCF complexes (Reitsma et al., 2017). In agreement with Reitsma et al. (2017), we found that the level of β-TrCP co-IP’d with endogenous ^{3xFLAG}Cul1 was higher in unstimulated DKO cells than in WT cells (Fig 2F). However, after 10-min TNFα treatment, co-IP’d β-TrCP was increased by 80% in the WT cells, but was unchanged in the DKO cells (Fig 2F). These results suggest that when pIκBα substrate appears, new $SCF^{\beta\text{-}TrCP}$ are quickly assembled in a Cand1/2-dependent manner.

We further analyzed the assembly of pIκBα•β-TrCP•Cul1 in cells expressing tetracycline-induced ^{3xFLAG}IκBα. We first looked at the interaction of ^{3xFLAG}pIκBα with β-TrCP, by immobilizing ^{3xFLAG}pIκBα, deubiquitinating the immobilized protein with Usp2, and quantifying the ratio β-TrCP:pIκBα (Fig 2G), and we found that the DKO cells had no deficiency in forming the pIκBα•β-

TrCP complex (Fig 2H). In a parallel assay, we used the Nedd8 E1 inhibitor MLN4924 (Soucy et al., 2009) to prevent the ubiquitination of pIκBα (Fig S2G-H), and confirmed that pIκBα•β-TrCP formation was not affected in DKO cells (Fig S2I). Finally, we analyzed the association of Cul1 with the pIκBα•β-TrCP complex. Whereas Cul1, especially neddylated Cul1, was efficiently recruited to pIκBα•β-TrCP in WT cells, this recruitment was reduced to 40% in DKO cells (Fig 2H). These results suggest that substrates can bind both free and Cul1-bound FBPs, and the lower degradation rate of IκBα in DKO cells is due to inefficient recruitment of pIκBα•β-TrCP to Cul1, a process that requires the exchange activity of Cand1.

Cand1 stabilizes Cul1•Dcn1

Interestingly, Cul1-bound Dcn1, the E3 of Nedd8, was detected only in WT cells (Fig 3A). Since this could be due to potential difference in Cul1 neddylation status in WT vs. DKO cells, we treated the cells with MLN4924. Again, we could detect Cul1•Dcn1 only in the WT cells (Fig 3A). A prior report established that Cand1, Cul1, and Dcn1 can form a ternary complex (Kim et al., 2008). Unexpectedly, we showed here that Cand1 strongly promotes binding of Dcn1 to Cul1•^{GST}Rbx1 *in vitro* (Fig 3B). This stabilization could be sustained by the N-terminal half of Cand1 (Fig 3B), which binds the C-terminal domain of Cul1 where Dcn1 also binds. Since Cand1 and Dcn1 formed a complex only in the presence of Cul1•Rbx1 (Fig S2J), this stabilization effect is likely due to a conformational change in the C-terminal domain of Cul1 and/or Rbx1 induced by the binding of Cand1 (Fig S2K). We further quantified that Cand1 increased the ^{GST}Dcn1•Cul1 level by 2.9 fold under a specific pulldown condition (Fig 3C). This result together with the known K_D of Dcn1•Cul1 (Monda et al., 2013) suggests that Cand1 changed the K_D of Dcn1•Cul1 from 1.8 μM to 0.05 μM (Fig 3D), which we validated in additional pulldown assays (Fig S3A).

Since Cand1 strongly inhibited Cul1 neddylation *in vitro* and this inhibition was counteracted by FBPs (Pierce et al., 2013), we set up a competitive neddylation assay to test the counter-intuitive prediction that Cand1-bound Cul1 should be a better neddylation substrate than free Cul1 when FBPs are present. Since the k_{off} of Cand1•Cul1•Rbx1 is low, we mixed equimolar free Cul1^{TAMRA}•Rbx1 with Cand1-bound Cul1^{FAM}•Rbx1, or *vice versa*, incubated the mixture with a limiting amount of Dcn1, then triggered neddylation by adding DKO cell lysate supplemented with recombinant FBPs, and determined the neddylation status of Cul1^{TAMRA} and Cul1^{FAM} individually (Fig 3E). Consistent with the notion that Cand1 stabilized Dcn1•Cul1•Rbx1 and Dcn1 significantly increases the speed of neddylation (Fig S3B) (Monda et al., 2013; Scott et al., 2014), Cand1-bound Cul1 showed up to 50% more neddylation than free Cul1 (Fig 3F), an effect that only occurred when FBPs were present (Fig S3C).

Though Cand1-bound Cul1 cannot be neddylated, formation of Cand1•Cul1•Rbx1•Dcn1 enables immediate neddylation of Cul1 upon removal of Cand1 by FBPs, such that an SCF would be "born" in a neddylated state that is resistant to disassembly by Cand1 and is primed to ubiquitinate substrate. Indeed, when neddylation occurred, more Cand1•Cul1 was dissociated and more SCF was assembled (Fig 3G), and this change occurred over time while neddylation proceeded (Fig S3D). Altogether, these results suggest that Cand1 helps recruit neddylation enzymes to Cul1 such that the formation of an SCF is directly coupled to its activation.

Computational model of the SCF cycle

To understand the impact of SCF assembly and disassembly on the degradation of SCF substrates we developed a deterministic mathematical model based on mass-action equations (Fig 4A and "Computational method" in STAR Methods). To model the SCF$^{\beta\text{-TrCP}}$-mediated degradation of IκBα we considered two populations of F-box proteins: one that represents β-TrCP and another one that accounts for all other F-box proteins in the cell. To parametrize our model we used data that we and others have collected on the rate constants of the various processes considered in the model as well as on the cellular concentrations of SCF components and factors that promote the SCF cycle (Pierce et al., 2013; Mosadeghi et al., 2016; Bennett et al., 2010; Reitsma et al., 2017). We specifically incorporated our observations that Cand1 and Dcn1 exhibit positive cooperativity when binding to Cul1•Rbx1 (Fig 3D) and that Dcn1 stabilizes the Cand1•Cul1•Rbx1 complex in the presence of Skp1•FBP by up to 40% (Fig S3E).

Altogether, our model contains 54 state variables and 35 parameters of which 22 were either directly measured or adapted from previous publications. From the 13 remaining parameters 8 were estimated based on the known value of measured quantities leaving only 5 parameters which had to be estimated from experiments. To fit the model, we chose the following subset of steady state and transient measurements: % of Cul1 bound to Cand1 in WT (Fig 4B), half-life ($t_{1/2}$) for IκBα degradation in WT and DKO (Fig 4C), % of β-TrCP bound to Cul1 upon substrate addition (Fig 4D) and % of Cul1 conjugated to Nedd8 in WT and DKO (Fig 4E).

Our model correctly anticipates the impact of perturbations to the Nedd8–Cand1 cycle on Cul1 assembly state. For example, 100% of Cul1 is predicted to assemble with Skp1 in DKO cells (Fig 4B) in agreement with observations based on selected reaction monitoring mass spectrometry (SRM-MS; Reitsma et al., 2017). Likewise, inhibition of Nedd8 conjugation by MLN4924 is predicted to increase the fraction of Cul1 bound to Cand1 while that of Cul1 bound to Skp1•FBP is predicted to decline (Fig 4B), which is also consistent with results from SRM-MS (Reitsma et al., 2017; the lower values reported by these authors arise from their estimate that 16% of Cul1 was not bound to either Cand1 or Skp1).

To simulate TNFα-induced degradation of IκBα via $SCF^{\beta\text{-TrCP}}$, we first determined the following parameters: (i) the rate of IκBα phosphorylation (by following the shift of the IκBα band in the presence of the ubiquitination inhibitor MLN4924) (Fig S3F), (ii) the cellular concentrations of β-TrCP (64 nM) and IκBα (650 nM) determined by quantitative western blotting (Fig S3G-H), and (iii) the k_{off} of pIκBα•β-TrCP in cell lysate (3.3×10^{-5} s^{-1}; Fig S3I-K) as determined by competitive displacement. This last measurement was quite surprising because prior experiments with a phosphopeptide containing a related degron suggested an off rate in the range of 0.1 sec^{-1} (Saha and Deshaies, 2008). Using these values for model fitting, we obtained the $t_{1/2}$ values for IκBα degradation in WT cells (23min) and in DKO cells (46min) which were similar to those determined empirically (Fig 2C). Importantly, the model correctly predicted the surprising observation that re-expression of Cand1 in the DKO cells at 13% of the WT level (as shown for DKO22 in Fig 2B) restored the $t_{1/2}$ of IκBα degradation to the WT level (Fig 4C). Previous analysis of a mathematical model focusing on the Cand1 cycle suggested that the U-shaped dose-response curve for Cand1

(Fig. 4C, lower panel) results from a trade-off between high SCF ligase activity at low Cand1 concentration and fast F-box exchange at high Cand1 concentration (Straube et al., 2017). One of the predictions of that model is that the presence of substrate would favor the assembly of the corresponding SCF ligase which is precisely what we observed in WT cells (Fig 2F; Reitsma et al. 2017). Interestingly, we obtained the same effect (~1.7-fold increase in the level of β-TrCP bound to Cul1) with our model when simulating the formation of pIκBα using the estimated parameters (Fig 4D). Together, these observations suggest that our model, though it omits much of the complexity that exists in cells (e.g. spatial inhomogeneity and de-novo synthesis of SCF components and accessory proteins), nevertheless captures essential features of the SCF cycle making it effective in predicting both steady-state and dynamic properties of the SCF system in WT cells and in response to genetic and chemical perturbations.

Cellular role of Cand1 revealed by simulations and experimental perturbations

To probe the strength of our model in predicting responses to new perturbations, we simulated the effect of varying the concentration of SCF components on the kinetics of substrate degradation, and compared the results with those obtained empirically. We first increased the Cul1 level in the model, which yielded two predictions: 1) Cul1 overproduction led to a reduction in Cul1 neddylation in both WT and DKO cells (Fig 4E); 2) the $t_{1/2}$ of IκBα in WT and DKO cells overproducing Cul1 became identical and equaled that in WT cells (Fig 4F). Consistent with these predictions, overproduction of ^{3xFLAG}Cul1 did not affect the $t_{1/2}$ of IκBα in WT cells but restored a normal $t_{1/2}$ in DKO cells (Fig 5A), and resulted in reduced neddylation of both Cul1 and Cul4a (Fig 5B). Next, we wondered how increasing the β-TrCP level would affect substrate degradation. Consistent with experiments (Fig 5C, S5E) we found that increased levels of β-TrCP had no significant impact on the $t_{1/2}$ for IκBα in either WT or DKO cells (Fig 4F).

To understand why the $t_{1/2}$ of IκBα in DKO cells was rescued by overproducing Cul1 but not β-TrCP, we probed the assembly status of SCF$^{β\text{-TrCP}}$. Using Cul1•^{GST}Rbx1 “sponge” protein as a bait to capture unbound Skp1•β-TrCP from the cells (Fig 5D), we first found that when Cul1 was overproduced, the amount of free β-TrCP was reduced by 80% in the DKO cells (Fig 5E, S5F), suggesting that almost all β-TrCP was assembled with Cul1, and thus pIκBα was able to access active SCF without relying on the exchange activity of Cand1/2. Second, we quantified the % of β-TrCP bound to endogenous Cul1. Whereas the total amount of SCF$^{\beta\text{-TrCP}}$ was increased upon β-TrCP overproduction (Fig S5G), the percent of β-TrCP assembled into an SCF complex was not (Fig 5F, G). Thus, despite there being more SCF$^{\beta\text{-TrCP}}$, pIκBα was similarly partitioned between pools of SCF$^{\beta\text{-TrCP}}$ and free β-TrCP. For the ~50% of pIκBα molecules in DKO cells that initially bound free β-TrCP, their degradation required dissociation and re-equilibration with the total pool of β-TrCP, which was slow (Fig S3I-J). This explains why DKO cells could contain an elevated level of SCF$^{\beta\text{-TrCP}}$ (Fig 2F) but continue to exhibit a reduced rate of IκBα degradation.

Cand1/2 buffer changes in the expression level of F-box proteins

A major conundrum that emerged from the interplay between model predictions and experiments was the finding that Cul1 overexpression rescued the degradation defect of DKO cells. This begs the question of why such a complex system of FBP exchange exists when similar substrate degradation rates could be achieved by simply increasing the level of Cul1? Remarkably, a hint to resolving this conundrum came from the matrix of normalized response coefficients (Fig S5B) that we computed to quantify the impact of selected model parameters on the experimentally accessible quantities of interest such as the fraction of neddylated Cul1 or the $t_{1/2}$ of substrate. Strikingly, the total FBP concentration was one of the two most sensitive parameters which were predicted to have a strong effect on the substrate $t_{1/2}$ in DKO cells, but not in WT cells. Consistent with this prediction, expression of ^{HA}Fbxo6 in DKO cells through lentiviral infection further increased the $t_{1/2}$ of IκBα by ~40% (Fig 6A, S6A), and decreased the level of SCF$^{\beta\text{-TrCP}}$ (Fig S6C), without altering levels of β-TrCP and Skp1 (Fig S6B). Similarly, cyclin E and p27, which are substrates of SCF$^{\text{Fbxw7}}$ and SCF$^{\text{Skp2}}$, respectively, were also stabilized in DKO cells with overproduced Fbxo6 (DKO$^{\text{Fbxo6}}$; Fig 6B).

When we immunoprecipitated (IP) ^{HA}Fbxo6 in the presence of the Cul1•^{GST}Rbx1 “sponge”, the amount of endogenous Cul1 co-IP’d with ^{HA}Fbxo6 was dramatically increased in the DKO$^{\text{Fbxo6}}$ cells, and therefore, the amount of Cul1 available for the remaining FBP pool was reduced by > 50%

(Fig 6C). More strikingly, cell proliferation of DKO^{Fbxo6} cells slowed dramatically and the cells displayed abnormal morphology and inviability (Fig 6D, S6D-E), which were not observed in WT^{Fbxo6} cells (Fig 6D, S6D), in DKO^{Fbxo6} cells that re-expressed Cand1 (Fig 6C-D), when the F-box motif of overexpressed Fbxo6 was deleted (Fbxo6$^{\Delta Fbox}$) or when Fbxl16 that forms Skp1•Fbxl16 incapable of binding to Cul1 (Honarpour et al., 2014) was overexpressed (Fig 6D, S6F-G). Consistently, the increased doubling time in DKO^{Fbxo6} cells was partially rescued by overexpression of Cul1 (Fig 6E), suggesting that the defects in DKO^{Fbxo6} cells were at least partially due to the sequestration of Cul1 by ^{HA}Fbxo6. Moreover, the increased cell doubling time and the depletion of the free Cul1 pool were also observed in DKO cells overexpressing Skp2, or Skp2 with its substrate binding region deleted (Skp2$^{\Delta LRR}$) (Fig 6F, S6H-J), suggesting the observed defects in FBP-overexpressing DKO cells were not due to altered stability of substrate proteins. In agreement with the dramatic reduction in cell proliferation, DKO$^{Skp2\Delta LRR}$ cells exhibited increased levels of cleaved PARP, a marker for apoptosis (Fig 6G).

DISCUSSION

In this study, we expand upon our prior work (Pierce et al., 2013) to devise a kinetic model for the Cand1-mediated cycle of SCF assembly and disassembly. Consistent with the demonstrated substrate receptor exchange factor (SREF) activity of Cand1, we show that the degradation of SCF substrates is inefficient in Cand1/2 DKO human cells. We propose that this defect arises because substrates bind equivalently to FBPs regardless of whether they are assembled with Cul1 or not. In WT cells, this is immaterial, because for at least some substrates (e.g. pIκBα), a Skp1•β-TrCP•pIκBα complex gains access to Cul1 within a few minutes through dynamic assembly/disassembly of SCFs (Fig 7; see below), which is much faster than the dissociation of pIκBα from β-TrCP (Fig S3I-J). But this is not the case in DKO cells, where the pIκBα bound to free β-TrCP can access Cul1 only through successive rounds of dissociation and re-equilibration with the entire pool of β-TrCP molecules, which is expected to be very slow. An implication of this is that in WT cells the degradation rate of a substrate should not be related to the percent assembly of its FBP because of the rapid flux of SCF assembly/disassembly, whereas in DKO cells, which have a static complement of SCFs, there should be a direct correlation between these parameters. Indeed, there is remarkable agreement between the fraction of pIκBα•β-TrCP not associated with Cul1 in DKO cells, and the fold defect in degradation of IκBα, suggesting that inefficient access of substrate to Cul1 is the major deficiency of DKO cells. Consistent with this argument, slower degradation of IκBα in DKO cells was rescued by overexpression of Cul1, which drove assembly of almost all β-TrCP into an SCF, rendering it independent of Cand1/2.

Prior work had suggested that Cand1 is not important for regulation of SCF in human cells (Bennett et al., 2010). Given that low (13%) re-expression of Cand1 fully rescued the deficiency of IκBα degradation in DKO cells, and that Cand2 partially compensated for the Cand1 KO, our data suggest that RNAi underestimates the significance of Cand-mediated exchange in cells.

Cand1, Nedd8 and CSN cooperatively regulate the rapid cycling of Cul1

Using the kinetic parameters for the Cul1 assembly/disassembly cycle, coupled with quantitative measurements of SCF protein and substrate levels in cells reported here and elsewhere (Bennett et al., 2010; Reitsma et al., 2017), we developed a mathematical model that allowed us to study the dynamics of SCF assembly and SCF substrate degradation. Our model accurately predicts the effect of Cand1/2 DKO on IκBα degradation and recapitulates the general features of the steady-state architecture of the SCF network and how it changes in DKO cells and upon inhibition of neddylation. Strikingly, the model reveals that with no bound substrate, Cul1 progresses through an entire exchange cycle with an average time of 55 s (Fig 7A, S5D). In agreement with this prediction, chemical ablation of neddylation or deneddylation resulted in conversion of Cul1 to fully deneddylated or neddylated species, respectively, with a $t_{1/2}$ of 54-90 s (Fig 7B-C). Given the molecular ratio of Skp1:Cul1 (Reitsma et al., 2017), an F-box protein should cycle through an SCF complex every ~4 minutes. The rapid pace of this cycle allows a cell to remodel its network of SCFs far faster than could be achieved by regulated transcription or translation.

The key gate in our model is substrate occupancy. If an SCF is born with no substrate, it can immediately enter the exchange cycle. If it contains bound substrate, it persists until the substrate is degraded. Then, CSN binds and removes Nedd8, and the SCF is either disrupted by

Cand1 or re-neddylated by Dcn1. Because Cand1 binds Cul1 faster than Dcn1 and Dcn1 prefers Cand1•Cul1 to Cul1, we predict that re-neddylation is discouraged and the SCF proceeds to the exchange state. Removal of Skp1•FBP from Cul1 by Cand1 establishes a substantial reservoir of Cand1•Cul1•Dcn1 (up to 42% of the total Cul1; Reitsma et al., 2017) that is primed to form new, active SCFs by drawing from the pool of Skp1•FBPs.

From a broader perspective, the mechanism that drives the SCF cycle resembles that of a Brownian ratchet which converts random (undirected) motion into directed motion through input of energy (Peskin et al., 1993). In the SCF cycle the "Brownian motion" is provided by the Cand1-mediated exchange of FBPs. Input of energy, which enforces directionality, is provided by neddylation, which prevents re-binding of Cand1 to a newly-formed, neddylated SCF.

The Adaptive Exchange Hypothesis

The degradation defect of cells lacking the Cand SREFs was compensated by overexpression of Cul1, such that the vast majority of FBPs were assembled with Cul1 and thus there was no need for an exchange mechanism to link substrates to Cul1. This begs the question, why does the exchange mechanism exist? Both the mathematical model and experimental observations converged on a simple explanation: Cand-mediated exchange renders the SCF system tolerant of large changes in the expression of individual FBPs. Notably, bioinformatics analyses revealed that such large changes occur routinely during development (Fig S7). This could explain why the multicellular organism Arabidopsis is dramatically perturbed by disruption of Cand function (Cheng et al., 2004; Chuang et al., 2004; Feng et al., 2004), whereas cultured cells and single-celled yeasts are not (Liu et al., 2009; Zemla et al., 2013). If it were not for the Cand system, cells would require counting mechanisms to ensure that the total level of Cul1 was adequate to saturate all available Skp1•FBP modules. Having a system in which all SCF enzymes were always assembled and active could create other problems, especially considering the millisecond rate at which SCF enzymes can initiate and extend ubiquitin chains (Pierce et al., 2009; Scott et al., 2016). The exchange mechanism, by creating a delay between substrate binding to an FBP and its assembly into an active SCF, may have the side benefit of increasing the specificity of the system by setting a ceiling on the maximal k_{off} value of a substrate.

At its heart, the assembly/disassembly cycle is controlled by the k_{off} of substrate from an active SCF complex. The molecular logic of the SCF cycle resembles the control of microtubule networks by dynamic instability (Kirschner and Mitchison, 1986). In that case, individual microtubules sample the cytoplasm through constant, randomly-directed growth and shrinkage. Formation of favorable contacts retards the k_{off} of tubulin subunits, thereby stabilizing the microtubule and driving morphogenesis of a mitotic spindle. In the case of SCFs, the same Darwinian process of variation-selection occurs, but instead of enabling morphogenesis of a specific structure, it controls the repertoire of assembled SCFs such that the cell is biased to accumulate those that are needed at a given time. We refer to this mechanism as 'adaptive exchange'. It is adaptive both in a functional, biochemical sense at the cellular and organismal levels as described here, as well as in an evolutionary sense. This exchange mechanism could enable expansion/contraction of FBP gene repertoires without the maladaptive effects that would occur in a system dependent on stoichiometric Cul1. Duplicated FBP genes could then diverge and acquire new functions beneficial to the organism. This could be the basis for massive variations in FBP gene number found in different organisms (Xu et al., 2009; Srinivasan et al., 2013).

ACKNOWLEDGEMENTS

We thank Brenda Schulman, Ning Zheng, William den Besten for gifts of reagents, Novartis for providing the CSN5i-3 compound, Shu-Ou Shan for sharing instruments, Lea Goentoro and Noah Olsman for insightful discussion on the mathematical model, Robert J. Flassig for discussions on parameter estimation and all the members of the Deshaies lab for helpful discussions. XL is a fellow of The Jane Coffin Childs Memorial Fund for Medical Research (JCCMF), and this investigation has been aided by a grant from JCCMF. JMR is supported by F32 grant GM112308 from NIH. JLM is supported by Life Sciences Research Foundation. RJD was an investigator of the Howard Hughes Medical Institute (HHMI), and this work was supported in part by HHMI and NIH GM065997 to RJD.

AUTHOR CONTRIBUTIONS

Conceptualization, X.L., R.S., R.J.D.; Methodology and Investigation, X.L., J.M.R, Y.Z., J.L.M.; Methodology and Software, R.S.; Writing, X.L, R.S., R.J.D; Supervision, X.L, R.S., R.J.D; Funding Acquisition, X.L., J.M.R., R.J.D..

DECLARATION OF INTERESTS

Raymond J. Deshaies is an employee and shareholder of Amgen.

REFERENCE

Bennett, E.J., Rush, J., Gygi, S.P., and Harper, J.W. (2010). Dynamics of cullin-RING ubiquitin ligase network revealed by systematic quantitative proteomics. Cell 143, 951-965.

Bosu, D.R., Feng, H., Min, K., Kim, Y., Wallenfang, M.R., and Kipreos, E.T. (2010). C. elegans CAND-1 regulates cullin neddylation, cell proliferation and morphogenesis in specific tissues. Developmental biology 346, 113-126.

Chen, W., Xiong, S., Li, J., Li, X., Liu, Y., Zou, C., and Mallampalli, R.K. (2015). The ubiquitin E3 ligase SCF-FBXO24 recognizes deacetylated nucleoside diphosphate kinase A to enhance its degradation. Molecular and cellular biology 35, 1001-1013.

Cheng, Y., Dai, X., and Zhao, Y. (2004). AtCAND1, a HEAT-repeat protein that participates in auxin signaling in Arabidopsis. Plant Physiol 135, 1020-1026.

Chuang, H.W., Zhang, W., and Gray, W.M. (2004). Arabidopsis ETA2, an apparent ortholog of the human cullin-interacting protein CAND1, is required for auxin responses mediated by the SCF(TIR1) ubiquitin ligase. The Plant cell 16, 1883-1897.

Cleland, W.W. (1975). Partition analysis and the concept of net rate constants as tools in enzyme kinetics. Biochemistry 14, 3220-3224.

Deshaies, R.J., and Joazeiro, C.A. (2009). RING domain E3 ubiquitin ligases. Annual review of biochemistry 78, 399-434.

Duda, M.D., Scott, D.C., Calabrese, M.F., Zimmerman, E.S., Zheng, N., Schulman, B.A. (2011). Structural regulation of cullin-RING ubiquitin ligase complexes. Curr Opin Struct Biol 21, 257-264

Emberley, E.D., Mosadeghi, R., and Deshaies, R.J. (2012). Deconjugation of Nedd8 from Cul1 is directly regulated by Skp1-F-box and substrate, and the COP9 signalosome inhibits deneddylated SCF by a noncatalytic mechanism. The Journal of biological chemistry 287, 29679-29689.

Enchev, R.I., Schulman, B.A., and Peter, M. (2015). Protein neddylation: beyond cullin-RING ligases. Nature reviews Molecular cell biology 16, 30-44.

Enchev, R.I., Scott, D.C., da Fonseca, P.C., Schreiber, A., Monda, J.K., Schulman, B.A., Peter, M., and Morris, E.P. (2012). Structural basis for a reciprocal regulation between SCF and CSN. Cell Rep 2, 616-627.

Feng, S., Shen, Y., Sullivan, J.A., Rubio, V., Xiong, Y., Sun, T.P., and Deng, X.W. (2004). Arabidopsis CAND1, an unmodified CUL1-interacting protein, is involved in multiple developmental pathways controlled by ubiquitin/proteasome-mediated protein Degradation. The Plant cell 16, 1870-1882.

Goldenberg, S.J., Cascio, T.C., Shumway, S.D., Garbutt, K.C., Liu, J., Xiong, Y., and Zheng, N. (2004). Structure of the Cand1-Cul1-Roc1 complex reveals regulatory mechanisms for the assembly of the multisubunit cullin-dependent ubiquitin ligases. Cell 119, 517-528.

Goody, R.S., and Hofmann-Goody, W. (2002). Exchange factors, effectors, GAPs and motor proteins: common thermodynamic and kinetic principles for different functions. Eur Biophys J 31, 268-274.

Guo, Z., Ahmadian, M.R., and Goody, R.S. (2005). Guanine nucleotide exchange factors operate by a simple allosteric competitive mechanism. Biochemistry 44, 15423–15429.

Heckman, K.L., and Pease, L.R. (2007). Gene splicing and mutagenesis by PCR-driven overlap extension. Nature protocols 2, 924-932.

Honarpour N., Rose C.M., Brumbaugh J., Anderson J., Graham R.L., Sweredoski M.J., Hess S., Coon J.J., Deshaies R.J. (2014). F-box protein FBXL16 binds PP2A-B55α and regulates differentiation of embryonic stem cells along the FLK1+ lineage. Mol Cell Proteomics 13, 780-791.

Jiang, G.Y., Zhang, X.P., Wang, L., Lin, X.Y., Yu, J.H., Wang, E.H., and Zhang, Y. (2016). FBXO25 promotes cell proliferation, invasion, and migration of NSCLC. Tumour Biol 37, 14311-14319.

Jin, J., Cardozo, T., Lovering, R.C., Elledge, S.J., Pagano, M., and Harper, J.W. (2004). Systematic analysis and nomenclature of mammalian F-box proteins. Genes & development 18, 2573-2580.

Kamran, M., Long, Z.J., Xu, D., Lv, S.S., Liu, B., Wang, C.L., Xu, J., Lam, E.W., and Liu, Q. (2017). Aurora kinase A regulates Survivin stability through targeting FBXL7 in gastric cancer drug resistance and prognosis. Oncogenesis 6, e298.

Katayama, K., Noguchi, K., and Sugimoto, Y. (2013). FBXO15 regulates P-glycoprotein/ABCB1 expression through the ubiquitin--proteasome pathway in cancer cells. Cancer Sci 104, 694-702.

Keuss, M.J., Thomas, Y., McArthur, R., Wood, N.T., Knebel, A., and Kurz, T. (2016). Characterization of the mammalian family of DCN-type NEDD8 E3 ligases. J Cell Sci 129, 1441-1454.

Kim, A.Y., Bommelje, C.C., Lee, B.E., Yonekawa, Y., Choi, L., Morris, L.G., Huang, G., Kaufman, A., Ryan, R.J., Hao, B., et al. (2008). SCCRO (DCUN1D1) is an essential component of the E3 complex for neddylation. The Journal of biological chemistry 283, 33211-33220.

Kirschner, M., and Mitchison, T. (1986). Beyond self-assembly: from microtubules to morphogenesis. Cell 45, 329-342.

Klebe, C., Prinz, H., Wittinghofer, A., and Goody, R.S. (1995). The kinetic mechanism of Ran—nucleotide exchange catalyzed by RCC1. Biochemistry 34, 12543–12552.

Kroll, M., Margottin, F., Kohl, A., Renard, P., Durand, H., Concordet, J.P., Bachelerie, F., Arenzana-Seisdedos, F., and Benarous, R. (1999). Inducible degradation of IkappaBalpha by the proteasome requires interaction with the F-box protein h-betaTrCP. The Journal of biological chemistry 274, 7941-7945.

Kulak, N.A., Pichler, G., Paron, I., Nagaraj, N., and Mann, M. (2014). Minimal, encapsulated proteomic-sample processing applied to copy-number estimation in eukaryotic cells. Nature methods 11, 319-324.

Kurz, T., Chou, Y.C., Willems, A.R., Meyer-Schaller, N., Hecht, M.L., Tyers, M., Peter, M., and Sicheri, F. (2008). Dcn1 functions as a scaffold-type E3 ligase for cullin neddylation. Molecular cell 29, 23-35.

Li, J., Yakushi, T., Parlati, F., Mackinnon, A.L., Perez, C., Ma, Y., Carter, K.P., Colayco, S., Magnuson, G., Brown, B., et al. (2017). Capzimin is a potent and specific inhibitor of proteasome isopeptidase Rpn11. Nat Chem Biol 13, 486-493.

Liu, J., Furukawa, M., Matsumoto, T., and Xiong, Y. (2002). NEDD8 modification of CUL1 dissociates p120(CAND1), an inhibitor of CUL1-SKP1 binding and SCF ligases. Molecular cell 10, 1511-1518.

Liu, Y., Mimura, S., Kishi, T., and Kamura, T. (2009). A longevity protein, Lag2, interacts with SCF complex and regulates SCF function. The EMBO journal 28, 3366-3377.

Lo, S.C., and Hannink, M. (2006). CAND1-mediated substrate adaptor recycling is required for efficient repression of Nrf2 by Keap1. Molecular and cellular biology 26, 1235-1244.

Lu, Y., Lee, B.H., King, R.W., Finley, D., and Kirschner, M.W. (2015). Substrate degradation by the proteasome: a single-molecule kinetic analysis. Science 348, 1250834.

Lydeard, J.R., Schulman, B.A., and Harper, J.W. (2013). Building and remodelling Cullin-RING E3 ubiquitin ligases. EMBO Rep 14, 1050-1061.

Monda, J.K., Scott, D.C., Miller, D.J., Lydeard, J., King, D., Harper, J.W., Bennett, E.J., and Schulman, B.A. (2013). Structural conservation of distinctive N-terminal acetylation-dependent interactions across a family of mammalian NEDD8 ligation enzymes. Structure 21, 42-53.

Mosadeghi, R., Reichermeier, K.M., Winkler, M., Schreiber, A., Reitsma, J.M., Zhang, Y., Stengel, F., Cao, J., Kim, M., Sweredoski, M.J., et al. (2016). Structural and kinetic analysis of the COP9-Signalosome activation and the cullin-RING ubiquitin ligase deneddylation cycle. eLife 5.

Peskin, C.S., Odell, G.M., and Oster, G.F. (1993). Cellular motions and thermal fluctuations: the Brownian ratchet. Biophys J 65, 316-324.

Pierce, N.W., Lee, J.E., Liu, X., Sweredoski, M.J., Graham, R.L., Larimore, E.A., Rome, M., Zheng, N., Clurman, B.E., Hess, S., et al. (2013). Cand1 Promotes Assembly of New SCF Complexes through Dynamic Exchange of F Box Proteins. Cell 153, 206-215.

Ran, F.A., Hsu, P.D., Lin, C.Y., Gootenberg, J.S., Konermann, S., Trevino, A.E., Scott, D.A., Inoue, A., Matoba, S., Zhang, Y., et al. (2013). Double nicking by RNA-guided CRISPR Cas9 for enhanced genome editing specificity. Cell 154, 1380-1389.

Raue, A., Kreutz, C., Maiwald, T., Bachmann, J., Schilling, M., Klingmüller, U., Timmer, J. (2009) Structural and practical identifiability analysis of partially observed dynamical models by exploiting the profile likelihood. Bioinformatics 25, 1923-1929.

Reitsma JM, Liu X., Reichermeier KM, Moradian A, Sweredoski MJ, Hess S and Deshaies RJ (2017). Composition and regulation of the cellular repertoire of SCF ubiquitin ligases. Cell 171,1326-1339.

Saha, A., and Deshaies, R.J. (2008). Multimodal activation of the ubiquitin ligase SCF by Nedd8 conjugation. Molecular cell 32, 21-31.

Salahudeen, A.A., Thompson, J.W., Ruiz, J.C., Ma, H.W., Kinch, L.N., Li, Q., Grishin, N.V., and Bruick, R.K. (2009). An E3 ligase possessing an iron-responsive hemerythrin domain is a regulator of iron homeostasis. Science 326, 722-726.

Schmidt, M.W., McQuary, P.R., Wee, S., Hofmann, K., and Wolf, D.A. (2009). F-box-directed CRL complex assembly and regulation by the CSN and CAND1. Molecular cell 35, 586-597.

Schulman, B.A., Carrano, A.C., Jeffrey, P.D., Bowen, Z., Kinnucan, E.R.E., Finnin, M.S., Elledge, S.J., Harper, J.W., Pagano, M., and Pavietich, N.P. (2000). Insights into SCF ubiquitin ligases from the structure of the Skp1-Skp2 complex. Nature 408, 381-386.

Scott, D.C., Sviderskiy, V.O., Monda, J.K., Lydeard, J.R., Cho, S.E., Harper, J.W., and Schulman, B.A. (2014). Structure of a RING E3 trapped in action reveals ligation mechanism for the ubiquitin-like protein NEDD8. Cell 157, 1671-1684.

Shen, B., Zhang, W., Zhang, J., Zhou, J., Wang, J., Chen, L., Wang, L., Hodgkins, A., Iyer, V., Huang, X., et al. (2014). Efficient genome modification by CRISPR-Cas9 nickase with minimal off-target effects. Nature methods 11, 399-402.

Soucy, T.A., Smith, P.G., Milhollen, M.A., Berger, A.J., Gavin, J.M., Adhikari, S., Brownell, J.E., Burke, K.E., Cardin, D.P., Critchley, S., et al. (2009). An inhibitor of NEDD8-activating enzyme as a new approach to treat cancer. Nature 458, 732-736.

Spencer, E., Jiang, J., and Chen, Z.J. (1999). Signal-induced ubiquitination of IkappaBalpha by the F-box protein Slimb/beta-TrCP. Genes & development 13, 284-294.

Srinivasan, J., Dillman, A.R., Macchietto, M.G., Heikkinen, L., Lakso, M., Fracchia, K.M., Antoshechkin, I., Mortazavi, A., Wong, G., and Sternberg, P.W. (2013). The draft genome and transcriptome of Panagrellus redivivus are shaped by the harsh demands of a free-living lifestyle. Genetics 193, 1279-1295.

Straube R, Shah M, Flockerzi D, and Wolf DA (2017). Trade-off and flexibility in the dynamic regulation of the cullin-RING ubiquitin ligase repertoire. PLoS Comput Biol 13, e1005869.

Wu, S., Zhu, W., Nhan, T., Toth, J.I., Petroski, M.D., and Wolf, D.A. (2013). CAND1 controls in vivo dynamics of the cullin 1-RING ubiquitin ligase repertoire. Nat Commun 4, 1642.

Xu, G., Ma, H., Nei, M., and Kong, H. (2009). Evolution of F-box genes in plants: different modes of sequence divergence and their relationships with functional diversification. Proceedings of the National Academy of Sciences of the United States of America 106, 835-840.

Zemla, A., Thomas, Y., Kedziora, S., Knebel, A., Wood, N.T., Rabut, G., and Kurz, T. (2013). CSN- and CAND1-dependent remodelling of the budding yeast SCF complex. Nat Commun 4, 1641.

Zheng, N., Schulman, B.A., Song, L., Miller, J.J., Jeffrey, P.D., Wang, P., Chu, C., Koepp, D.M., Elledge, S.J., Pagano, M., et al. (2002). Structure of the Cul1-Rbx1-Skp1-F-boxSkp2 SCF ubiquitin ligase complex. Nature 416, 703-709.

FIGURE LEGEND

Figure 1. Properties of interactions among Cul1, Cand1 and Skp1•F-box protein revealed by FRET.

(A) FRET assay for Cand1•Cul1 complex formation. Fluorescence emission spectra from excitation at 350 nm of 70 nM Cul1^{AMC}•Rbx1, 70 nM $^{FlAsH\Delta H1}$Cand1, a mixture of the two (FRET), chase control for FRET, or buffer alone. +Chase indicates 700 nM Cand1. Proteins were added in the indicated order. Addition of chase to Cul1+Cand1 had a negligible effect on FRET due to the long $t_{1/2}$ of the Cand1•Cul1 complex as shown previously (Pierce et al., 2013).

(B) k_{on} for Cand1 binding to Cul1. The observed rates of Cand1•Cul1 assembly at different concentrations of Cand1 are plotted. Linear slope gives k_{on} of 1.7×10^7 $M^{-1}s^{-1}$. Error bars, ± SEM, n = 5 (see also Fig S1A).

(C) k_{on} for Cand1 binding to Cul1•Rbx1 preassembled with FBP. Similar to Fig 1B, except with 100 nM Skp1•Skp2 preincubated with 50 nM Cul1^{AMC}•Rbx1. Linear slope gives k_{on} of 2.0×10^6 $M^{-1}s^{-1}$. Error bars, ± SEM, n ≥ 4 (see also Fig S1B).

(D) Disruption of Cand1•Cul1 by Skp1•Skp2. The change in donor fluorescence versus time was measured following addition of 75 nM Skp1•Skp2 or 75 nM Skp1 to 25 nM $^{FlAsH\Delta H1}$Cand1•Cul1^{AMC}•Rbx1.

(E) k_{off} of Cand1 from ternary exchange intermediate. The single exponential observed rates of Cand1 dissociation from 10 nM $^{FlAsH\Delta H1}$Cand1•Cul1^{AMC}•Rbx1 in the presence of increasing concentrations of Skp1•Skp2 were measured (see Fig S1C) and plotted. Fitting of the curve predicts a rate plateau at 67 sec^{-1}. Error bars, ± SEM, n ≥ 3.

(F) Kinetic model of the exchange cycle. The number in parentheses indicates the k_{off} of 2.9 s^{-1} calculated from detailed balance relations (see Fig S4C).

(G) Deletion of β hairpin in Cand1 enables formation of a stable complex comprising Cul1, Skp1•Fbxw7, and Cand1. Cand1 or Cand1Δβ (100 nM) was added to 70 nM ^{CFP}Cul1•Rbx1•Skp1•Fbxw7^{TAMRA}, and formation of SCF^{Fbxw7} was monitored by FRET. + Chase indicates 700 nM Skp1•Skp2.

(H) Deletion of loop regions in Skp1 enables formation of a stable complex comprising Cul1, Skp1•Skp2, and Cand1. Skp1•Skp2 or Skp1ΔΔ•Skp2 (700 nM) was added to 70 nM ^{FlAsH}Cand1•Cul1^{AMC}•Rbx1 and the persistence of the latter complex was monitored by FRET.

Figure 2. Cand1/2 double knockout (DKO) cells display defects in IκBα degradation and SCF$^{β\text{-}TrCP}$ assembly.

(A-C) Cand1/2 DKO cells display defects in IκBα degradation. IκBα levels in indicated cell lines were monitored by western blot (WB) at indicated time points after TNFα treatment. Both phospho-IκBα (pIκBα, upper band) and unmodified IκBα (lower band) were detected by the anti-IκBα antibody. Here and elsewhere in this work, we blotted for GAPDH as a loading control.

(B) WB analysis of Cand1 and β-TrCP in cell lysates from (A). A more intense exposure (dark) of the Cand1 blot and relative levels of Cand1 are also shown.

(C) Quantification of IκBα $t_{1/2}$ from panel A.

(D) Ubiquitination of pIκBα is significantly reduced in DKO cells. WB analysis (with anti-pIκBα antibody) of the ubiquitination of pIκBα in WT and DKO cells upon TNFα treatment. DKO36 from (A) was used in this experiment and thereafter.

(E-F) TNFα promotes formation of SCF$^{β\text{-}TrCP}$ in WT but not DKO cells. Schematic workflow of the experiment is depicted in (E), and WB analysis of endogenous SCF$^{β\text{-}TrCP}$ in WT and DKO cells before and after 10-min TNFα treatment is shown in (F). Relative levels of SCF$^{β\text{-}TrCP}$ were calculated as the β-TrCP:Cul1 ratio in ^{3xFLAG}Cul1 immunoprecipitations (IPs), and all ratios were normalized to that obtained for the IP from WT cells not treated with TNFα. Average fold increase of SCF$^{β\text{-}TrCP}$ induced by TNFα treatment is shown in the graph. Error bars, ± SEM, n = 3, P value = 0.001.

(G-H) Recruitment of Cul1 to pIκBα•β-TrCP is inefficient in DKO cells. Schematic workflow of the experiment is depicted in (G), and WB analysis of the recruitment of β-TrCP and Cul1 to pIκBα following 10-min TNFα treatment is shown in (H). Expression of ^{3xFLAG}IκBα was induced by 100 ng/ml tetracycline for 24 hours. Relative levels of β-TrCP and Cul1 recruited to pIκBα were calculated as the β-TrCP:pIκBα (see also Fig S2I) and Cul1:β-TrCP ratios in the IPs. Average levels of Cul1 recruited to pIκBα•β-TrCP are shown in the graph. Error bars, ± SEM, n = 3, P value = 0.0001.

Figure 3. Cand1 enhances formation of Cul1•Dcn1 complex and subsequent neddylation of Cul1 stabilizes newly formed SCF.

(A) Stable Cul1•Dcn1 complex is dramatically reduced in DKO cells. IP-WB analysis of interactions between endogenous ^{3xFLAG}Cul1 and Dcn1 in WT and DKO cells pre-treated with either 0.1% DMSO or 1 µM MLN4924 for 1 hour.

(B) Cand1 stabilizes Cul1•Dcn1 complex *in vitro*. Pulldown-WB analysis of recombinant Dcn1 (0.2 µM) and Ubc12 (0.2 µM) bound to recombinant Cul1•^{GST}Rbx1 (0.4 µM) in the presence and absence of recombinant Cand1, Cand1$^{1\text{-}603}$, or Cand1$^{604\text{-}1230}$ (all 0.4 µM). A more intense exposure (dark) of the Dcn1 blot is also shown.

(C) The Cul1•^{GST}Dcn1 complex is stabilized by Cand1 *in vitro*. Pulldown (PD) analysis of recombinant Cul1•Rbx1 (1 µM) bound to recombinant ^{GST}Dcn1 (0.6 µM) in the presence of 0-3 µM Cand1. Protein samples were fractionated on a SDS-PAGE gel and stained with Coomassie Blue. Normalized levels of Cul1 recovered were calculated as the ratio of Cul1 to ^{GST}Dcn1. (See also Fig S3A)

(D) Thermodynamic cycle of Dcn1, Cul1•Rbx1 and Cand1 binding. All numbers are K_D values. The K_D of 1.8 x 10^{-6} M for Dcn1 and Cul1•Rbx1 was reported previously (Monda et al., 2013); the K_D of 5 x 10^{-8} M for Dcn1 and Cand1•Cul1•Rbx1 was estimated based on results in Fig 3C and S3A; the K_D of 7 x 10^{-13} M for Cul1•Rbx1 and Cand1 was from Fig 1B; and the K_D in parentheses was calculated from detailed balance considerations (see Fig S4C).

(E-F) Cand1-bound Cul1 is neddylated faster than free Cul1 in the presence of FBPs. Schematic workflow of a competitive Cul1 neddylation assay is shown in (E). Free Cul1•Rbx1 and Cand1•Cul1•Rbx1 in which the different Cul1 species are labeled with different fluors (FAM or TAMRA) compete for limiting Dcn1, and neddylation enzymes are provided by DKO lysate. 1x represents 50 nM protein in the final sample mixture. Fluorescence scan of the SDS-PAGE gel containing samples prepared as described in (E) is shown in (F). “Fold increase with Cand1” was calculated as the ratio of percent neddylation of Cand1-bound Cul1 to free Cul1 (see Fig S3B-C for negative controls). A representative result of three replicates is shown.

(G) Neddylation increases the assembly of FBP with Cand1-bound Cul1. Cand1, Dcn1 and Cul1•^{GST}Rbx1 were pre-incubated and then mixed 1:1 (v:v) with Skp1•β-TrCP and Ubc12 or Ubc12 charged to Nedd8 (Ubc12~Nedd8). After 15 min incubation, the protein mixture was incubated with glutathione beads and immobilized proteins were analyzed by WB. (See also Fig S3D.)

Figure 4. Mathematical model of the SCF cycle.

(A) Simplified scheme illustrating the main processes and interactions considered in the mathematical model (see Fig S4 for a detailed reaction scheme). Lines with unidirectional arrows represent irreversible reactions. FB1 stands for Skp1•β-TrCP whereas FB2 represents a pool of auxiliary Skp1•F-box proteins that compete for access to Cul1•Rbx1. Both F-box proteins form SCF ligases with Cul1•Rbx1 that undergo the same cycle of processes including F-box exchange, neddylation, deneddylation, substrate binding and substrate degradation.

(B-F) Model simulations and predictions. Simulations labeled in orange color were used to estimate unknown parameters. Remaining simulations represent model predictions. Error bars for predictions were obtained from a profile likelihood analysis (Fig S5A). Experimental results are shown as thin bars. To simulate inhibition of Nedd8 conjugation by MLN4924 we set k_{nedd}=0. As a result the fraction of Cul1•Rbx1 bound to Cand1 increased while the fraction of Cul1•Rbx1 bound to Skp1•FBP decreased (Reitsma et al. 2017) (B). If Cand proteins are absent (DKO) the latter fraction is predicted to increase to 100% in agreement with observations. The model confirms (C, upper panel) that re-expression of Cand1 (13% of WT level) in a DKO cell line reduces the half-life ($t_{1/2}$) for IκBα degradation back to WT levels (Fig 2C). The half-life for substrate degradation is predicted to exhibit a U-shaped dependence on the cellular Cand1 concentration with an extended valley where $t_{1/2}$ ≈20min remains approximately constant (C, lower panel). Dashed lines indicate the Cand1 concentration in WT (black) and DKO cells with Cand1 re-expressed to 13% of WT level (red). When substrate is added the fraction of β-TrCP bound to Cul1 increases ~1.7-fold (D) from its steady state level (46%) as observed in WT cells (Fig 2F). Cul1 overexpression is predicted to reduce the fraction of neddylated Cul1 (E) in agreement with observations. Also, Cul1 overexpression should have no effect on the half-life for IκBα degradation in WT, but should reduce $t_{1/2}$ in DKO cells back to WT level (F). In contrast, overexpression of β-TrCP is predicted to have no effect on $t_{1/2}$ in DKO cells (F).

Figure 5. Experimental concordance with mathematical predictions.

(A) ^{3xFLAG}Cul1 overexpression rescues the IκBα degradation defect of DKO cells. IκBα levels were monitored by western blot (WB) at indicated time points after TNFα treatment. Overexpression of ^{3xFLAG}Cul1 was induced by tetracycline. Average relative $t_{1/2}$ of IκBα are shown in the graph. Error bars: range of values, n = 2.

(B) ^{3xFLAG}Cul1 overexpression impedes cullin neddylation. WB analysis of cullins in cell lysates from (A). Fold increase in total Cul1 levels and percent neddylation of overexpressed ^{3xFLAG}Cul1 and endogenous Cul4a are indicated. A representative result of two replicates is shown.

(C) β-TrCP overexpression does not rescue the IκBα degradation defect of DKO cells. IκBα levels were monitored by western blot (WB) at indicated time points after TNFα treatment. Overexpression of β-TrCP was induced by tetracycline. Average relative $t_{1/2}$ of IκBα are shown in the graph. Error bars: range of values, n = 2. (See Fig S5E for WB of β-TrCP)

(D-E) Overexpression of Cul1 significantly depletes free β-TrCP in the DKO cells. As illustrated in (D), cells with/without tetracycline induced ^{3xFLAG}Cul1 were lysed in buffer containing Cul1•^{GST}Rbx1 sponge protein and subjected to GST pulldown, which probes changes in levels of unbound cellular proteins capable of binding to sponge in cell lysate (see Fig S5F for WB images). Average changes in protein levels compared to non-tetracycline induced control are shown in the graph. Overexpression of ^{3xFLAG}Cul1 depleted the pool of free β-TrCP in DKO cells by 80%. Error bars: range of values, n = 2.

(F-G) Overproduction of β-TrCP modestly reduces the efficiency of its assembly with Cul1. As illustrated in (F), cells containing endogenous ^{3xFLAG}Cul1 were lysed in buffer containing Cul1•^{GST}Rbx1 sponge protein. β-TrCP bound to endogenous ^{3xFLAG}Cul1 was probed by anti-FLAG beads, and free cellular β-TrCP capable of binding to sponge in cell lysate was probed by GST beads (see Fig S5G for WB images). Percentage of β-TrCP bound to endogenous ^{3xFLAG}Cul1 in WT and DKO cells with or without tetracycline-induced overexpression of β-TrCP is graphed. Error bars: range of values, n = 2.

Figure 6. Overexpression of single F-box proteins suppresses cell proliferation in DKO cells by sequestering Cul1.

(A) Overexpression of Fbxo6 increases the $t_{1/2}$ of IκBα only in DKO cells (see Fig S6A-B for WB images). Fbxo6 was overexpressed by transduction with a recombinant lentivirus expressing ^{HA}Fbxo6. The assay was performed four days after the viral transduction. Average fold increase of IκBα $t_{1/2}$ by Fbxo6 overexpression in WT and DKO cells are graphed. Error bar: ± SD, n = 3, P value < 0.01.

(B) Overexpression of Fbxo6 in DKO cells reduces degradation of SCF substrates. All samples were analyzed on the same gel and blot, but one lane between WT and DKO samples on the blot image was eliminated and indicated as a space.

(C) Overexpressed Fbxo6 sequesters Cul1 in DKO cells. Cells were infected with recombinant lentiviruses carrying the ^{HA}Fbox6 gene five days before ^{HA}Fbxo6 was IP'd from WT$^{3xFLAG\text{-}Cul1}$ and DKO$^{3xFLAG\text{-}Cul1}$ cells in the presence of recombinant Cul1•^{GST}Rbx1 (+ sponge). Equal percent volumes of Input (In), immunoprecipitation eluent (IP), and flow-through (FT) were analyzed by WB. Long (L) and short (S) exposures of endogenous ^{3xFLAG}Cul1 are shown. Quantifications of percent Cul1 in the ^{HA}Fbxo6 IPs are graphed. Error bars: ± SD, n = 3, P value < 0.01.

(D) Fbxo6 overexpression reduces proliferation of DKO cells in a specific, FBP-dependent manner. Cells were treated with recombinant lentiviruses carrying different FBP constructs as indicated. Three days after lentiviral infection, cells were equally seeded and counted every 24 hrs for 4 days. Average cell doubling time is graphed. Error bars: ± SD, n = 3, P value < 0.01. Note that Fbxl16 bound at least as much Skp1 as Fbxo6 but did not bind Cul1 (compare Fig S6G with panel D), and that re-introduction of Cand1 rescued the DKO cells.

(E) Overexpression of Cul1 partially rescues toxicity of overproduced Fbxo6 in DKO cells. Cul1 overexpression was induced by tetracycline. Cell doubling was measured as in (D). Error bars: ± SD, n = 3.

(F) Overexpression of ^{HA}Skp2 or ^{HA}Skp2$^{\Delta LRR}$ slows cellular proliferation in DKO cells. Cells were infected by lentiviruses and cell doubling was measured as in (D). Error bars: ± SD, n = 3, P value < 0.01.

(G) Overexpression of ^{HA}Skp2$^{\Delta LRR}$ increased the level of apoptosis marker in DKO cells. A representative result of two replicates is shown.

Figure 7. Rapid cycling of Cul1 in human cells.

(A) Cycling of Cul1 summarized from biophysical, cellular and computational studies. Association rates are computed based on k_{on} and steady state cellular concentrations of unbound proteins, and the cycle time for Cul1 is computed using effective rates for the reversible binding steps (see also Fig S5D). The reversal of the de-neddylation reaction by Dcn1 (dashed lines) is discouraged in WT cells due to preferential association of Dcn1 with Cand1•Cul1, but is expected to occur more frequently in DKO cells. The substrate of the SCF complex can bind the FBP either in its free or assembled state. Substrate binding stabilizes the SCF complex by preventing CSN from binding. The 55 s cycle time for Cul1 represents the average time it takes a Cul1 molecule to be deneddylated and exchanged into a different SCF if it is not bound by substrate.

(B) Deneddylation of Cul1 is fast in human cells. HEK293 cells were treated with 3 µM MLN4924 to inhibit the Nedd8 E1 and were maintained at 37°C for the indicated time before being directly lysed on culture plates. Average $t_{1/2}$ for deneddylation is shown. Error bars, ± SD, n = 3.

(C) Neddylation of Cul1 is fast in human cells. Assay condition was similar to (B) but 3 µM CSN5i-3 was used to inhibit CSN (Schlierf et al., 2016). Average $t_{1/2}$ for neddylation is shown. Error bars, ± SD, n = 3.

STAR METHODS

EXPERIMENTAL MODEL AND SUBJECT DETAILS

Flp-In T-REx 293 cells (RRID:CVCL_U427) were grown in Dulbecco's Modified Eagle's Medium (DMEM) with 10% tetracycline-free fetal bovine serum (Clontech) and penicillin at 37 °C. The generation of stable cell lines is described below in method details.

METHOD DETAILS

Constructs

$^{\Delta H1}$Cand1 was generated by replacing the first 14 codons of full length Cand1 cDNA with DNA sequence encoding CCPGCCGSG. The resulting construct was inserted into the Xma1/Not1 sites of pGEX-4T for expression in E. coli. Cand1$^{1-603}$ and Cand1$^{604-1230}$ were designed by truncating the full length Cand1 cDNA at the indicated codons and inserting the PCR products into the Xma1/Not1 sites of pGEX-4T for expression in E. coli. Constructs for CRISPR nickase- mediated gene knockout in mammalian cells were designed as described (Ran et al., 2013). Briefly, oligos containing sgRNA sequences were annealed and inserted into the Bbs1 site of pX335 (Addgene). The homologous recombination template was generated by first cloning the 300-bp homologous recombination regions using genomic DNA purified from WT 293 cells as the PCR templates, then inserting the antibiotic resistance gene plus a terminator between the two homologous recombination DNA fragments using overlapping PCR (Heckman & Pease, 2007), and finally inserting the resulting PCR products into the EcoR1/Xho1 sites of pGEX-4T. For generation of stable cells lines using the Flp-In system, cDNAs encoding Cand1^{HA}, ^{3xFLAG}Cul1, ^{3xFLAG}IκBα and ^{2xStrepII}β-TrCP were individually inserted into pcDNA5/FRT/TO vector (Thermo Fisher Scientific). For expression of exogenous genes in Figure 6, the lentiviral backbone pCDH-EF1-MCS-IRES-NEO (System Biosciences) was used to direct the expression of ^{HA}Fbxo6, ^{HA}Fbxo6$^{\Delta F\text{-}box}$(Δ10-57), ^{HA}Skp2, ^{HA}Skp2$^{\Delta LRR}$(1-234), ^{HA}Fbxl16, and ^{Myc}Cand1.

Protein Expression and Purification

Cul1•Rbx1, Skp1•Skp2, and Skp1ΔΔ•β-TrCP$^{139\text{-}569}$ were purified as described (Saha and Deshaies, 2008). Cand1, Skp1ΔΔ•Skp2, Skp1•Fbxw7$^{\text{TAMRA}}$, and Skp1•β-TrCP$^{139\text{-}569}$ were purified as described (Pierce et al., 2013). Cul1•$^{\text{GST}}$Rbx1 was purified as described for Cul1•Rbx1, omitting the thrombin digestion step. Cul1$^{\text{Sortase-Tag}}$•Rbx1 was expressed by cotransforming BL21 E. coli with RDB 2080 and RDB 2557 and inducing overnight at 16°C; it was then purified on glutathione resin followed by digestion with thrombin and chromatography on HiTrap SP cation exchange column (GE Healthcare), and was exchanged to buffer containing 50 mM Tris (pH 7.6), 150 mM NaCl, 10 mM $CaCl_2$ using PD-10 columns (GE Healthcare). Cul1$^{\text{Sortase-Tag}}$•Rbx1 was incubated with 60 µM Sortase and 250 µM GGGG$^{\text{AMC}}$, GGGGK$^{\text{TAMRA}}$, or GGGGK$^{\text{FAM}}$ peptides (New England Peptide) at room temperature for 24 hr. Cul1$^{\text{AMC}}$•Rbx1, Cul1$^{\text{TAMRA}}$•Rbx1, and Cul1$^{\text{FAM}}$•Rbx1 were further purified by S200 size exclusion chromatography. $^{\Delta\text{H1}}$Cand1 was expressed in Rosetta E. coli with IPTG induction overnight at 16°C, and was purified on glutathione resin followed by digestion with thrombin and chromatography on HiTrap Q cation exchange column (GE Healthcare) and S200 size exclusion column. Then 50 µl of 40 µM $^{\Delta\text{H1}}$Cand1 was incubated with 1 µl Lumio Green (FlAsH) dye (Thermo Fisher Scientific) in buffer containing 20 mM Tris (pH7.5), 100 mM NaCl, 2 mM TCEP (Thermo Fisher Scientific), 1 mM EDTA, and 5% glycerol at room temperature for at least two hours to generate $^{\text{FlAsH}\Delta\text{H1}}$Cand1. Cand1$^{1\text{-}603}$, Cand1$^{604\text{-}1230}$, Skp1, and Dcn1 were expressed and purified similarly to the preparation of Cand1. Ubc12 was expressed in Sf9 cells from a recombinant baculovirus and was prepared as previously described (Scott et al., 2014).

FRET Assay

Fluorimeter scans were performed on a Fluoromax-4 Spectrofluorometer (Jobin Yvon) in a buffer containing 30 mM Tris (pH 7.6), 100 mM NaCl, 0.5 mM DTT, and 1 mg/ml Ovalbumin (Sigma). Mixtures containing Cul1$^{\text{AMC}}$•Rbx1 were excited at 350 nm and the emissions were scanned from 400 nm to 600 nm. Mixtures containing $^{\text{CFP}}$Cul1•Rbx1 were excited at 430 nm and the emissions were scanned from 450 nm to 650 nm. Stopped flow reactions were performed on a Kintek stopped flow machine in the same buffer as the fluorimeter scans.

Antibodies

The following primary antibodies were used in Western Blot analyses: anti-Cand1 (Bethyl Laboratories # A302-901, Santa Cruz Biotechnology # 10672), anti-Cand2 (Bethyl Laboratories # A304-046A), anti-IκBα (Abcam # ab32518), anti-β-TrCP (Cell Signaling # 4394S), anti-GAPDH (Millipore # MAB374), anti-Cul1 (Thermo Fisher Scientific # 32-2400), anti-phospho-IκBα (Cell Signaling Technology # 9246S), anti-FLAG (Sigma # F1804), anti-Dcn1 (Novus Biologicals # H00054165-A01), anti-Ubc12 (Rockland # 600-401-865), anti-Irp2 (Santa Cruz Biotechnology # 33682), anti-Fbxl5 (Neoclone # N0036), anti-Cul4a (Cell Signaling Technology # 2699S), anti-Rbx1 (Bethyl Laboratories # A303-462A), anti-Skp1 (Thermo Fisher Scientific # MA5-15928), anti-HA-HRP (Sigma # 12013819001) , anti-cleaved PARP (Asp214) (Cell Signaling # 5625), anti-Fbxo6 (Abcam # 103635), anti-Cyclin E (Santa Cruz Biotechnology # 247), anti-Skp2 (D3G5) (Cell Signaling # 2652S), anti-p27 (Abcam # 32034). Alexa Fluor 680 conjugated anti-mouse IgG (Thermo Fisher Scientific # A10038), Alexa Fluor 790 conjugated anti-rabbit IgG (Thermo Fisher Scientific # A11374), and Alexa Fluor 680 conjugated anti-rabbit IgG (Abcam # ab175772) secondary antibodies were used to detect the primary antibodies on an Odyssey Imager (LI-COR Biosciences). HRP-conjugated anti-rabbit IgG (Sigma), HRP-conjugated anti-mouse IgG (Sigma), and anti-mouse IgG HRP Mouse TrueBlot Ultra (Rockland # 18-8817-33) were used to detect the primary antibodies using chemiluminescence.

Generation of Stable Cell Lines

To construct Cand1/2 DKO cells, the CAND2 gene was first knocked out in Flp-In T-REx 293 cells to generate Cand2 single KO cells, followed by disruption of the CAND1 gene. To knock out the CAND2 gene with CRISPR-Cas9 nickases, WT cells in a 12-well plate were cotransfected with three plasmids: 0.2 µg pX335 containing “GTGGAAGGCGGCGGTGCTCA” guide RNA, 0.2 µg pX335 containing “GAAGATGACGTCCAGCGACA” guide RNA, and 0.2 µg pGEX-4T containing neomycin resistance gene plus a SV40 terminator which was placed between two 300-bp DNA sequences that are identical to CAND2 genomic DNA regions flanking the first exon. Twenty-four hours after cotransfection, cells were transferred to 15-cm plates and cultured with medium containing 800 µg/ml G418 (Thermo Fisher Scientific). After two weeks, neomycin-resistant colonies were isolated and screened for the loss of Cand2 protein by immunoblot with an antibody recognizing the C-terminus of Cand2. Colonies that showed loss of Cand2 were further confirmed for complete knock out of Cand2 by sequencing PCR products of the genomic region surrounding the first exon of Cand2. Forward primer “AGCTGGCACCTACGGGAATAACAAGGA” and reverse primer “ACACACACGAGGGAGGAGAG” were used for PCR. The sequencing results also revealed independent KO cell colonies. A similar approach was used to knock out the Cand1 gene with CRISPR-Cas9 nickases. WT or Cand2 single KO cells were cotransfected with three plasmids: 0.2 µg pX335 containing “GCAAATTGGAAATGTGGTACG” guide RNA, 0.2 µg pX335 containing “GCATCCAGCGACAAGGACTTT” guide RNA, and 0.2 µg pGEX-4T containing puromycin resistance gene plus a BGH terminator placed between two 300-bp DNA sequences that are identical to Cand1 genomic DNA regions flanking the first exon. Cells were then selected for resistance to 1 µg/ml puromycin, loss of Cand1 protein in immunoblot analysis, and disruption of WT Cand1 Exon 1 in the genomic DNA. Forward primer “TGTCTGGCTCCCCGTAGAGGCCCTTCT” and reverse primer “CCTATTCGCTTGCCATCCT” were used for PCR.

Site-specific fusion of sequences encoding the 3xFLAG tag to the 5’ end of the coding region of endogenous *CUL1* alleles is described elsewhere (Reitsma et al., 2017).

Targeted integrations of the coding sequences of Cand1^{HA}, ^{3xFLAG}Cul1, ^{3xFLAG}IκBα, or ^{2xStrepII}β-TrCP into the Flip-In T-REx 293 cells were carried out as described in the manual (Thermo Fisher Scientific). pcDNA5/FRT/TO vector containing the gene insert and pOG44 vector containing Flp recombinase were cotransfected into cells using Lipofectamine 3000 (Invitrogen). Cells were then selected for resistance to 100 µg/ml hygromycin and confirmed for tetracycline induced expression of integrated genes.

Lentiviral Infection

Lentiviral constructs were co-transfected with packaging (psPAX2) and enveloping (pMD.2G) plasmids (System Biosciences) into 293FT cells using Fugene HD (Promega). Virus-containing supernatants were harvested at 48 and 72 hrs after transfection. Relative viral titer was determined using Lenti-X GoStix (Clontech). HEK293 cells were infected at a multiplicity of infection of 2.0 at

24 hrs and 48 hrs after seeding, to ensure 100% cell infection rate which was verified by immunofluorescence.

IκBα Degradation Assay

Cells (0.6 million) of desired genotypes were seeded on 6-well plates and allowed to grow overnight with or without 100 ng/ml tetracycline in the medium. Cells were then incubated in DMEM medium containing no serum for 6 hours, and 100 µg/ml cycloheximide was added to the medium 10 minutes before the start of the assay. Cells were taken out of the cell culture incubator five minutes before the addition of 25 ng/ml TNFα (Sigma-Aldrich), and were kept at room temperature for the duration of the degradation assay. At different time points after the addition of TNFα, cells were washed with PBS and lysed by adding 2x SDS sample buffer to the plate. Cell lysates were collected in tubes and sonicated before fractionation by SDS-PAGE for Western Blot analyses. IκBα signals (both phosphorylated and unmodified IκBα) measured on an Odyssey Imager (LI-COR Biosciences) were normalized to GAPDH signals in the same sample and were fit to a single exponential in Prism to calculate half-lives.

In vivo IκBα Ubiquitination Assay

Similar to IκBα degradation assay, except that 1 µM bortezomib was added to the medium 30 minutes before TNFα treatment. Ubiquitinated phospho-IκBα was detected by anti-phospho-IκBα primary antibody.

Co-Immunoprecipitation Assay

To IP the endogenous ^{3xFLAG}Cul1 and probe the formation of SCF$^{\beta\text{-TrCP}}$, cells were resuspended in buffer containing 10 mM HEPES (pH 7.9), 1.5 mM $MgCl_2$, 10 mM KCl, 1 mM DTT, 1x protease inhibitors (Roche), 50 µM quinoline-8-thiol (8TQ, Sigma-Aldrich)(Li et al., 2017), 0.6% IGEPAL CA-630, and recombinant Cul1•Rbx1 protein at ~100x of the endogenous Cul1 level (1.5x cell pellet volume of 35 µM Cul1•Rbx1 solution)(Reitsma et al., 2017). Cells were lysed by sonication, and the supernatant of the cell lysate after 10-min centrifugation at 15,000 g was incubated with anti-FLAG beads (Sigma-Aldrich) for 30 minutes at 4 °C. The beads were then washed by the lysis buffer three times and eluted by 2x SDS-PAGE sample buffer. To IP ^{3xFLAG}IκBα, a similar method was used except that no recombinant Cul1•Rbx1 protein was added in the lysis buffer. To IP the endogenous ^{3xFLAG}Cul1 and probe the formation of the Cul1•Dcn1 complex, cells were lysed in buffer containing 50 mM HEPES (pH 7.5), 5 mM $Mg(OAc)_2$, 70 mM KOAc, 50 µM 8TQ, and protease inhibitors. Supernatant of the cell lysate after centrifugation was incubated with anti-FLAG beads (BioLegend) for 30 minutes at 4 °C, and the beads were washed in micro Bio-Spin columns (Bio-Rad) by the lysis buffer three times and eluted by 2x SDS-PAGE sample buffer. To determine percent β-TrCP bound to Cul1, cells were lysed by brief sonication after being mixed with Pierce IP lysis buffer (Thermo Fisher) containing 1x protease inhibitor (Roche), 50 µM 8TQ, and recombinant Cul1•^{GST}Rbx1 protein at ~100x of the endogenous Cul1 level (1.5x cell pellet volume of 35 µM Cul1•^{GST}Rbx1 solution), followed by sequential incubations with anti-FLAG beads and glutathione sepharose 4B beads (Reitsma et al., 2017). The precipitated proteins in each pull-down were eluted by 30 µl 2x SDS-PAGE sample buffer prior to WB analysis. To determine percent Cul1 bound to overexpressed HA-tagged F-box protein, cells were lysed by brief sonication after being mixed with Pierce IP lysis buffer (Thermo Fisher) containing 1x protease inhibitor (Roche) and recombinant Cul1•^{GST}Rbx1 'sponge' protein. Then 100 µl cell lysate (input) was withdrawn and incubated with anti-HA EZVIEW Red affinity beads (Sigma). After separating and collecting the flowthrough, the beads were eluted in 100 µl 2x SDS-PAGE sample buffer (IP), and 10 µl each of input, IP and flowthrough samples were fractionated by SDS-PAGE and analyzed by WB.

Usp2 on-bead treatment

After the immunoprecipitation of ^{3xFLAG}IκBα, anti-FLAG beads were washed and incubated with 0.5 µM Usp2 catalytic domain (Boston Biochem) in 30 µl buffer containing 50 mM HEPES (pH 8.0), 0.01% IGEPAL CA-630, and 3 mM DTT at 37 °C for 2.5 hours. The treatment was stopped and proteins were eluted by adding 10 µl of 4x SDS-PAGE sample buffer.

Quantification of Protein Concentration by WB

A few million WT cells were collected and resuspended in 150 µl PBS buffer containing full length recombinant ^{GST}IκBα (Novus Biologicals) and ^{GST}β-TrCP (Novus Biologicals) and lysed by mixing with 150 µl 4x SDS sample buffer. The total cell volume per sample was estimated by multiplying the total cell number and 2 pl/cell (BioNumbers.hms.harvard.edu). Recombinant ^{GST}IκBα and ^{GST}β-TrCP were added to a level corresponding to 200 nM and 26 nM of cellular concentration, respectively, as internal standards. Both endogenous and recombinant IκBα and β-TrCP were detected by immunoblot analysis to reveal the ratio of endogenous vs. internal standard protein for quantification. The concentration of added recombinant protein standard was determined by a serial dilution experiment prior to the quantification experiment to avoid over- or under-loading, and it was also verified that all quantified signals were within the linear range of detection.

In vitro Neddylation Assay

Neddylation reactions were conducted at room temperature in buffer containing 30 mM Tris (pH 7.5), 5 mM $MgCl_2$, and 2 mM ATP, with Dcn1 and NAE purified from E. coli and Ubc12 purified from Sf9 insect cells. Concentrations of Dcn1, NAE, and Ubc12 used in each experiment are specified in figures and figure legends. Nedd8 (Boston Biochem) was first thioesterified onto Ubc12 by NAE in an individual tube, and the Ubc12~Nedd8 was then mixed with Cul1 to start the neddylation reaction. When cell lysate was used for neddylation reaction, DKO cells pooled from a 10-cm culture plate were lysed in 200 µl buffer containing 30 mM Tris (pH 7.5), 5 mM $MgCl_2$, 2 mM ATP, protease inhibitors, and 50 µM 8TQ. After mixing the neddylation enzymes with Cul1, samples were incubated at room temperature for desired time periods, and the reaction was stopped by adding 4x SDS-PAGE sample buffer.

Dissociation of pIκBα•β-TrCP in Cell Lysate

DKO cells expressing ^{3xFLAG}IκBα were treated with 25 ng/ml TNFα for 15 min, and were collected and lysed in buffer containing 10 mM HEPES (pH 7.9), 1.5 mM $MgCl_2$, 10 mM KCl, 1 mM DTT, 0.6% IGEPAL CA-630, protease inhibitors, and phosphatase inhibitors (Thermo Fisher Scientific). An aliquot of cell lysate (100 µl) was incubated with anti-FLAG beads for 30 min to get 0-hr sample. Another 100 µl aliquot was kept at room temperature for 9.5 hr and then incubated with anti-FLAG beads for 30 min to get the 10-hr control sample. For the rest of the lysate, recombinant Skp1ΔΔ•β-TrCP$^{139-569}$ (0.8x cell pellet volume of 12 µM Skp1•β-TrCP$^{139-569}$ solution, ~100x of endogenous β-

TrCP level) was added as a chase, and the lysate was incubated at room temperature. Thirty min prior to each time point, 100 µl was drawn from the lysate-chase mixture and incubated with anti-FLAG beads for 30 min. All the proteins bound by the beads were eluted by 2x SDS-PAGE sample buffer and analyzed by SDS-PAGE followed by Western Blot.

Analysis of FBP Expression Levels

RNA-seq data for mouse development across multiple tissues was obtained from ENCODE (Mouse ENCODE Project; BioProject accession number PRJNA66167). Specifically, data for 66 tissues across embryonic and birth (day 0) timepoints generated by Barbara Wold's lab was used, along with data for ES cells from an E14 mouse embryo generated by Michael Snyder's lab. Processed data was downloaded in an automated manner and the average of Fragments Per Kilobase of transcript per Million mapped reads (FPKM) values for two replicates was retained for further analyses. Accession numbers or processed data for the 134 ENCODE datasets available upon request. For analyses, only transcripts expressed in ES cells (25130 transcripts) were considered. FBPs were defined as those previously described (Jin et al., 2004).

QUANTIFICATION AND STATISTICAL ANALYSIS

Western Blots with fluorescent signals were scanned on an Odyssey Imager (LI-COR Biosciences), and when necessary, multiple scans with different detection sensitivity levels were taken to avoid oversaturation. Images were exported as tif files, and protein band intensities were quantified by ImageJ (NIH) or Image Studio Lite (LI-COR Biosciences). Western Blots with chemiluminescence were detected by BioMax MR Film (Carestream) with varied exposure time lengths, and films with appropriate exposure strength were scanned and quantified using ImageJ (NIH). Protein gels stained by Coomassie blue were either imaged by Gel Doc™ XR+ Gel Documentation System (Bio-Rad) or scanned after drying between cellophane sheets, and the protein band intensities were quantified by ImageJ (NIH). Kinetic analyses were performed by regressions in Prism. Fluorescence signals detected by the Typhoon scanner were quantified by ImageQuant (GE Healthcare). Statistical parameters are reported in the Figures and Figure Legends. Data are judged to be statistically significant when $p < 0.05$ by two-tailed Student’s *t* test. Statistical analysis was performed in GraphPad QuickCalcs.

KEY RESOURCES TABLE

REAGENT or RESOURCE	SOURCE	IDENTIFIER
Antibodies		
anti-Cand1	Bethyl Laboratories	Cat # A302-901
anti-Cand2	Bethyl Laboratories	Cat # A304-046A
anti-IκBα	Abcam	Cat # ab32518
anti-β-TrCP	Cell Signaling	Cat # 4394S
anti-GAPDH	Millipore	Cat # MAB374
anti-Cul1	Thermo Fisher Scientific	Cat # 32-2400
anti-phospho-IκBα	Cell Signaling Technology	Cat # 9246S
anti-FLAG	Sigma	Cat # F1804
anti-Dcn1	Novus Biologicals	Cat # H00054165-A01
anti-Ubc12	Rockland	Cat # 600-401-865
anti-Irp2	Santa Cruz Biotechnology	Cat # 33682
anti-Fbxl5	Neoclone	Cat # N0036
anti-Cul4a	Cell Signaling Technology	Cat # 2699S
anti-Rbx1	Bethyl Laboratories	Cat # A303-462A
anti-Skp1	Thermo Fisher Scientific	Cat # MA5-15928
anti-HA, HRP conjugated	Sigma	Cat # 12013819001
anti-cleaved PARP (Asp214)	Cell Signaling	Cat # 5625
anti-Fbxo6	Abcam	Cat # 103635
anti-Cyclin E	Santa Cruz Biotechnology	Cat # 247
anti-Skp2 (D3G5)	Cell Signaling	Cat # 2652S
anti-p27	Abcam	Cat # 32034
Alexa Fluor 680 conjugated anti-mouse IgG	Thermo Fisher Scientific	Cat # A10038
Alexa Fluor 790 conjugated anti-rabbit IgG	Thermo Fisher Scientific	Cat # A11374
Alexa Fluor 680 conjugated anti-rabbit IgG	Abcam	Cat # ab175772
HRP-conjugated anti-rabbit IgG	Sigma	Cat # RABHRP1
HRP-conjugated anti-mouse IgG	Sigma	Cat # RABHRP2
anti-mouse IgG HRP Mouse TrueBlot Ultra	Rockland	Cat # 18-8817-33
ANTI-FLAG M2 Affinity Gel antibody	Sigma	Cat # A2220
EZview(TM) Red anti-HA Affinity Gel antibody	Sigma	Catc# E6779
Chemicals, Peptides, and Recombinant Proteins		
MLN4924	Active Biochem	Cat # A-1139
Quinoline-8-thiol	Sigma-Aldrich	Cat # 359785
Bortezomib	LC Laboratories	Cat # B-1408
Puromycin	Clontech	Cat # 631306
G418	Sigma	Cat # G8168
Hygromycin B (50 mg/mL)	Thermo Fisher Scientific	Cat # 10687010
Roche mini complete EDTA-free protease inhibitor	Roche	Cat # 4693116001

Pierce IP Lysis Buffer	Thermo Fisher Scientific	Cat # 87787
Ferric ammonium citrate	Thermo Fisher Scientific	Cat # R21215
GGGG^{AMC}	New England Peptide	N/A
GGGGK^{TAMRA}	New England Peptide	N/A
GGGGK^{FAM}	New England Peptide	N/A
Lumio™ Green Detection Kit	Thermo Fisher Scientific	Cat # LC6090
Ovalbumin	Sigma	Cat # A2512
Skp1ΔΔ•β-TrCP$^{139-569}$	Pierce et al., 2013	N/A
Skp1•β-TrCP$^{139-569}$	Pierce et al., 2013	N/A
Skp1•Fbxw7^{TAMRA}	Pierce et al., 2013	N/A
Nedd8	Boston Biochem	Cat # UL-812
TNFα	Sigma	Cat # H8916
Human USP2 catalytic domain protein	Boston Biochem	Cat # E-504
^{GST}IκBα	Novus Biologicals	Cat # H00008945-P01
^{GST}β-TrCP	Novus Biologicals	Cat # H00004792-P01
Critical Commercial Assays		
Lenti-X GoStix	Clontech	Cat # 631243
Experimental Models: Cell Lines		
Flp-In T-REX 293 Cell Line	Thermo Fisher Scientific	Cat # R78007 RRID:CVCL_U427
HEK293-FT Cell Line	Thermo Fisher Scientific	Cat # R70007 RRID:CVCL_6911
Oligonucleotides		
Cand2 targeting sequences (pX335)-1: 5’-CACCGTGGAAGGCGGCGGTGCTCA-3’ and 5’-AAACTGAGCACCGCCGCCTTCCAC-3’	This study	N/A
Cand2 targeting sequences (pX335)-2: 5’-CACCGAAGATGACGTCCAGCGACA-3’ and 5’-AAACTGTCGCTGGACGTCATCTTC-3’	This study	N/A
Cand1 targeting sequences (pX335)-1: 5’-CACCGCAAATTGGAAATGTGGTACG-3’ and 5’-AAACCGTACCACATTTCCAATTTGC-3’	This study	N/A
Cand1 targeting sequences (pX335)-2: 5’-CACCGCATCCAGCGACAAGGACTTT-3’ and 5’-AAACAAAGTCCTTGTCGCTGGATGC-3’	This study	N/A
Cand2 genotyping primers: 5’-AGCTGGCACCTACGGGAATAACAAGGA-3’ an 5’-ACACACACGAGGGAGGAGAG-3’	This study	N/A
Cand1 genotyping primers: 5’-TGTCTGGCTCCCCGTAGAGGCCCTTCT-3’ and 5’-CCTATTCGCTTGCCATCCT-3’	This study	N/A
Recombinant DNA		
pGEX-Cand1	Pierce et al., 2013	RDB 2562
pGEX-$^{\Delta H1}$Cand1	This study	XL 008
pGEX-Cand1$^{1-603}$	This study	XL 063
pGEX-Cand1$^{604-1230}$	This study	XL 081
pGEX-Cul1•Rbx1	Gift from N. Zheng	RDB 2080, 2081

pGEX-Cul1$^{\text{Sortase-Tag}}$•Rbx1	This study	RDB 2080, 2557
pGEX-Skp1•Skp2	Gift from N. Zheng	RDB 2047
pGEX-Skp1ΔΔ•Skp2	This study	RDB 2814, XL 18
pGEX-Skp1	Pierce et al., 2013	RDB 2435
pGEX-DCN1	Gift from N. Zheng	RDB 3386
pX335-U6-Chimeric_BB-CBh-hSpCas9n(D10A)	Ran et al., 2013	Addgene Plasmid # 42335
pGEX Cand2 donor plasmid	This study	XL 051
pGEX Cand1 donor plasmid	This study	XL 052
pOG44 Flp-Recombinase	Thermo Fisher Scientific	Cat # V600520
pcDNA5/FRT/TO Cand1$^{\text{HA}}$	This study	XL 082
pcDNA5/FRT/TO $^{\text{3xFLAG}}$Cul1	This study	XL 080
pcDNA5/FRT/TO $^{\text{3xFLAG}}$IκBα	This study	XL 087
pcDNA5/FRT/TO $^{\text{2xStrepII}}$β-TrCP	This study	XL 095
psPAX2	Reitsma et al., 2017	N/A
pMD.2G	Reitsma et al., 2017	N/A
pCDH-EF1-MCS-IRES-NEO: $^{\text{HA}}$FBXO6	Reitsma et al., 2017	RDB 3385
pCDH-EF1-MCS-IRES-NEO: $^{\text{HA}}$FBXO6ΔFbox	This study	XL 120
pCDH-EF1-MCS-IRES-NEO: $^{\text{HA}}$FBXL16	This study	XL 121
pCDH-EF1-MCS-IRES-NEO: $^{\text{HA}}$Skp2	This study	XL 122
pCDH-EF1-MCS-IRES-NEO: $^{\text{HA}}$Skp2ΔLRR	This study	XL 123
Software and Algorithms		
Prism	GraphPad	RRID:SCR_002798
MATLAB	MathWorks	RRID:SCR_001622
ImageJ	NIH	RRID:SCR_003070
Other		
DMEM	Thermo Fisher Scientific	Cat # BW12-614Q
Tet system approved fetal bovine serum	Clontech	Cat # 631367
Trypsin-EDTA (0.25%)	Thermo Fisher Scientific	Cat # 25200056
ANTI-FLAG M2 Affinity Gel antibody	Sigma	Cat # A2220
EZview(TM) Red anti-HA Affinity Gel antibody	Sigma	Cat # E6779
Glutathione Sepharose 4B	GE Healthcare	Cat # 45-000-139
Lipofectamine 3000	Thermo Fisher Scientific	Cat # L3000008

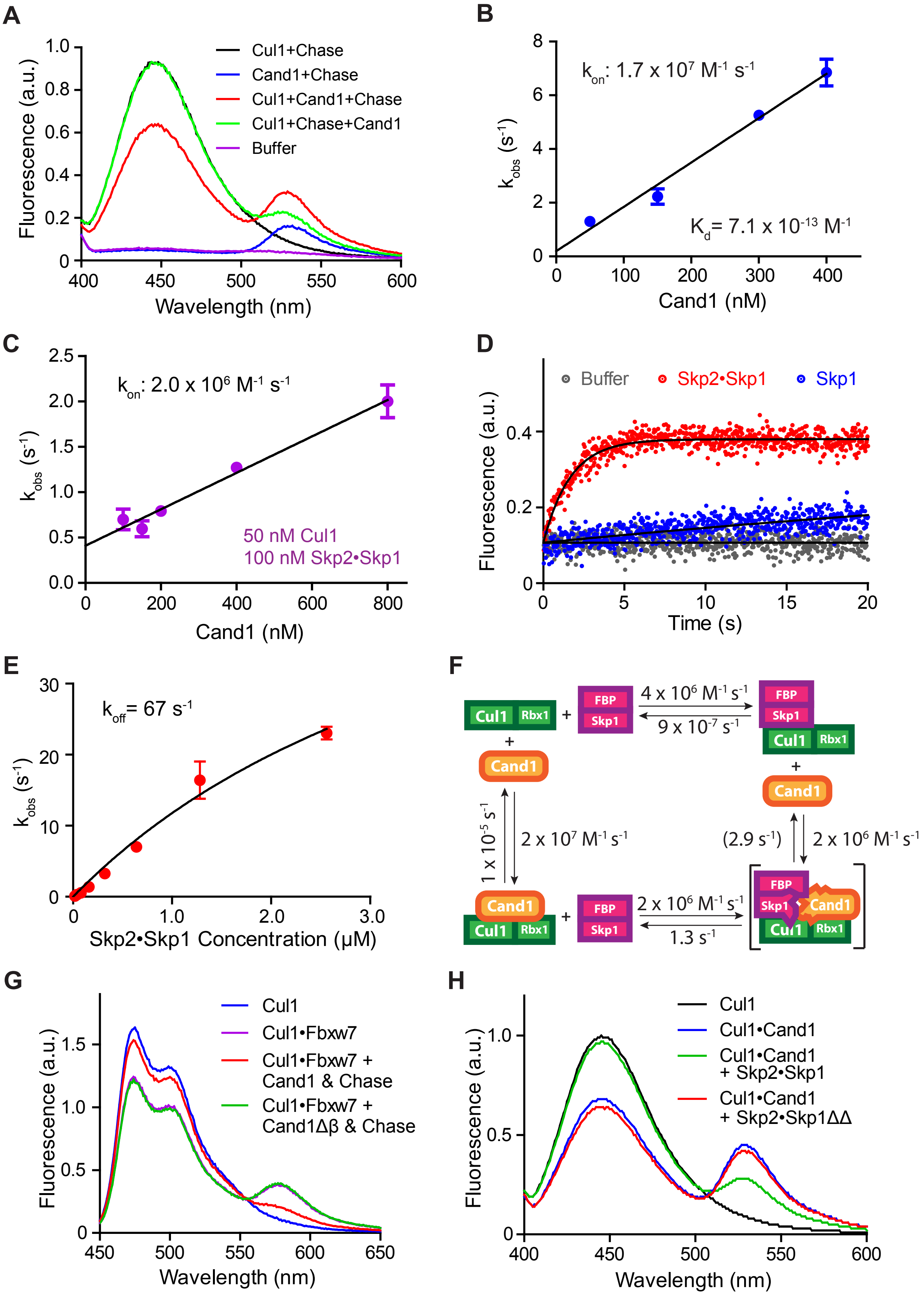
A
Fluorescence (a.u.)
1.0
0.8
0.6
0.4
0.2
0
400
450
500
550
600
Wavelength (nm)
Cul1+Chase
Cand1+Chase
Cul1+Cand1+Chase
Cul1+Chase+Cand1
Buffer
B
k_{obs} (s^{-1})
8
6
4
2
0
100
200
300
400
Cand1 (nM)
k_{on}: 1.7 x 10^{7} M^{-1} s^{-1}
K_d= 7.1 x 10^{-13} M^{-1}
C
k_{obs} (s^{-1})
2.5
2.0
1.5
1.0
0.5
0.0
0
200
400
600
800
Cand1 (nM)
k_{on}: 2.0 x 10^{6} M^{-1} s^{-1}
50 nM Cul1
100 nM Skp2•Skp1
D
Fluorescence (a.u.)
Buffer
Skp2•Skp1
Skp1
0.4
0.2
0
5
10
15
20
Time (s)
E
k_{obs} (s^{-1})
30
20
10
0
1.0
2.0
3.0
Skp2•Skp1 Concentration (μM)
k_{off}= 67 s^{-1}
F
Cul1
Rbx1
+
FBP
Skp1
4 x 10^{6} M^{-1} s^{-1}
9 x 10^{-7} s^{-1}
Cand1
1 x 10^{-5} s^{-1}
2 x 10^{7} M^{-1} s^{-1}
(2.9 s^{-1})
2 x 10^{6} M^{-1} s^{-1}
2 x 10^{6} M^{-1} s^{-1}
1.3 s^{-1}
G
Fluorescence (a.u.)
1.5
1.0
0.5
0
450
500
550
600
650
Wavelength (nm)
Cul1
Cul1•Fbxw7
Cul1•Fbxw7 + Cand1 & Chase
Cul1•Fbxw7 + Cand1Δβ & Chase
H
Fluorescence (a.u.)
1.0
0.5
0
400
450
500
550
600
Wavelength (nm)
Cul1
Cul1•Cand1
Cul1•Cand1 + Skp2•Skp1
Cul1•Cand1 + Skp2•Skp1ΔΔ

Figure 1

Figure 2

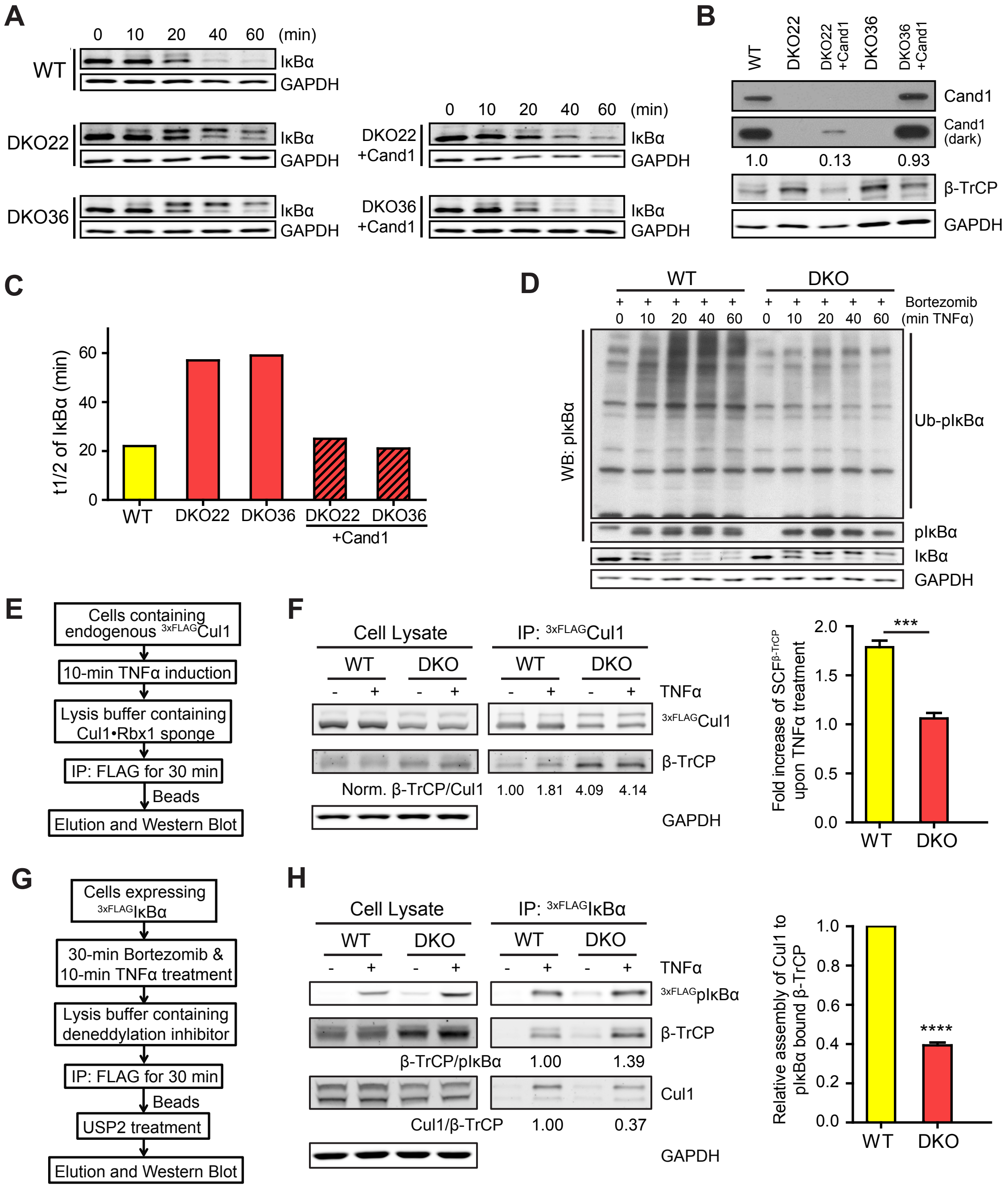

Figure 2

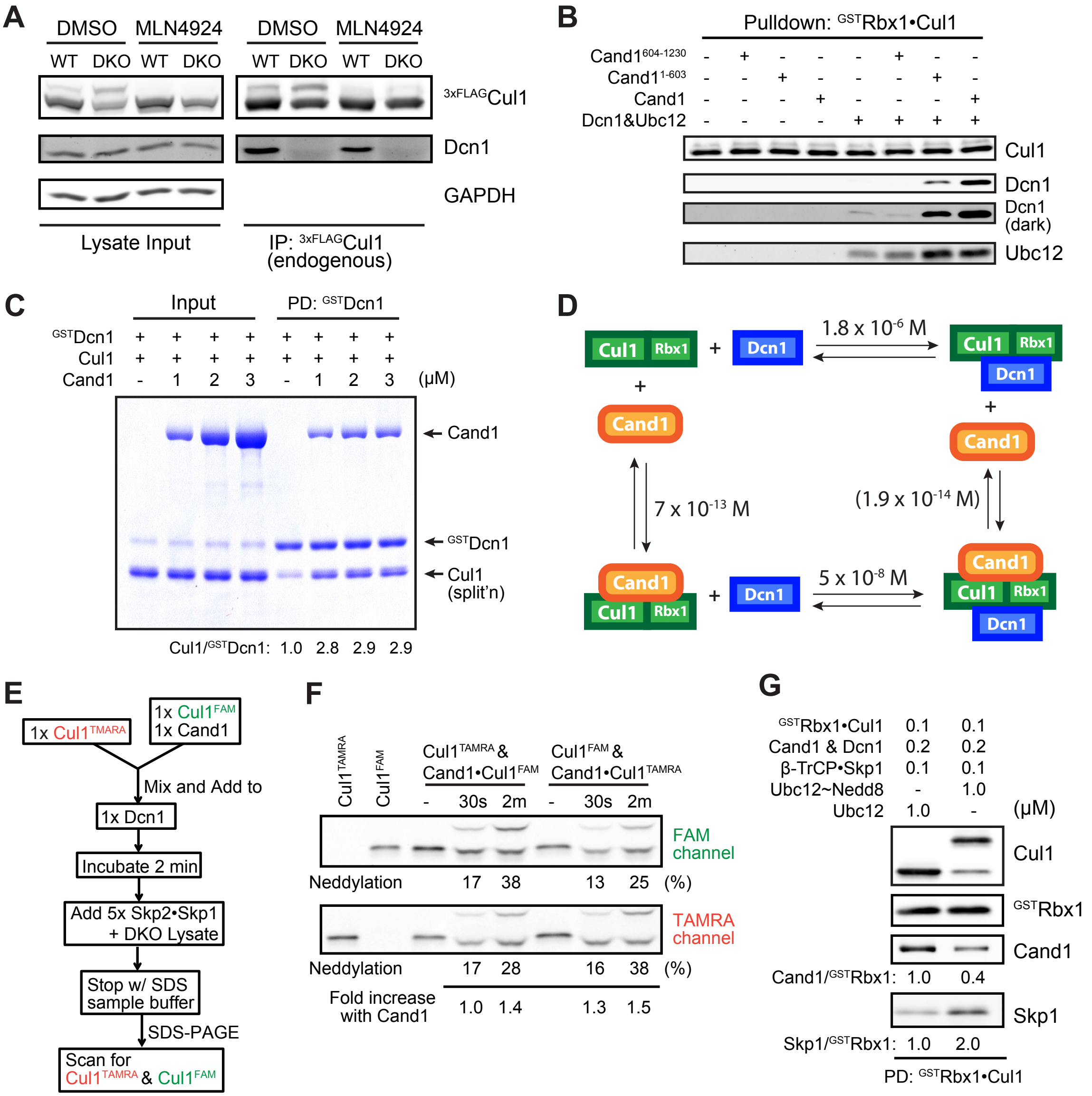
A
DMSO
MLN4924
DMSO
MLN4924
WT DKO WT DKO
WT DKO WT DKO
3xFLAGCul1
Dcn1
GAPDH
Lysate Input
IP: 3xFLAGCul1 (endogenous)
B
Pulldown: GSTRbx1•Cul1
Cand1604-1230 - + - - - + - -
Cand11-603 - - + - - - + -
Cand1 - - - + - - - +
Dcn1&Ubc12 - - - - + + + +
Cul1
Dcn1
Dcn1 (dark)
Ubc12
C
Input
PD: GSTDcn1
GSTDcn1 + + + + + + + +
Cul1 + + + + + + + +
Cand1 - 1 2 3 - 1 2 3 (μM)
Cand1
GSTDcn1
Cul1 (split'n)
Cul1/GSTDcn1: 1.0 2.8 2.9 2.9
D
Cul1 Rbx1
Dcn1
1.8 x 10-6 M
Cand1
7 x 10-13 M
(1.9 x 10-14 M)
5 x 10-8 M
E
1x Cul1TMARA
1x Cul1FAM
1x Cand1
Mix and Add to
1x Dcn1
Incubate 2 min
Add 5x Skp2•Skp1 + DKO Lysate
Stop w/ SDS sample buffer
SDS-PAGE
Scan for Cul1TAMRA & Cul1FAM
F
Cul1TAMRA
Cul1FAM
Cul1TAMRA & Cand1•Cul1FAM
Cul1FAM & Cand1•Cul1TAMRA
- 30s 2m - 30s 2m
FAM channel
Neddylation 17 38 13 25 (%)
TAMRA channel
Neddylation 17 28 16 38 (%)
Fold increase with Cand1 1.0 1.4 1.3 1.5
G
GSTRbx1•Cul1 0.1 0.1
Cand1 & Dcn1 0.2 0.2
β-TrCP•Skp1 0.1 0.1
Ubc12~Nedd8 - 1.0
Ubc12 1.0 - (μM)
Cul1
GSTRbx1
Cand1
Cand1/GSTRbx1: 1.0 0.4
Skp1
Skp1/GSTRbx1: 1.0 2.0
PD: GSTRbx1•Cul1

Figure 3

Figure 4

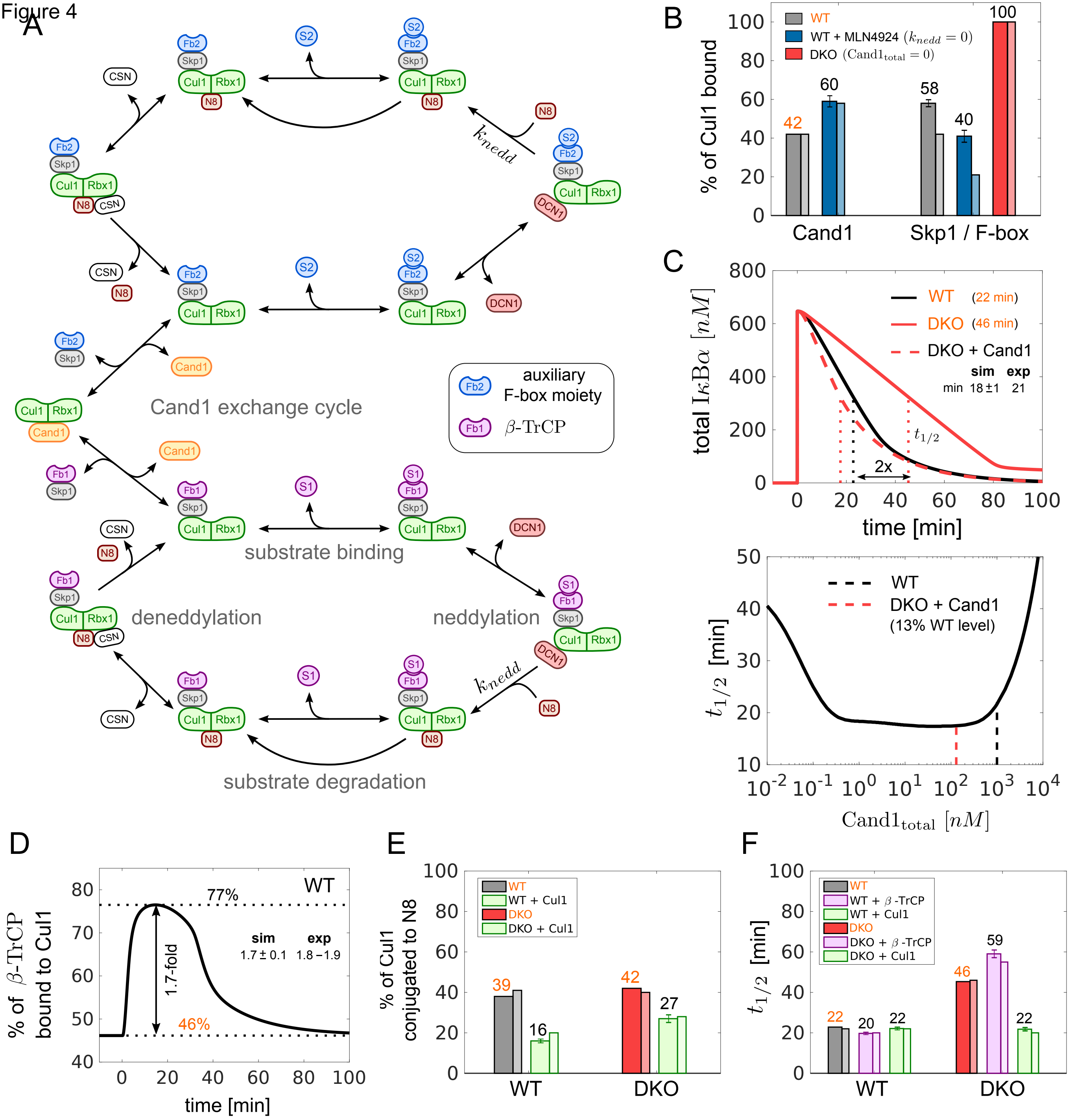
A
CSN
Fb2
Skp1
Cul1
Rbx1
N8
S2
DCN1
k_{nedd}
Cand1
Cand1 exchange cycle
auxiliary F-box moiety
Fb1
β-TrCP
S1
substrate binding
deneddylation
neddylation
substrate degradation
B
% of Cul1 bound
WT
WT + MLN4924 ($k_{nedd} = 0$)
DKO ($\mathrm{Cand1_{total}} = 0$)
42
60
58
40
100
Cand1
Skp1 / F-box
0
20
40
60
80
100
C
total $\mathrm{I\kappa B\alpha}$ [nM]
WT (22 min)
DKO (46 min)
DKO + Cand1
sim exp
min 18±1 21
$t_{1/2}$
2x
time [min]
0
20
40
60
80
100
200
400
600
800
$t_{1/2}$ [min]
WT
DKO + Cand1
(13% WT level)
10
20
30
40
50
10^{-2} 10^{-1} 10^{0} 10^{1} 10^{2} 10^{3} 10^{4}
$\mathrm{Cand1_{total}}$ [nM]
D
% of β-TrCP bound to Cul1
WT
77%
46%
1.7-fold
sim exp
1.7 ± 0.1 1.8 – 1.9
time [min]
40
50
60
70
80
0
20
40
60
80
100
E
% of Cul1 conjugated to N8
WT
WT + Cul1
DKO
DKO + Cul1
39
16
42
27
WT
DKO
0
20
40
60
80
100
F
$t_{1/2}$ [min]
WT
WT + β-TrCP
WT + Cul1
DKO
DKO + β-TrCP
DKO + Cul1
22
20
22
46
59
22
WT
DKO
0
20
40
60
80
100

Figure 5

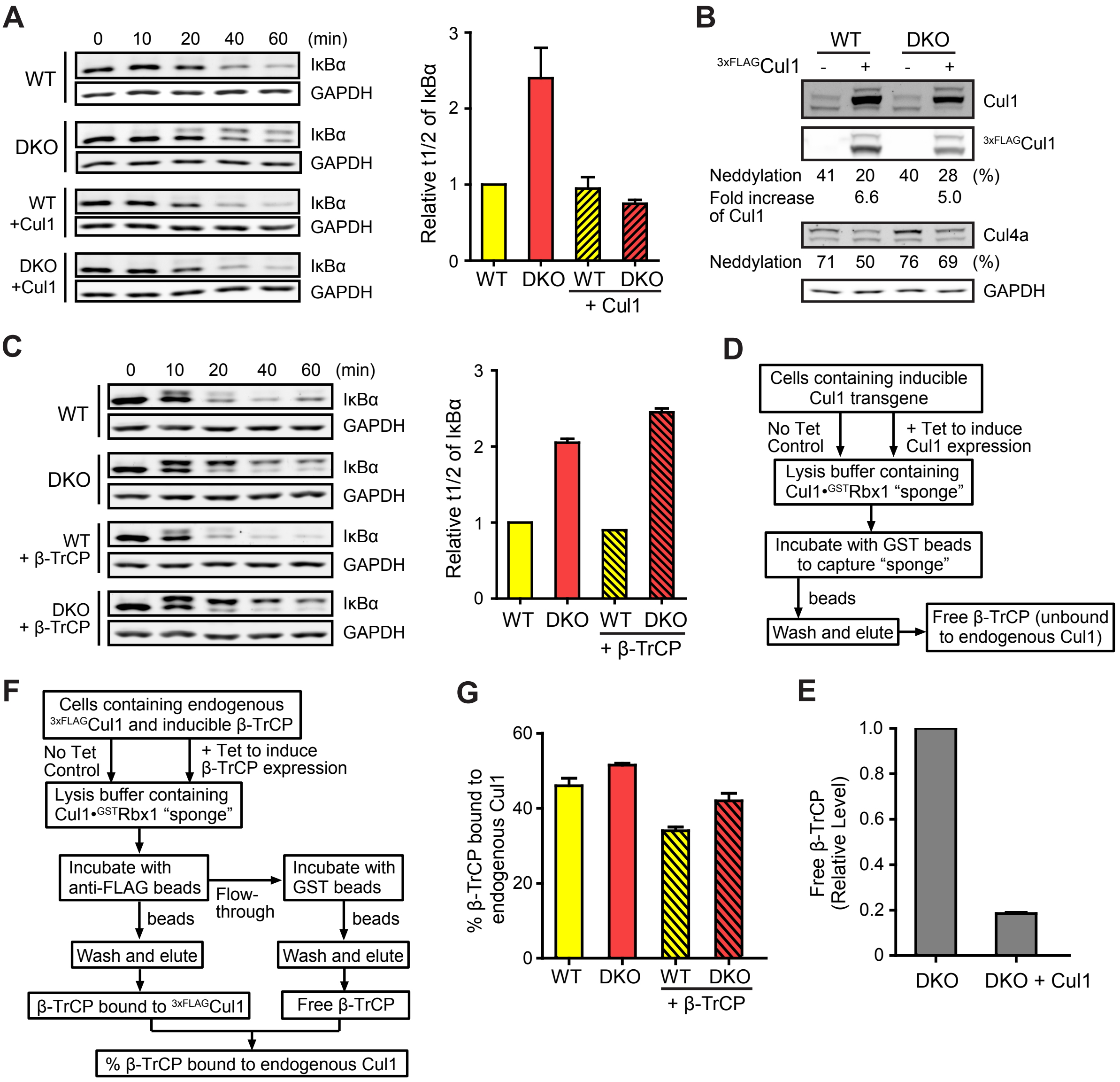

Figure 5

Figure 6

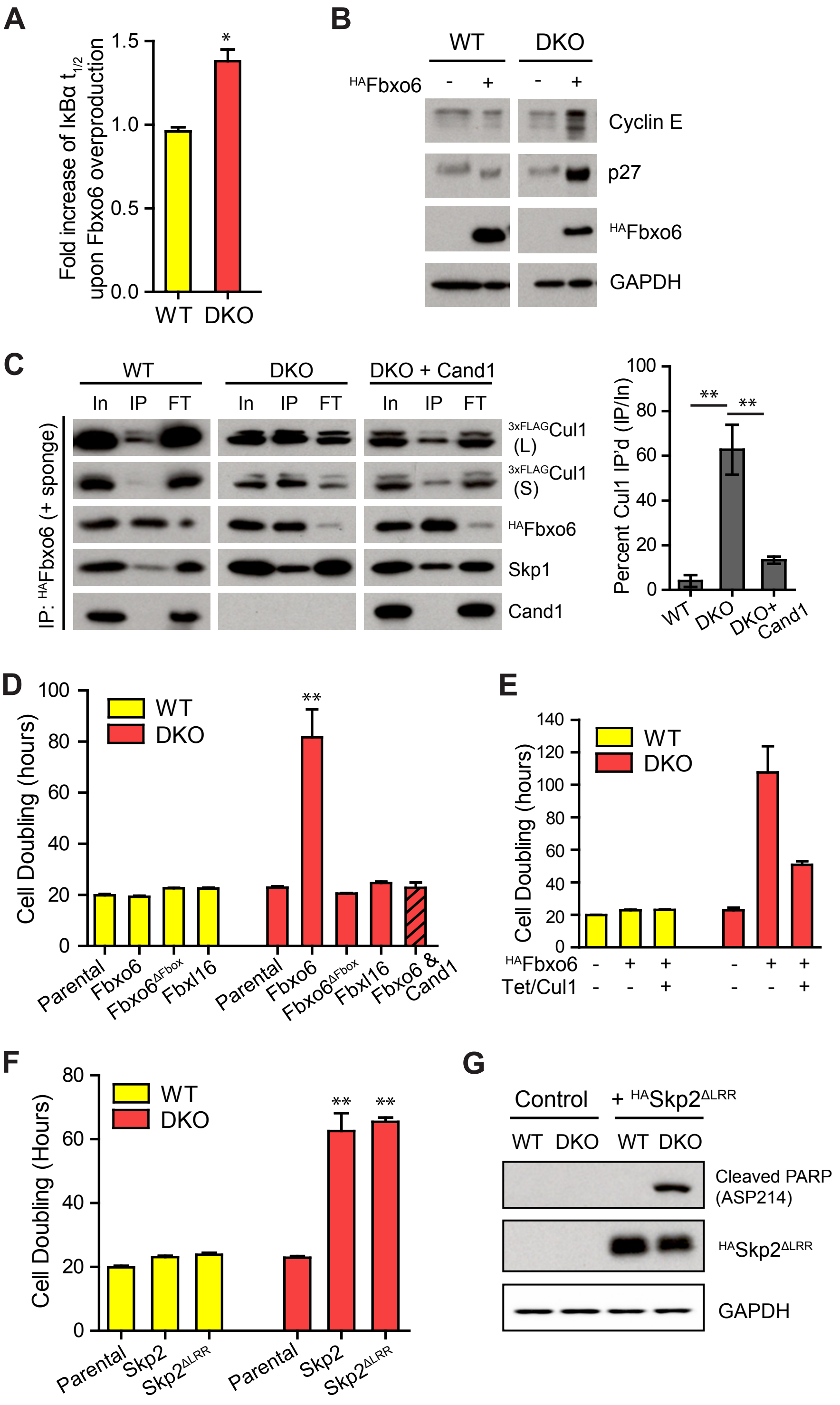

Figure 6

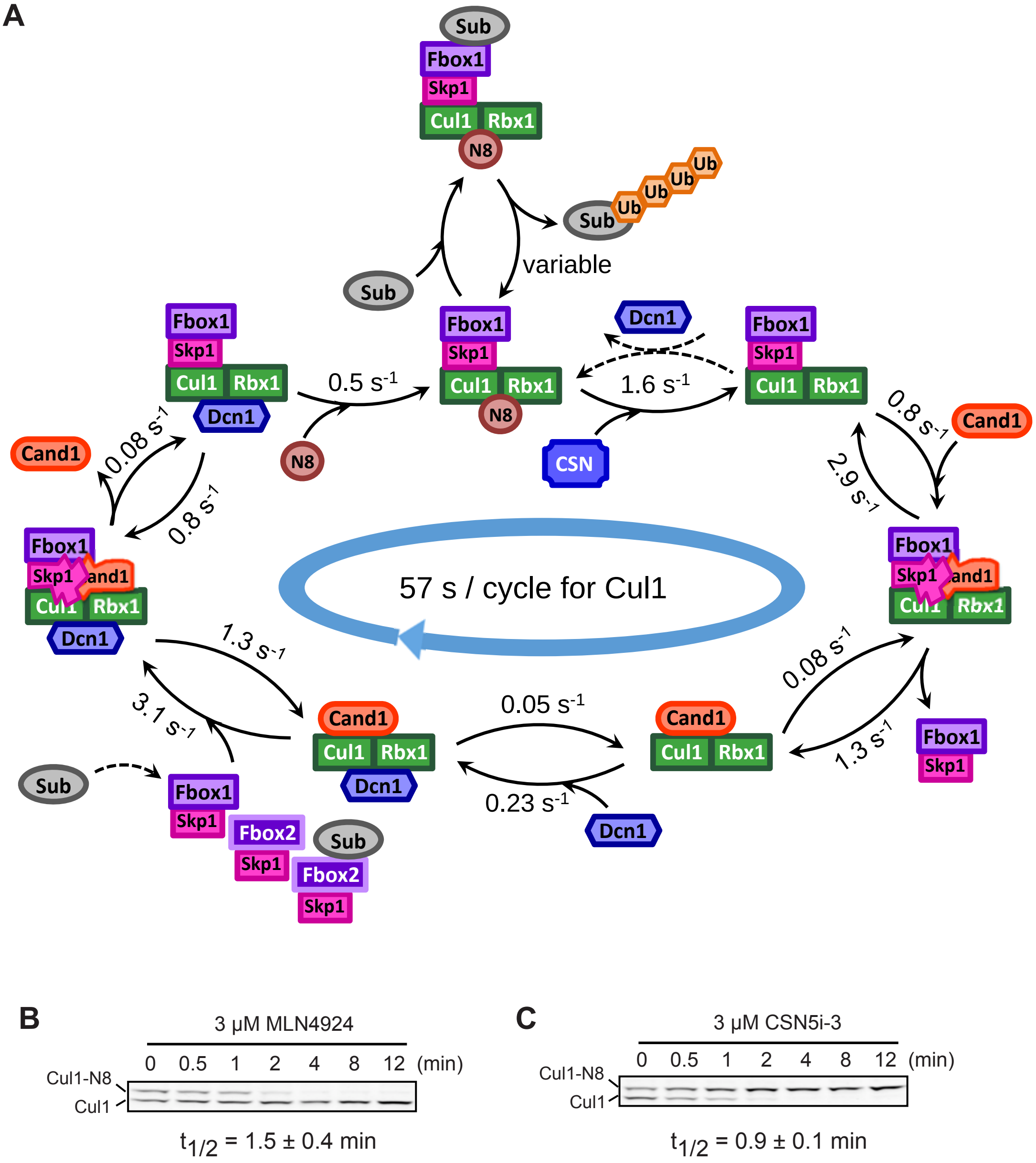
A
Sub
Fbox1
Skp1
Cul1
Rbx1
N8
Ub
variable
Dcn1
0.5 s-1
1.6 s-1
CSN
Cand1
0.08 s-1
0.8 s-1
2.9 s-1
57 s / cycle for Cul1
1.3 s-1
3.1 s-1
0.05 s-1
0.23 s-1
Fbox2
B
3 µM MLN4924
0 0.5 1 2 4 8 12 (min)
Cul1-N8
Cul1
t1/2 = 1.5 ± 0.4 min
C
3 µM CSN5i-3
0 0.5 1 2 4 8 12 (min)
Cul1-N8
Cul1
t1/2 = 0.9 ± 0.1 min

Figure 7

Supplemental Figures

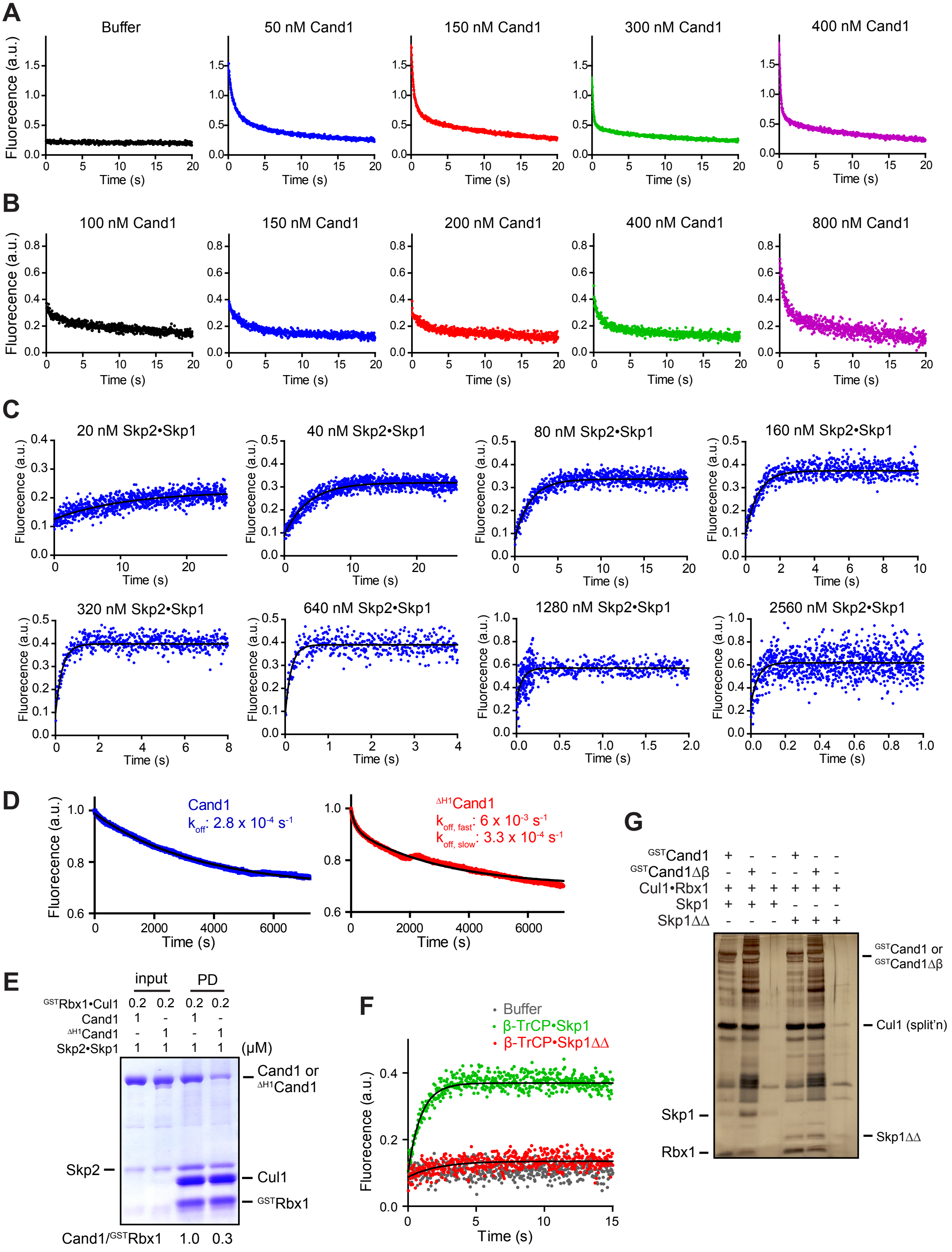

Figure S1

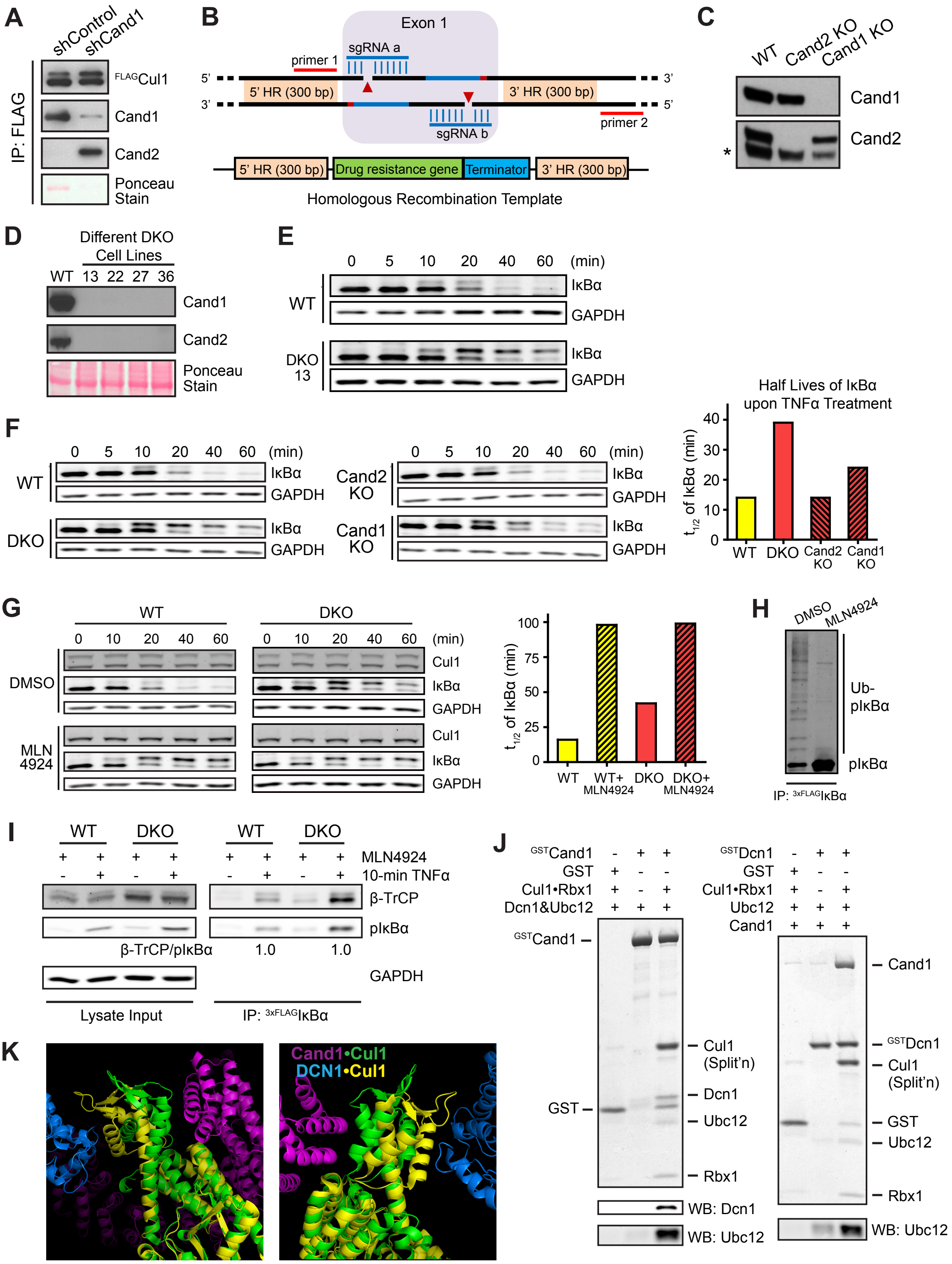
A
shControl
shCand1
IP: FLAG
FLAGCul1
Cand1
Cand2
Ponceau Stain
B
Exon 1
sgRNA a
primer 1
5'
3'
5' HR (300 bp)
3' HR (300 bp)
sgRNA b
primer 2
5' HR (300 bp)
Drug resistance gene
Terminator
3' HR (300 bp)
Homologous Recombination Template
C
WT
Cand2 KO
Cand1 KO
Cand1
Cand2
*
D
Different DKO Cell Lines
WT 13 22 27 36
Cand1
Cand2
Ponceau Stain
E
0 5 10 20 40 60 (min)
WT
IκBα
GAPDH
DKO 13
IκBα
GAPDH
F
0 5 10 20 40 60 (min)
WT
DKO
Cand2 KO
Cand1 KO
IκBα
GAPDH
Half Lives of IκBα upon TNFα Treatment
t1/2 of IκBα (min)
0 10 20 30 40
WT
DKO
Cand2 KO
Cand1 KO
G
WT
DKO
0 10 20 40 60 (min)
DMSO
MLN 4924
Cul1
IκBα
GAPDH
t1/2 of IκBα (min)
0 25 50 75 100
WT
WT+ MLN4924
DKO
DKO+ MLN4924
H
DMSO
MLN4924
Ub-pIκBα
pIκBα
IP: 3xFLAGIκBα
I
WT
DKO
WT
DKO
+ + + + + + + +
MLN4924
- + - + - + - +
10-min TNFα
β-TrCP
pIκBα
β-TrCP/pIκBα 1.0 1.0
GAPDH
Lysate Input
IP: 3xFLAGIκBα
J
GSTCand1 - + +
GST + - -
Cul1•Rbx1 + - +
Dcn1&Ubc12 + + +
GSTCand1
GST
Cul1 (Split'n)
Dcn1
Ubc12
Rbx1
WB: Dcn1
WB: Ubc12
GSTDcn1 - + +
GST + - -
Cul1•Rbx1 + - +
Ubc12 + + +
Cand1 + + +
Cand1
GSTDcn1
Cul1 (Split'n)
GST
Ubc12
Rbx1
WB: Ubc12
K
Cand1•Cul1
DCN1•Cul1

Figure S2

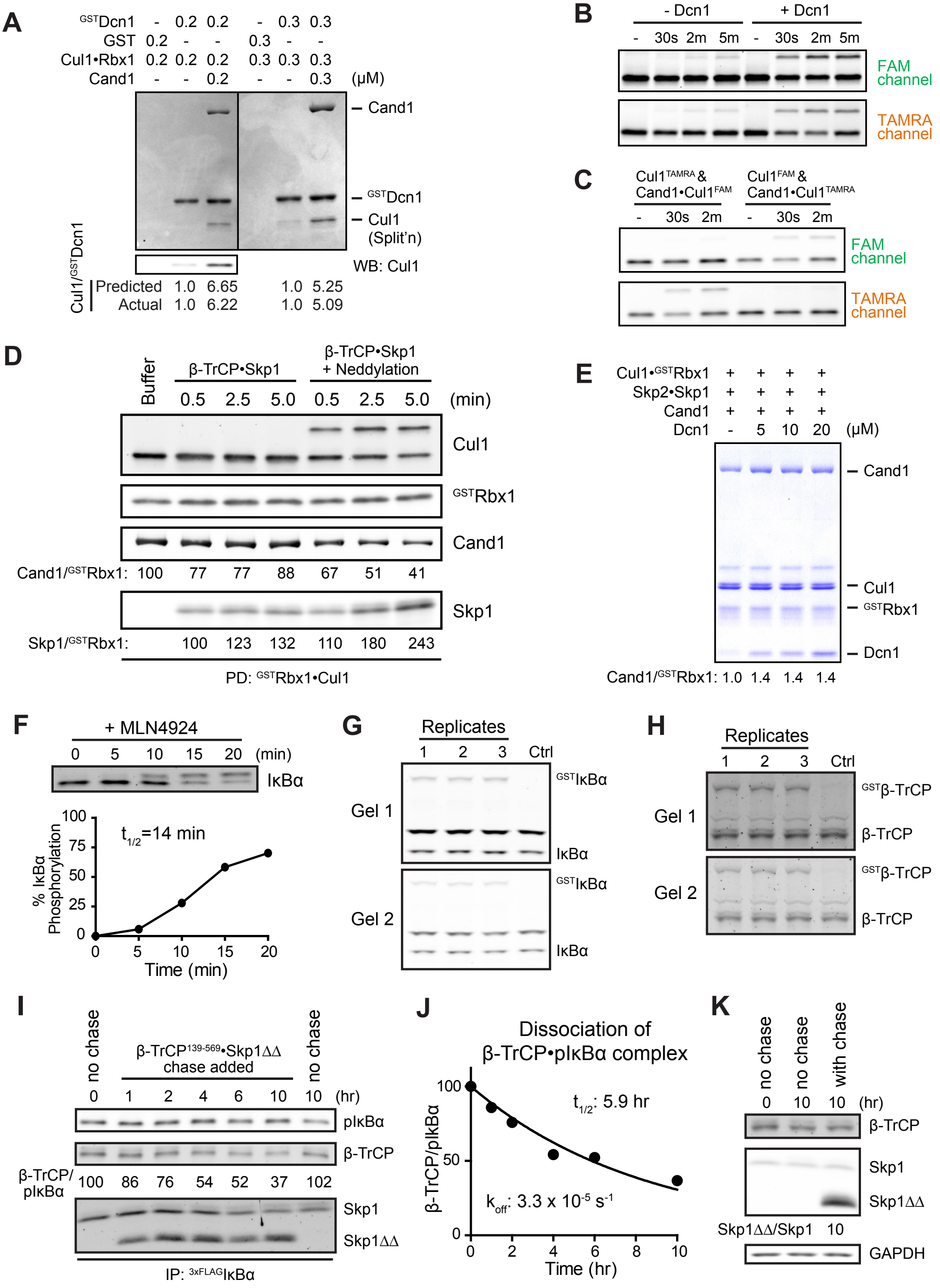
A
GSTDcn1 - 0.2 0.2 - 0.3 0.3
GST 0.2 - - 0.3 - -
Cul1•Rbx1 0.2 0.2 0.2 0.3 0.3 0.3
Cand1 - - 0.2 - - 0.3 (μM)
Cand1
GSTDcn1
Cul1 (Split'n)
WB: Cul1
Cul1/GSTDcn1
Predicted 1.0 6.65 1.0 5.25
Actual 1.0 6.22 1.0 5.09
B
- Dcn1
+ Dcn1
- 30s 2m 5m - 30s 2m 5m
FAM channel
TAMRA channel
C
Cul1TAMRA & Cand1•Cul1FAM
Cul1FAM & Cand1•Cul1TAMRA
- 30s 2m - 30s 2m
FAM channel
TAMRA channel
D
Buffer
β-TrCP•Skp1
β-TrCP•Skp1 + Neddylation
0.5 2.5 5.0 0.5 2.5 5.0 (min)
Cul1
GSTRbx1
Cand1
Cand1/GSTRbx1: 100 77 77 88 67 51 41
Skp1
Skp1/GSTRbx1: 100 123 132 110 180 243
PD: GSTRbx1•Cul1
E
Cul1•GSTRbx1 + + + +
Skp2•Skp1 + + + +
Cand1 + + + +
Dcn1 - 5 10 20 (μM)
Cand1
Cul1
GSTRbx1
Dcn1
Cand1/GSTRbx1: 1.0 1.4 1.4 1.4
F
+ MLN4924
0 5 10 15 20 (min)
IκBα
t1/2=14 min
% IκBα Phosphorylation
100
75
50
25
0
0 5 10 15 20
Time (min)
G
Replicates
1 2 3 Ctrl
Gel 1
Gel 2
GSTIκBα
IκBα
H
Replicates
1 2 3 Ctrl
Gel 1
Gel 2
GSTβ-TrCP
β-TrCP
I
no chase
β-TrCP139-569•Skp1ΔΔ chase added
no chase
0 1 2 4 6 10 10 (hr)
pIκBα
β-TrCP
β-TrCP/pIκBα 100 86 76 54 52 37 102
Skp1
Skp1ΔΔ
IP: 3xFLAGIκBα
J
Dissociation of β-TrCP•pIκBα complex
t1/2: 5.9 hr
koff: 3.3 x 10-5 s-1
β-TrCP/pIκBα
100
50
0
0 2 4 6 8 10
Time (hr)
K
no chase
no chase
with chase
0 10 10 (hr)
β-TrCP
Skp1
Skp1ΔΔ
Skp1ΔΔ/Skp1 10
GAPDH

Figure S3

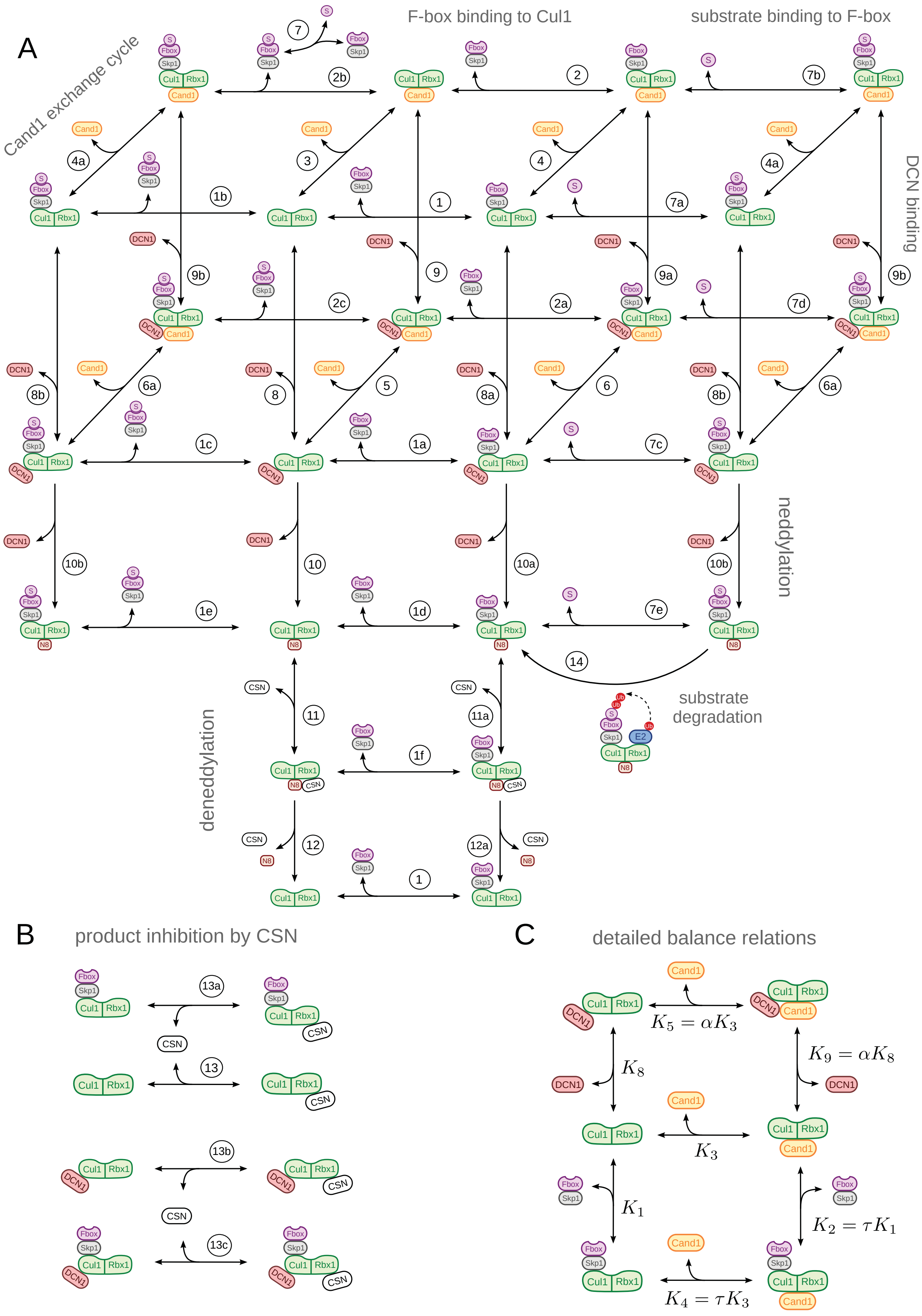
A
Cand1 exchange cycle
F-box binding to Cul1
substrate binding to F-box
DCN binding
neddylation
deneddylation
substrate degradation
1
1a
1b
1c
1d
1e
1f
2
2a
2b
2c
3
4
4a
5
6
6a
7
7a
7b
7c
7d
7e
8
8a
8b
9
9a
9b
10
10a
10b
11
11a
12
12a
14
S
Fbox
Skp1
Cul1
Rbx1
Cand1
DCN1
N8
CSN
Ub
E2
B
product inhibition by CSN
13
13a
13b
13c
C
detailed balance relations
$K_5 = \alpha K_3$
$K_9 = \alpha K_8$
K_8
K_3
K_1
$K_2 = \tau K_1$
$K_4 = \tau K_3$

Figure S4

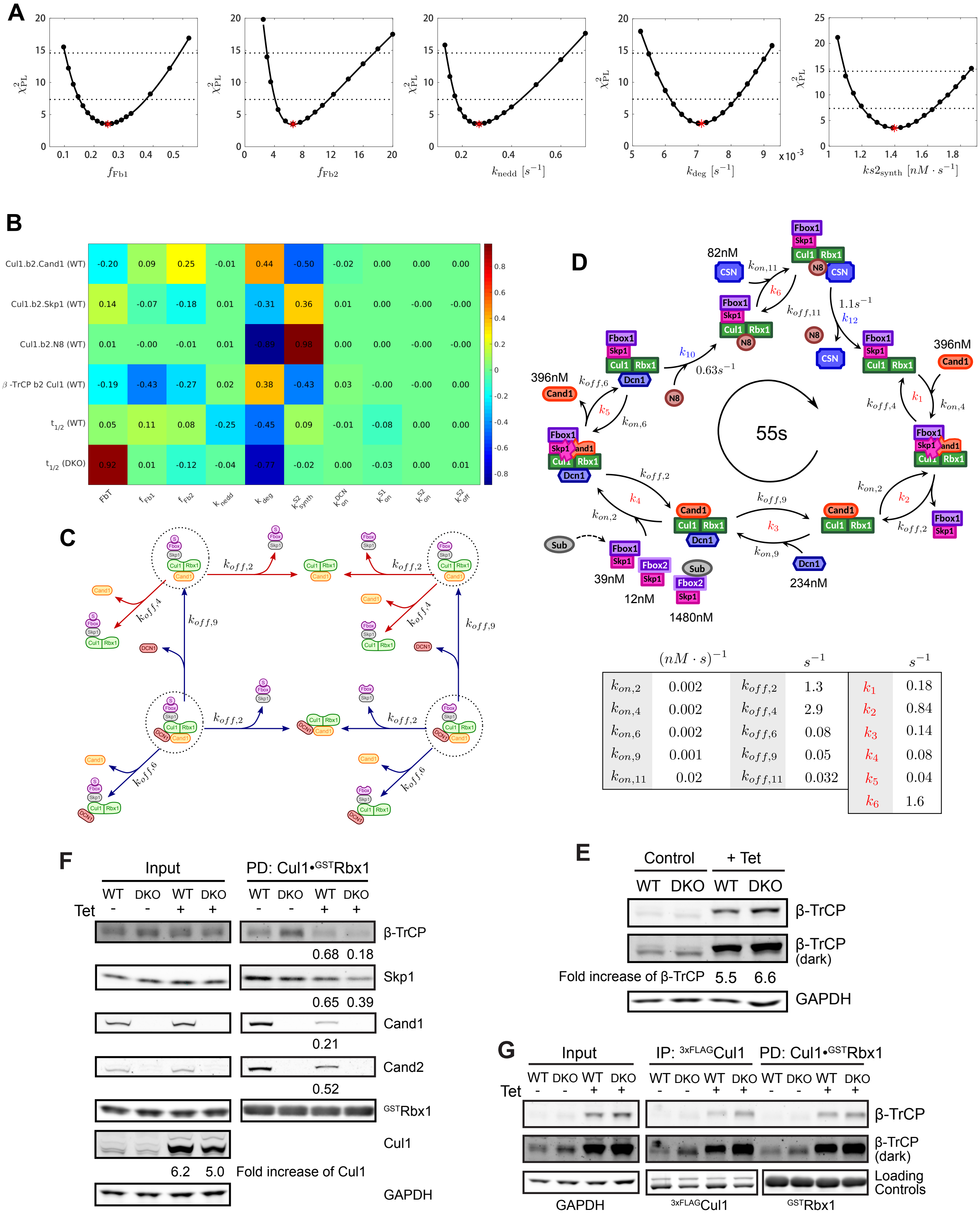

	$(nM \cdot s)^{-1}$		s^{-1}		s^{-1}
$k_{on,2}$	0.002	$k_{off,2}$	1.3	k_1	0.18
$k_{on,4}$	0.002	$k_{off,4}$	2.9	k_2	0.84
$k_{on,6}$	0.002	$k_{off,6}$	0.08	k_3	0.14
$k_{on,9}$	0.001	$k_{off,9}$	0.05	k_4	0.08
$k_{on,11}$	0.02	$k_{off,11}$	0.032	k_5	0.04
				k_6	1.6

Figure S5

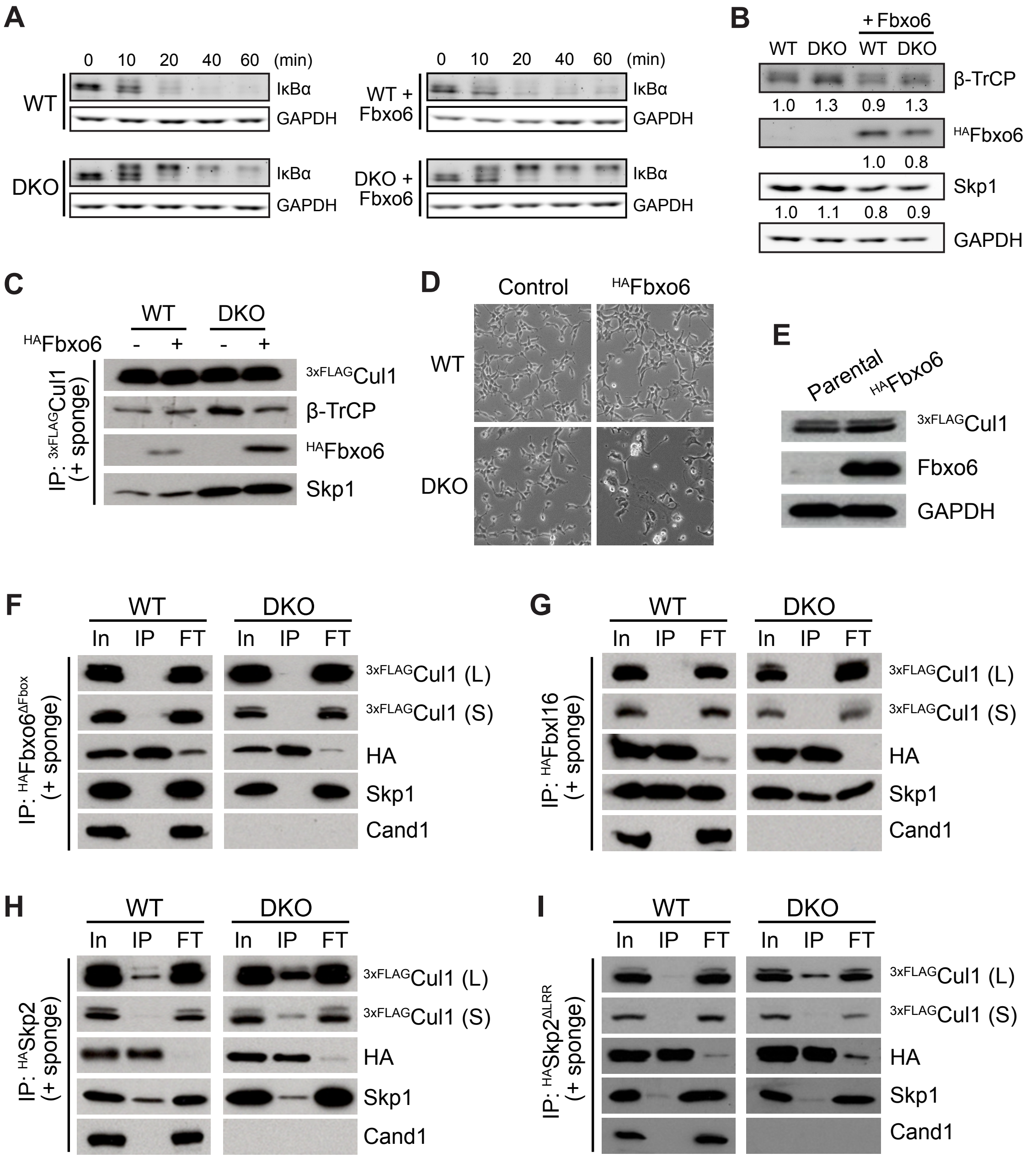

J

F-box Protein	% Cul1 Bound (WT)	% Cul1 Bound (DKO)
^{HA}Fbxo6$^{\Delta F\text{-}box}$	0.0	0.0
^{HA}Fbxl16	0.0	0.0
^{HA}Skp2	2.0	25.3
^{HA}Skp2$^{\Delta LRR}$	2.4	25.1

Figure S6

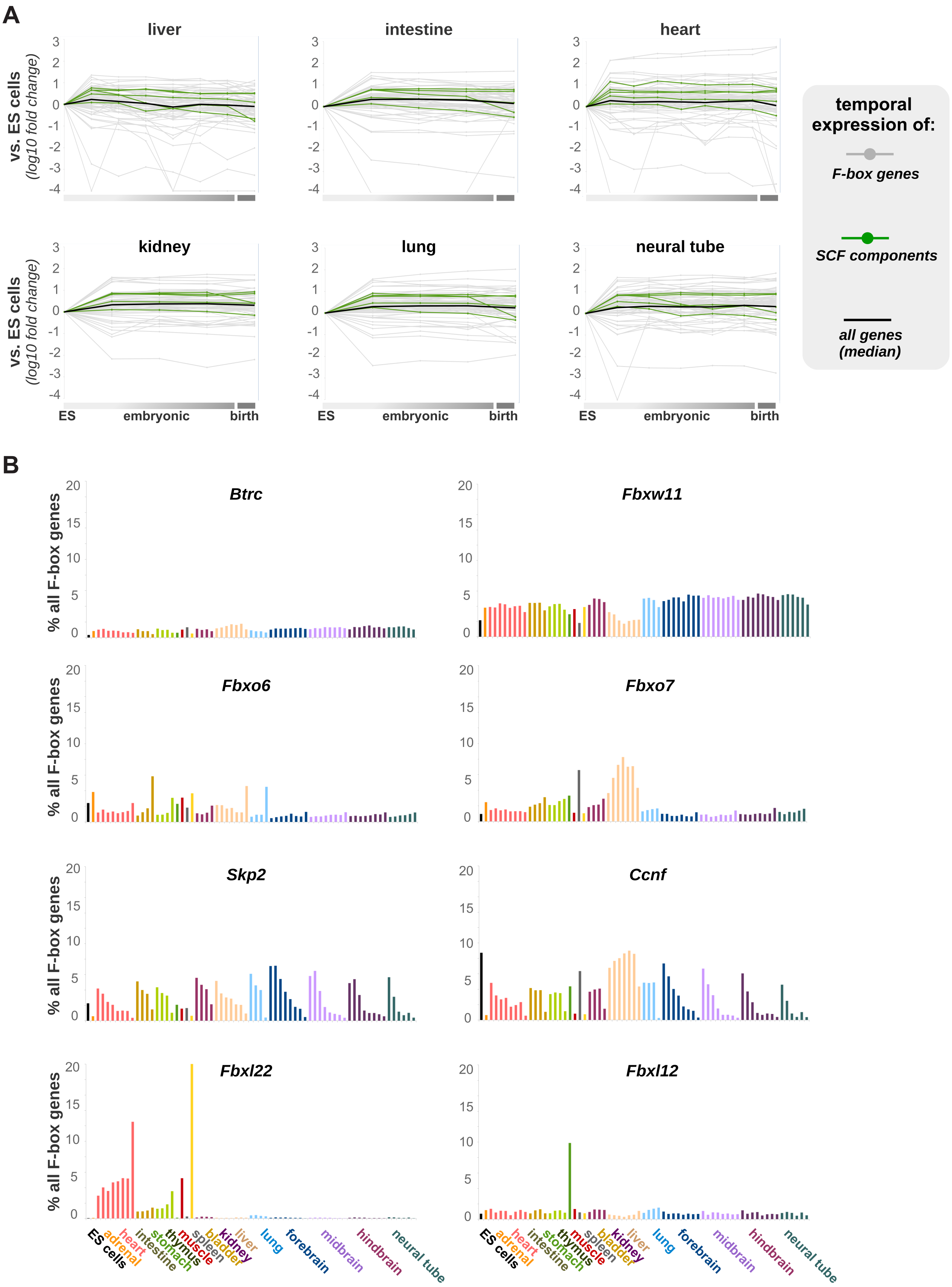
A
liver
intestine
heart
kidney
lung
neural tube
vs. ES cells
(log10 fold change)
3
2
1
0
-1
-2
-3
-4
ES
embryonic
birth
temporal expression of:
F-box genes
SCF components
all genes (median)
B
Btrc
Fbxw11
Fbxo6
Fbxo7
Skp2
Ccnf
Fbxl22
Fbxl12
% all F-box genes
20
15
10
5
0
ES cells
adrenal
heart
intestine
stomach
thymus
muscle
spleen
bladder
kidney
liver
lung
forebrain
midbrain
hindbrain
neural tube

Figure S7

SUPPLEMENTAL FIGURE LEGENDS

Figure S1. Properties of Cul1•Cand1 complex assembly and disassembly (related to Figure 1).

(A) k_{obs} for Cand1 binding to Cul1. The change in donor fluorescence versus time was measured in a stopped-flow fluorimeter upon addition of varying concentrations of $^{FlAsH\Delta H1}$Cand1 to 50 nM Cul1^{AMC}•Rbx1. Indicated concentrations are after 1:1 (v:v) mixing of the two solutions in the stopped-flow fluorimeter. Signal changes were fit to two phase exponential curves, and the fast-phase rates were used as k_{obs}. These values are plotted against [Cand1] in Fig 1B.

(B) k_{obs} for Cand1 binding to Cul1 preassembled with Skp1•Skp2. Similar to Fig S1A, except 100 nM Skp1•Skp2 was preincubated with 50 nM Cul1^{AMC}. Signal changes were fit to two phase exponential curves, and the fast-phase rates were used as k_{obs}. These values are plotted against [Cand1] in Fig 1C.

(C) k_{obs} for Cand1•Cul1 dissociation by Skp1•Skp2. The change in donor fluorescence versus time was measured in a stopped-flow fluorimeter upon addition of varying concentrations of Skp1•Skp2 to 10 nM $^{FlAsH\Delta H1}$Cand1•Cul1^{AMC}•Rbx1. Indicated concentrations are after 1:1 (v:v) mixing of the two solutions in the stopped-flow fluorimeter. Signal changes were fit to single exponential curves. These values are plotted against [Skp1•Skp2] in Fig 1E.

(D) Replacing the first helix of Cand1 with the tetracysteine tag increased the k_{off} of Cand1 from Cul1•Rbx1. Fluorescence emission at 445 nm (donor emission) was detected every 2 seconds after the addition of 10 x excess $^{FlAsH\Delta H1}$Cand1 (acceptor protein) to Cul1^{AMC}•Rbx1 pre-incubated with unlabeled Cand1 or $^{\Delta H1}$Cand1. FRET was observed following spontaneous dissociation of non-fluorescent Cand1 from Cul1^{AMC}•Rbx1. Signal changes were fit to exponential curves with a fixed end point of 70% initial donor fluorescence. Cand1•Cul1^{AMC}•Rbx1 was fit to a one phase curve. $^{\Delta H1}$Cand1•Cul1^{AMC}•Rbx1 was fit to a two phase curve, with $k_{off,\ slow}$ similar to the k_{off} of Cand1•Cul1^{AMC}•Rbx1 and $k_{off,\ fast}$ about 20 times faster.

(E) $^{\Delta H1}$Cand1•Cul1•Rbx1 is less stable than Cand1•Cul1•Rbx1. Skp1•Skp2, Cul1•^{GST}Rbx1, Cand1 or $^{\Delta H1}$Cand1 at indicated concentrations were used in the GST pulldown (PD) assay. Relative level of recovered Cand1 is shown as Cand1:^{GST}Rbx1 ratio. Based on this result and the known K_D of Cul1•Skp1•Fbxw7, the K_D of $^{\Delta H1}$Cand1•Cul1 is simulated to be ~4.5 times higher than the K_D of Cand1•Cul1. In this and other experiments employing recombinant Cul1, it migrates faster than expected because it is expressed by the ‘split-n-coexpress’ (split’n) method of Li et al (2005).

(F) β-TrCP removes Cand1 from Cul1 when it is in complex with full length Skp1 but not Skp1 with loop regions deleted. The change in donor fluorescence versus time was measured in a stopped-flow apparatus upon addition of 75 nM Skp1•β-TrCP or Skp1ΔΔ•β-TrCP to 25 nM $^{\text{FlAsH}\Delta\text{H1}}$Cand1•Cul1$^{\text{AMC}}$•Rbx1.

(G) Deletion of β-hairpin in Cand1 or loop regions in Skp1 enables formation of a stable complex comprising Cul1, Skp1, and Cand1. *In vitro* pull-down assays containing the indicated proteins were performed to demonstrate the formation of stable complexes consisting of Cul1•Rbx1, Skp1 and $^{\text{GST}}$Cand1 when Cand1 and/or Skp1 was mutated to delete structural elements that are predicted to clash in the Cand1•Cul1•Rbx1•Skp1 complex. The indicated proteins were mixed in equimolar amounts and bound to glutathione-4B resin. Proteins associated with the resin were fractionated by SDS-PAGE and detected by silver stain.

Figure S2. Degradation defects in Cand1∆, Cand2∆, and Cand1/2 double knockout cells (related to Figure 2). Complex of Cand1•Cul1•Dcn1 (related to Figure 3).

(A) Cand2•Cul1 complex was detected only when Cand1 was depleted. IP-WB analysis of Cand1•Cul1 and Cand2•Cul1 complexes in control (shControl) and Cand1 knock-down (shCand1) cells that are stably expressing the shRNA (Pierce et. al., 2013). Cells were treated with 1 µg/ml tetracycline for 1 hour 24 hours before collection to induce expression of $^{\text{FLAG}}$Cul1 integrated at the FRT site (Flp-In system).

(B) Strategy for construction of Cand1/2 knockout cell lines. A pair of chimeric single-guide RNAs (sgRNA) guiding CRISPR Cas9 (D10A) nickases were designed to target the first exon of the Cand1 or Cand2 gene for mutagenesis. A homologous recombination (HR) template containing a drug resistance gene plus a translational terminator and two 300-bp homology arms that were identical to the genomic sequences flanking the first exon is depicted. Primer 1 and primer 2 were used to generate PCR products of the mutated genomic region for sequencing and confirming the complete inactivation of Cand1 and Cand2 genes. Note that primer 2 probed the region outside of the 300-bp HR region on the genomic DNA.

(C) Confirmation of Cand1 and Cand2 single KO cell lines. WB analysis showing the loss of Cand1 or Cand2 proteins in the corresponding KO cell lines. * marks a non-specific band, which serves as a loading control.

(D) Confirmation of Cand1/2 DKO cell lines. WB analysis showing the loss of Cand1 and Cand2 proteins in four DKO cell lines. DKO13, 22, 36 are independent cell lines confirmed by sequencing results. The filter stained with Ponceau S prior to probing is shown as a loading control. These lines initially displayed slower growth than the wild type (WT) cells, but the growth rate gradually increased after a few passages and became similar to the WT cells by the time their genotypes were confirmed.

(E) IκBα degradation is defective in DKO13 cells. WB analysis of IκBα levels in WT and DKO13 cells at indicated time points after TNFα treatment. DKO13 shows an IκBα degradation defect similar to the DKO22 and DKO36 lines shown in Fig 2A.

(F) Cand1 but not Cand2 is required for proper degradation of IκBα. WB analysis of IκBα degradation in response to TNFα treatment in WT, Cand1/2 DKO, Cand2 single knockout (Cand2 KO) and Cand1 KO cells. Half-lives of IκBα in this analysis are shown in the graph.

(G) Inhibiting neddylation stabilizes IκBα in both WT and DKO cells and enables quantification of the rate of IκBα phosphorylation. WB analysis of IκBα degradation in response to TNFα treatment in WT and DKO cells pretreated with either 0.1% DMSO or 1 µM MLN4924 for 1 hr. Half-lives of IκBα in this analysis are shown in the graph.

(H) Inhibiting neddylation strongly inhibits IκBα ubiquitination. Expression of ^{3xFLAG}IκBα cDNA integrated at the FRT site was induced with tetracycline for 24 hours and then ^{3xFLAG}IκBα was immunopreciptiated from cell lysate with anti-FLAG following pre-treatment of the cells with either 0.1% DMSO or 1 µM MLN4924 for 1 hr before 10-min TNFα treatment. IPs were evaluated by WB analysis with antibodies against pIκBα.

(I) pIκBα binds β-TrCP with equal efficiency in WT and DKO cells. WT and DKO cells expressing tetracycline-induced ^{3xFLAG}IκBα and treated with 1 µM MLN4924 for 1 hr to block pIκBα ubiquitination were lysed and subjected to IP with anti-FLAG followed by WB analysis with the indicated antibodies to evaluate interaction between pIκBα and β-TrCP. This is essentially the same as the experiment in Fig 2G, except that ubiquitination of pIκBα was suppressed by MLN4924, instead of by treating the IPs with deububiquitinating enzyme Usp2. MLN4924 or Usp2 were used to collapse all pIκBα species into a single band to facilitate quantification.

(J) Cand1 forms a complex with Dcn1 and Ubc12 only in the presence of Cul1. Reciprocal pull-down assays were set up as indicated. Each protein was included at 1 µM. Proteins adsorbed to the glutathione beads were fractionated by SDS-PAGE and stained by Coomassie blue or subjected to WB with the indicated antibodies.

(K) Binding of Cand1 alters the conformation of the Dcn1 binding site on Cul1. The C-terminal domains of Cul1 from PDB files of “4P5O” and “1U6G” were aligned in PyMOL, and the front and back views of the aligned Cand1•Cul1•Dcn1 are shown. Cand1 is in magenta and Dcn1 is in blue; Cul1 in complex with Cand1 is in green, and Cul1 in complex with Dcn1 is in yellow.

Figure S3. Cand1 and neddylation (related to Figure 3). Development of the computational model (related to Figure 4 and Method S1).

(A) Confirmation of the estimated K_D of 5 x 10^{-8} M for Dcn1 binding to Cand1•Cul1•Rbx1. Assays were similar to Fig 3C but lower concentrations of Cul1, Cand1 and ^{GST}Dcn1 were used. Proteins adsorbed to the glutathione beads were fractionated by SDS-PAGE and stained by Coomassie blue or subjected to WB with the Cul1 antibody. Fold increase of Cul1 recovered from the pulldown assay calculated by the K_D values (Predicted) and measured from the experiments (Actual) are shown.

(B-C) Negative controls for Fig 3F. (B) A mixture of 0.2 µM Cul1^{FAM} and 0.2 µM Cul1^{TAMRA} with or without 0.2 µM Dcn1 was incubated with 0.1 µM each of Nedd8, Ubc12, and NAE for indicated time period. FAM and TAMRA signals were detected by a Typhoon scanner.

(C) 5x Skp1•Skp2 and DKO lysate indicated in Fig 3E was replaced with 0.1 µM each of Nedd8, Ubc12, and NAE, and no FBP was added.

(D) Neddylation promotes the formation of SCF during the exchange process. Cand1, Dcn1 and Cul1•^{GST}Rbx1 were pre-incubated with glutathione beads and then mixed 1:1 (v:v) with protein solution containing Skp1•β-TrCP and Ubc12 or Ubc12~Nedd8. At indicated time points after mixing, beads were washed and eluted, and immobilized proteins were fractionated by SDS-PAGE and detected by WB. Final concentrations of the protein components were the same as in Fig 3G.

(E) Dcn1 stabilizes the Cand1•Cul1•Rbx1 complex in the presence of FBP. Pulldown analysis of recombinant Cand1 (1 µM) bound to recombinant Cul1•^{GST}Rbx1 (0.5 µM) in the presence of Skp1•Skp2 (2 µM) and increasing concentrations of Dcn1 (0-20 µM). Protein samples were fractionated by SDS-PAGE and stained with Coomassie Blue. Normalized levels of Cand1 recovered were calculated as the ratio of Cand1 to ^{GST}Rbx1.

(F) WB estimation of IκBα phosphorylation rate. WT cells were treated with 1 µM MLN4924 for 1 hr to inhibit the ubiquitination and degradation of pIκBα, and then sampled at indicated time points after TNFα treatment. The $t_{1/2}$ of IκBα phosphorylation is estimated to be 14 min.

(G-H) Concentration of endogenous IκBα is 10 times higher than endogenous β-TrCP. WB quantification of the endogenous IκBα (G) and β-TrCP (H) concentrations in WT cells, with recombinant ^{GST}IκBα (G) and ^{GST}β-TrCP (H) spiked into cell lysate as the internal standards. Three biological replicates were analyzed on two individual gels as technical replicates. The concentration of IκBα was estimated to be 650 ± 66 nM (SD, n=6). The concentration of β-TrCP was estimated to be 64 ± 6 nM (SD, n=6). In other experiments, sample titration was performed to confirm that the band intensities measured here were within the linear range of the instrument.

(I-K) pIκBα and β-TrCP form a very stable complex in cells. IP-WB analysis of the dissociation rate of the pIκBα•β-TrCP complex in cell lysate is shown in (I). DKO cell lysate containing 3xFLAG tagged pIκBα with or without added recombinant Skp1ΔΔ•β-TrCP$^{139\text{-}569}$ chase protein (~100x of endogenous β-TrCP level) was incubated at room temperature for indicated times. Dissociation of β-TrCP from pIκBα was calculated as ratios of β-TrCP to pIκBα signals in anti-FLAG IPs, and these ratios were used to estimate k_{off} (J) based on a fit to a single exponential. Lysate input for (I) is shown in (K). The amount of recombinant Skp1ΔΔ•β-TrCP$^{139\text{-}569}$ chase protein added was in large excess of total endogenous Skp1•FBP complexes as judged by relative signals for Skp1 and Skp1ΔΔ. In addition, the level of endogenous β-TrCP in the lysate remained constant throughout a10-hr incubation at room temperature with or without added chase protein.

Figure S4. Detailed reaction scheme of the SCF cycle model (related to Figure 4 and Method S1).

(A) The scheme depicts the state variables and the reactions in the network as listed in Method S1 (Tables T2-T13). Fbox and S denote either Fb1 and S1 (relating to β-TrCP and pIκBα) or Fb2 and S2 (relating to auxiliary substrate receptors and their substrates). Lines with unidirectional arrows represent irreversible reactions. Reactions labeled by the same number (but different lower case letters) have the same kinetic parameters (Tables T3-T13 of Method S1). Note that for better visibility some states are drawn twice in the network.

(B) Reactions describing product inhibition of CSN by unneddylated Cul1 species. We assume that states in which Cul1 is not neddylated and its associated FBP is not bound to substrate, can bind CSN leading to the formation of complexes which are devoid of SCF ligase activity.

(C) Illustration of the detailed balance relations for the thermodynamic cycles involving Cand1 and FBP (lower cycle, $K_1K_4 = K_2K_3$), and Cand1 and Dcn1 (upper cycle , $K_8K_5 = K_3K_9$) (see Method S1 for details).

Figure S5. Parameter identifiability analysis, response matrix, computation of protein fractions and cycle time (related to Figure 4, Figure 7 and Method S1). Experimental tests of the mathematical model predictions (related to Figure 5).

(A) Profile likelihood as a function of estimated parameters (Table T15 of Method S1). Circles were determined by numerically computing the profile likelihood according to Eq. (S10). Red circles represent the optimal parameter values that minimize χ^2 as defined in Eq. (S9). Solid lines are smooth interpolations of the data points. Horizontal dotted lines represent thresholds as defined in Eq. (S11) that were used to derive 95% confidence intervals, either pointwise (lower line) or simultaneous (upper line).

(B) Matrix of response coefficients as defined by Eq. (S12) (see Method S1). Parameters on the horizontal axis were increased by 10% and the relative change of different observable quantities (vertical axis) was computed. Positive / negative response coefficients indicate a positive / negative correlation between parameter and observable quantity. Absolute values larger (smaller) than 1 indicate a high (low) sensitivity with respect to the corresponding parameter. The greater the absolute value of a response coefficient, the more sensitive the respective quantity is to changes in the corresponding parameter. Parameters are defined in Table T15 of Method S1. The abbreviation “b2“ means “bound to“.

(C) The scheme illustrates the computation of the coefficients defined in Eqs. (S13) and (S14) which determine the contribution of the encircled protein complexes to the protein fractions Cand1.b2.Cul1 and Skp1.b2.Cul1 as defined in Table T14 of Method S1. Note that these complexes are unstable (since they contain both Cand1 and FBP), and thus cannot be detected in our pull-down assays. Fb and S may denote Fb1 (β-TrCP) and S1 or Fb2 (auxiliary SRs) and S2.

(D) Illustration of the computation of the cycle time according to Eq. (S21). Concentrations represent steady state concentrations of free (unbound) proteins obtained from simulations using parameters for WT cells (Table T2-T13, T15 of Method S1). Numbers in the table summarize the values of the on and off rate constants as well as the corresponding net rate constants (red color) computed from Eqs. (S15) - (S20).

(E) Confirmation of β-TrCP overproduction in Fig 5C by WB analysis. Fold increase in total β-TrCP levels are indicated. (dark): more intense exposure of β-TrCP blot. A 9-fold increase in total β-TrCP level in both WT and DKO cells was observed in a replicate experiment.

(F) Overexpression of ^{3xFLAG}Cul1 reduces levels of unassembled cellular β-TrCP, Cand1 and Cand2. As depicted in Fig 5D, WT and DKO cells were treated with or without tetracycline to induce expression of a stably integrated ^{3xFLAG}Cul1 transgene, and then lysed in the presence of excess Cul1•^{GST}Rbx1 to capture unassembled β-TrCP, Skp1, Cand1, and Cand2. Lysates were subjected to pulldown with glutathione beads, and bound fractions were subjected to WB with the indicated antibodies. One set of representative results from two replicate experiments are shown. These are the underlying data for the graph in Fig 5E.

(G) Overproduction of β-TrCP modestly reduces the efficiency of its assembly with Cul1. As depicted in Fig 5F, WT and DKO cells with 3xFLAG-tagged endogenous Cul1 were treated with or without tetracycline to induce expression of a stably integrated β-TrCP transgene, and then lysed in the presence of excess Cul1•^{GST}Rbx1 to suppress Cand1-mediated exchange and capture unassembled Skp1•β-TrCP complexes. Lysates were subjected to IP with anti-FLAG followed by pull-down with glutathione beads. Bound fractions were subjected to WB with the indicated antibodies. One set of representative results from two replicate experiments are shown. These are the underlying data for the graph in Fig 5G.

Figure S6. FBP-dependent sequestration of Cul1 inhibits proliferation of DKO cells (related to Figure 6).

(A-B) Fbxo6 overexpression further slows IκBα degradation rate in the DKO cells. These are the underlying data for the graph in Fig 6A. Cells were infected with lentiviruses to overproduce Fbxo6 and were subjected to TNFα treatment three days after the viral infection.

(B) WB analysis of β-TrCP, ^{HA}Fbxo6, and Skp1 in the cell lysates from panel (A). Relative protein levels are indicated below each blot.

(C) Overproduction of ^{HA}Fbxo6 decreases the endogenous SCF$^{β\text{-}TrCP}$. ^{3xFLAG}Cul1 was immunoprecipitated from WT and DKO cells overexpressing ^{HA}Fbxo6 in the presence of recombinant Cul1•^{GST}Rbx1 (+ sponge). Co-immunoprecipitated β-TrCP and ^{HA}Fbxo6 were analyzed by WB.

(D) Overexpression of Fbxo6 alters the morphology of DKO cells. Live cell images were acquired at 20x magnification seven days after viral infection.

(E) WB with anti-Fbxo6 antibody showing ^{HA}Fbxo6 overproduction five days after infection with recombinant lentivirus. The overproduction is estimated to be 45 times of the endogenous level.

(F-I) Co-IP of ^{3xFLAG}Cul1 with overexpressed ^{HA}Fbxo6^{ΔFbox} (F), ^{HA}Fbxl16 (G), ^{HA}Skp2 (H), and ^{HA}Skp2^{ΔLRR} (I) in the presence of recombinant Cul1•^{GST}Rbx1 (+ sponge). Cells were infected by lentiviruses to overexpress different FBPs, and the experimental procedures were similar to Fig 6D. Long (L) and short (S) exposures of endogenous ^{3xFLAG}Cul1 are shown.

(J) Quantification of the relative percent of Cul1 co-immunoprecipitated with overexpressed FBPs in (F-I), n = 2.

Figure S7. FBP expression is dynamic during mouse development (related to Figure 6 and Discussion).

(A) Expression of FBP genes is highly variable during development of multiple tissues, despite stable expression of core SCF components. RNA-seq data from ENCODE for the indicated tissues during mouse development were normalized to ES cell expression levels. Fold change for each embryonic and birth timepoint relative to ES cells is presented in log10 scale. Each datapoint is derived from FPKM RNA-seq values and is the average of two replicates. Grey datapoints and lines represent expression of 73 FBPs, green represents SCF complex components (Cul1, Rbx1, Skp1, Cand1, and Cand2), and black represents the median fold change for all transcripts expressed in ES cells (25130 transcripts).

(B) Expression of many FBPs is highly dynamic during development. RNA-seq data from ENCODE for mouse development was obtained as FPKM values, and averaged for two replicates. For selected FBPs, expression levels relative to total expression of 73 FBPs was calculated for each tissue and timepoint. Distinct colors represent different tissues as listed on the bottom, and bars in the same color represent different embryonic developmental timepoints from early organogenesis (leftmost; timepoint varies by tissue) to birth (rightmost). Tissues with only one timepoint represent gene expression at birth.

METHOD S1: Mathematical model

Protein concentrations (HEK293 cells)

Table T1

protein	**concentration [nM]**	**reference**
Cul1	522	Reitsma et al. 2017
Cand1	1210	
CSN [(a)]	378	
DCN1	325	
Skp1	2107	
Rbx1	1724	
Nedd8 (N8)	3373	
β-TrCP	64	this paper
IκBα	647	this paper

[(a)] average value of CSN1-CSN8 excluding CSN7

Total DCN concentration

In humans there are 5 DCN proteins (DCN1-5) all of which bind to Cul1 with similar affinity [Monda et al. (2013), Keuss et al. (2016)]. In addition, it seems that the 5 DCN proteins are partially functionally redundant so that the effective pool of catalytically active DCN proteins is likely to be larger than the DCN1 pool. To account for this effect in our model we defined the total DCN concentration by

$$[DCN] = f_{DCN1} \cdot [DCN1]. \tag{S1}$$

To estimate the scale factor f_{DCN1} we note that in HeLa cells the total copy number of DCN proteins (DCN1-5) amounts to 256892 of which the sum of DCN1 and DCN2 equals 94931 [Kulak et al., 2014]. Assuming that the concentrations of DCN1 and DCN2 are equal and that the relative proportions of DCN proteins in HEK 293 cells are similar to those in HeLa cells we obtain $f_{DCN1} = 256892/(94931/2) \approx 5.4$ which suggests that $5 \leq f_{DCN1} \leq 6$. In the simulations we used $f_{DCN1} = 6$.

Sequestration of Cand1, CSN and DCN1 by other cullins

Cand1, CSN and DCN1 do not only bind to Cul1 but also to other cullins (Cul2-Cul5) in cullin-RING ubiquitin ligases (CRLs) [Bennett et al., 2010] which reduces the amounts of Cand1, CSN and DCN1 that are available for binding to Cul1. To account for this effect in our model we defined effective Cand1, CSN and DCN1 concentrations through

$$[Cand1]_{eff} = f_{Cand1,WT} \cdot [Cand1] \tag{S2}$$

$$[DCN1]_{eff} = f_{DCN1,WT} \cdot [DCN] \tag{S3}$$

$$[CSN]_{eff} = f_{CSN,WT} \cdot [CSN] \tag{S4}$$

where $[Cand1]$, $[DCN]$ and $[CSN]$ are defined in Table T1 and Eq. (S1). Since DCN proteins bind cullins with similar affinity (within a factor of ~10) [Monda et al. (2013), Keuss et a. (2016)] we assumed that the scale factor $f_{DCN1,WT}$ is proportional to the relative abundance of Cul1, i.e.

$$f_{DCN1,WT} = \frac{[Cul1]}{[Rbx1] + [Cul5]} = \frac{522nM}{1724nM + 548nM} \approx 0.23. \tag{S5}$$

Here we used the concentration of Rbx1 (cf. Table T1) as a measure for the concentration of Cul1-Cul4 all of which form stable heterodimers with Rbx1 [Lydeard et al., 2013]. The concentration of Cul5 was extrapolated from the value reported in [Bennett et al., 2010] according to

$$[Cul5] = \frac{[Cul1]}{[Cul1]_{Bennett}} [Cul5]_{Bennett} \approx \frac{522nM}{302nM} 317nM \approx 548nM.$$

For simplicity, we used the same scale factor for CSN as for DCN defined in Eq. (S5), i.e.

$$f_{CSN,WT} = f_{DCN1,WT} \approx 0.23. \tag{S6}$$

However, previous measurements have shown that if neddylation is inhibited the fraction of Cand1 associated with Cul1 is 0.4/0.75 ≈ 0.54 (Fig. S6 in [Bennett et al., 2010]) suggesting that more than half of the total Cand1 pool is associated with Cul1 under cellular conditions. Hence, we set $f_{Cand1,WT} = 0.54$ in Eq. (S2).

State variables and initial conditions

Table T2 lists the state variables together with their initial values as used in our simulations. F-box proteins (Fb) bind to Cul1 via the Skp1 adaptor protein. Due to the 1:1 stoichiometry between Skp1 and F-box proteins the total concentration of substrate receptors (Skp1•F-box dimers) is bounded by the availability of Skp1 proteins, i.e. [FbT] ≤ [Skp1] = 2107nM. In principle, it is conceivable that the amount of Skp1•F-box heterodimers is lower than the total amount of. However, to reduce the number of unknown parameters that have to be estimated by comparing model simulations with experiments (cf. Parameter estimation) we set [FbT] = [Skp1].

Model reaction and rate constants

We modeled the CRL cycle as a mass-action network. The network states together with the elementary reactions are depicted in Figs. S4A and S4B. The state variables together with their default initial values are defined in Table T2. Reversible reactions were parametrized by k_{on} and k_{off} rate constants while irreversible reactions were parametrized by (pseudo) first-order rate constant. The latter may represent an effective k_{cat} (as for neddylation and deneddylation) or a specific degradation rate (as in the case of substrate degradation). Reactions with the same set of parameters are labelled by the same digit (1-16). Individual reactions within a group of reactions with the same set of parameters are distinguished by a lower case letter (a,b,c,…).

In our model we considered two sets of F-box proteins, β-TrCP (Fb1) and auxiliary (background) substrate receptors (Fb2). In Fig. S4A and S4B only reactions involving Fb1 are shown. For each reaction involving Fb1 or S1 there exists a corresponding reaction for Fb2 or S2 which is listed in the tables below without an explicit reaction number.

Table T2

state variable	**IC**[(a)]	**state variable**	**IC**	**state variable**	**IC**
Cul1[(b)]	522 nM	Cul1•Cand1	0	N8-Cul1•CSN	0
Cand1[(b)]	1210 nM	Cul1•Fb1	0	Cul1•DCN1•Fb1	0
DCN1[(b)]	325 nM	Cul1•Fb2	0	Cul1•DCN1•Fb2	0
CSN[(b)]	378 nM	Cul1•Fb1•S1	0	Cul1•DCN1•Fb1•S1	0
FbT[(c)]	2107 nM	Cul1•Fb2•S2	0	Cul1•DCN1•Fb2•S2	0
Fb1[(b,d)]	64 nM	Cul1•Cand1•Fb1	0	Cul1•Cand1•DCN1	0
Fb2[(e,f)]	2043 nM	Cul1•Cand1•Fb2	0	Cul1•Cand1•DCN1•Fb1	0
Fb1•S1	0	Cul1•Cand1•Fb1•S1	0	Cul1•Cand1•DCN1•Fb2	0
Fb2•S2	0	Cul1•Cand1•Fb2•S2	0	Cul1•Cand1•DCN1•Fb1•S1	0
N8-Cul1	0	N8-Cul1•Fb1	0	Cul1•Cand1•DCN1•Fb2•S2	0
Cul1•DCN1	0	N8-Cul1•Fb2	0	Cul1•Fb1•CSN	0
Cul1•CSN	0	N8-Cul1•Fb1•S1	0	Cul1•Fb2•CSN	0
S1 (IκBα-P)	0	N8-Cul1•Fb2•S2	0	Cul1•DCN1•CSN	0
S2 (auxiliary)	0	N8-Cul1•Fb1•CSN	0	Cul1•DCN1•Fb1•CSN	0
		N8-Cul1•Fb2•CSN	0	Cul1•DCN1•Fb2•CSN	0

[(a)] initial condition, [(b)] measured, [(c)] [FbT] = [Skp1], [(d)] β-TrCP, [(e)] [Fb2] = [FbT] - [Fb1], [(f)] auxiliary substrate receptors

F-box binding to Cul1

The assembly of a functional Skp1•Cul1•F-box (SCF) complex requires binding of a Skp1•F-box heterodimer to Cul1. Here, we did not model the formation of Skp1•F-box dimers explicitly, but considered them as preformed stable entities [Schulman et al., 2009]. In general, there are ~69 different SCF complexes in humans. In our model we considered only two types of Skp1•F-box proteins denoted by Fb1 and Fb2. This allows us to analyze the time scale for the degradation of a specific substrate (mediated by Fb1) in the presence of auxiliary substrate receptors (SRs). The latter compete with Fb1 for access to Cul1, and they are collectively denoted by Fb2.

In a previous study the assembly of ~50 F-box proteins with Cul1 has been quantified under different conditions [Reitsma et al., 2017]. Under normal conditions occupancy ranged from 0% to 70% indicating a highly non-equilibrium steady state *in vivo* that is driven by neddylation, F-box exchange and substrate availability. Even in the absence of neddylation occupancy ranged between 0% and 30% suggesting that there exists some variation in the expression level and/or the binding affinity of Cul1 for different F-box proteins. For the Skp1•Fbxw7 receptor biochemical studies yielded a dissociation constant of 0.225pM which increased by ~6 orders of magnitude to 650nM in the presence of Cand1 [Pierce et al., 2013]. This dramatic increase is mainly driven by a corresponding increase in the k_{off} while the k_{on} remained almost constant. In fact, modulating the off rate constant has been proposed as one of the main mechanisms through which cells may adjust their cellular SCF repertoire [Reitsma et al, 2017].

To allow β-TrCP (Fb1) to exhibit a different binding affinity from background SRs we fix k_{on} at the values obtained for Fbxw7 and express the off rate constants for Fb1 and Fb2 in terms of those for Fbxw7 as

$$k_{off,i}^{Fb1} = f_{Fb1} \cdot k_{off,i}^{Fbxw7} \quad \text{and} \quad k_{off,i}^{Fb2} = f_{Fb2} \cdot k_{off,i}^{Fbxw7}, \quad i = 1,2 \tag{S7}$$

where $k_{off,1}^{Fbxw7} = 9 \cdot 10^{-7} s^{-1}$ and $k_{off,2}^{Fbxw7} = 1.3 s^{-1}$ denote the off rate constants of Skp1•Fbxw7 from the binary and ternary complexes (involving Cand1), respectively [Pierce et al., 2013]. The values of the two scale parameters f_{Fb1} and f_{Fb2} were estimated by comparing model predictions with experiments (cf. Parameter estimation and Table T15).

Table T3

No.	Reactions involving Fb1	k_{on} [(a)] $[(M \cdot s)^{-1}]$	k_{off} $[s^{-1}]$
1	Cul1 + Fb1 ↔ Cul1•Fb1	$4 \cdot 10^6$	$f_{Fb1} \cdot 9 \cdot 10^{-7}$
1a	Cul1•DCN1 + Fb1 ↔ Cul1•DCN1•Fb1		
1b	Cul1 + Fb1•S1 ↔ Cul1•Fb1•S1		
1c	Cul1•DCN1 + Fb1•S1 ↔ Cul1•DCN1•Fb1•S1		
1d	N8-Cul1 + Fb1 ↔ N8-Cul1•Fb1		
1e	N8-Cul1 + Fb1•S1 ↔ N8-Cul1•Fb1•S1		
1f	N8-Cul1•CSN + Fb1 ↔ N8-Cul1•Fb1•CSN		
2	Cul1•Cand1 + Fb1 ↔ Cul1•Cand1•Fb1	$2 \cdot 10^6$	$f_{Fb1} \cdot 1.3$
2a	Cul1•Cand1•DCN1 + Fb1 ↔ Cul1•Cand1•DCN1•Fb1		
2b	Cul1•Cand1 + Fb1•S1 ↔ Cul1•Cand1•Fb1•S1		
2c	Cul1•Cand1•DCN1 + Fb1•S1 ↔ Cul1•Cand1•DCN1•Fb1•S1		

(a) measured for Skp1•Fbxw7 [Pierce et al., 2013]

Table T4

	Reactions involving Fb2	k_{on} $[(M \cdot s)^{-1}]$	k_{off} $[s^{-1}]$
	Cul1 + Fb2 ↔ Cul1•Fb2	$4 \cdot 10^6$	$f_{Fb2} \cdot 9 \cdot 10^{-7}$
	Cul1•DCN1 + Fb2 ↔ Cul1•DCN1•Fb2		
	Cul1 + Fb2•S2 ↔ Cul1•Fb2•S2		
	Cul1•DCN1 + Fb2•S2 ↔ Cul1•DCN1•Fb2•S2		
	N8-Cul1 + Fb2 ↔ N8-Cul1•Fb2		
	N8-Cul1 + Fb2•S2 ↔ N8-Cul1•Fb2•S2		
	N8-Cul1•CSN + Fb2 ↔ N8-Cul1•Fb2•CSN		
	Cul1•Cand1 + Fb2 ↔ Cul1•Cand1•Fb2	$2 \cdot 10^6$	$f_{Fb2} \cdot 1.3$
	Cul1•Cand1•DCN1 + Fb2 ↔ Cul1•Cand1•DCN1•Fb2		
	Cul1•Cand1 + Fb2•S2 ↔ Cul1•Cand1•Fb2•S2		
	Cul1•Cand1•DCN1 + Fb2•S2 ↔ Cul1•Cand1•DCN1•Fb2•S2		

As suggested by our experiments (Fig. 2H) we modeled the assembly of SCF complexes by a random-order binding mechanism (Fig. S4A), i.e. Skp1•F-box receptor proteins may first bind to Cul1 species and then bind substrate or vice versa. In fact, previous simulations indicated that an exchange factor becomes dispensable if binding occurs in a sequential order, i.e. if substrate only binds to F-box proteins if the latter are already bound to Cul1 [Straube et al., 2017].

Cand1 binding to Cul1

The exchange of Skp1•F-box proteins on Cul1 is catalyzed by Cand1 which acts as a substrate receptor exchange factor [Pierce et al. (2013)]. Experiments suggest that Cand1 exerts its catalytic function similar to guanine nucleotide exchange factors, i.e. through formation of a ternary (Cul1•Cand1•Fb) complex. In the absence of Skp1•F-box proteins spontaneous dissociation of Cand1 from a Cul1•Cand1 complex is extremely slow ($k_{off,3} = 10^{-5}s^{-1}$) [Pierce et al. (2013)] but binding of Skp1•F-box to Cul1•Cand1 dramatically increases the dissociation constant for Cand1 in the ternary complex (reaction 4). On thermodynamic grounds (cf. Detailed balance relations) the increase of the dissociation constant for Cand1 upon binding of Skp1•F-box to Cul1•Cand1 must be the same as the increase of the dissociation constant for Skp1•F-box upon binding of Cand1 to Cul1•Skp1•F-box, i.e (cf. Fig. S4C)

$$\frac{K_2}{K_1} = \frac{K_4}{K_3} = \tau \qquad \text{(S8)}$$

where $K_i = k_{off,i}/k_{on,i}$ denotes the dissociation constant of reaction i. Substituting the known values for K_1 $(0.225pM)$ and K_2 $(650nM)$ we obtain $\tau \approx 2.9 \cdot 10^6$ which is comparable with values obtained for GTP/GDP exchange systems [Goody & Hofmann-Goody, 2002].

To compute the remaining dissociation constants we measured the rate constants for the association between Cul1 and Cand1 ($k_{on,3}$) and that between Cul1•Skp1•Skp2 and Cand1 ($k_{on,4}$) (cf. Fig. 1). In this way we obtained $K_3 = 0.5pM$ and (using Eq. S8) $K_4 = (K_2/K_1)K_3 \approx 1.44\mu M$. The latter also determines the dissociation rate constant $k_{off,4}$ as

$$k_{off,4} = k_{on,4} \cdot (K_2/K_1) \cdot K_3 \approx 2.9s^{-1}.$$

Reactions 5 and 6 describe the binding of Cand1 to Cul1 when DCN1 is already bound to Cul1. Our pulldown assay with immobilized DCN1 on GST beads showed (Fig. 3C and 3D) that in the presence of Cand1 the K_D of DCN1 in the ternary Cul1•Cand1•DCN1 complex is reduced by a factor $\alpha = 1/36 = 0.0278$ (cf. Fig. S4C). To ensure that the K_D for Cand1 in the ternary complex is reduced by the same factor we multiplied the k_{off} for reaction 5 and 6 by α and kept k_{on} the same as for reactions 3 and 4 (Table T5).

Substrate binding to F-box protein

We assumed that substrate binds with equal affinity to free Skp1•F-box proteins as well as to Skp1•F-box proteins that are already bound to Cul1 (Cul1•Fb). In general, our model allows for two substrates that may differ in their binding parameters. In particular simulations S1 represents the phosphorylated form of IκBα (IκBα-P) while S2 plays the role of auxiliary (background) substrate which is always present in cells. The off rate constant ($k_{off} {\sim} 10^{-5}s^{-1}$) for the dissociation of IκBα-P from Cul1•β-TrCP•IκBα-P is very small (cf. Fig. S5E) comparable to that for the dissociation of Skp1•F-box from an SCF complex. The on rate constant has not been measured, but is expected to lie between $10^{6} - 10^{7}(M \cdot s)^{-1}$. In the simulations we used the value $k_{on} = 10^{7}(M \cdot s)^{-1}$ for both IκBα-P (S1) and auxiliary substrate (S2). Since the latter represents a mixture of different substrates (the type and amount of which is difficult to quantify for our experimental conditions) we assumed a less extreme value for the off rate constant of S2. The reactions involving S1 and S2 are listed in Table T6 and Table T7, respectively.

Table T5

No.	Reactions	$k_{on}\ [(M \cdot s)^{-1}]$	$k_{off}\ [s^{-1}]$
3	Cul1 + Cand1 ↔ Cul1•Cand1	$2 \cdot 10^{7}$ (a)	10^{-5} (b)
4	Cul1•Fb1 + Cand1 ↔ Cul1•Cand1•Fb1	$2 \cdot 10^{6}$ (a)	2.9 (c)
	Cul1•Fb2 + Cand1 ↔ Cul1•Cand1•Fb2		
4a	Cul1•Fb1•S1 + Cand1 ↔ Cul1•Cand1•Fb1•S1		
	Cul1•Fb2•S2 + Cand1 ↔ Cul1•Cand1•Fb2•S2		
5	Cul1•DCN1 + Cand1 ↔ Cul1•Cand1•DCN1	$2 \cdot 10^{7}$	$\alpha \cdot 10^{-5}$ (d)
6	Cul1•DCN1•Fb1 + Cand1 ↔ Cul1•Cand1•DCN1•Fb1	$2 \cdot 10^{6}$	$\alpha \cdot 2.9$
	Cul1•DCN1•Fb2 + Cand1 ↔ Cul1•Cand1•DCN1•Fb2		
6a	Cul1•DCN1•Fb1•S1 + Cand1 ↔ Cul1•Cand1•DCN1•Fb1•S1		
	Cul1•DCN1•Fb2•S2 + Cand1 ↔ Cul1•Cand1•DCN1•Fb2•S2		

(a) measured (b) measured [Pierce et al., 2013], (c) computed from Eq. (S8), (d) $\alpha = 0.0278$

Table T6

No.	Reactions involving S1	$k_{on}\ [(M \cdot s)^{-1}]$	$k_{off}\ [s^{-1}]$
7	Fb1 + S1 ↔ Fb1•S1	10^{7} (a)	$3.3 \cdot 10^{-5}$ (b)
7a	Cul1•Fb1 + S1 ↔ Cul1•Fb1•S1		
7b	Cul1•Cand1•Fb1 + S1 ↔ Cul1•Cand1•Fb1•S1		
7c	Cul1•DCN1•Fb1 + S1 ↔ Cul1•DCN1•Fb1•S1		
7d	Cul1•Cand1•DCN1•Fb1 + S1 ↔ Cul1•Cand1•DCN1•Fb1•S1		
7e	N8-Cul1•Fb1 + S1 ↔ N8-Cul1•Fb1•S1		

(a) estimated, (b) measured

Table T7

No.	Reactions involving S2	$k_{on}\ [(M \cdot s)^{-1}]$	$k_{off}\ [s^{-1}]$
	Fb2 + S2 ↔ Fb1•S2	10^{7} (a)	0.01 (a)
	Cul1•Fb2 + S2 ↔ Cul1•Fb2•S2		
	Cul1•Cand1•Fb2 + S2 ↔ Cul1•Cand1•Fb2•S2		
	Cul1•DCN1•Fb2 + S2 ↔ Cul1•DCN1•Fb2•S2		
	Cul1•Cand1•DCN1•Fb2 + S2 ↔ Cul1•Cand1•DCN1•Fb2•S2		
	N8-Cul1•Fb2 + S2 ↔ N8-Cul1•Fb2•S2		

(a) estimated

DCN1 binding to Cul1

DCN1 is a scaffold-like E3 ligase which is required for efficient Cul1 neddylation [Kurz et al. (2008)]. Experiments have shown that DCN1 forms a stable ternary complex with Cul1 and Cand1 [Keuss et al. (2016)]. In the absence of Cand1 the K_D for DCN1 binding to Cul1 is comparably low ($1.8\mu M$) [Monda et al. (2013)] while binding of Cand1 increases the affinity of DCN1 to Cul1 36-fold (Fig. 3C and 3D), i.e. the K_D is lowered by a factor $\alpha = 1/36 = 0.0278$ (cf. Cand1 binding to Cul1). To generate a K_D of $1.8\mu M$ we set $k_{on} = 10^6\ (M \cdot s)^{-1}$ and $k_{off} = 1.8\ s^{-1}$ (Table T8). When Cand1 is already bound to Cul1 we keep k_{on}, but lower k_{off} by a factor α.

Table T8

No.	Reactions	$k_{on}\ [(M \cdot s)^{-1}]$	$k_{off}\ [s^{-1}]$
8	Cul1 + DCN1 ↔ Cul1•DCN1	10^6 [(a)]	1.8 [(b)]
8a	Cul1•Fb1 + DCN1 ↔ Cul1•DCN1•Fb1		
	Cul1•Fb2 + DCN1 ↔ Cul1•DCN1•Fb2		
8b	Cul1•Fb1•S1 + DCN1 ↔ Cul1•DCN1•Fb1•S1		
	Cul1•Fb2•S2 + DCN1 ↔ Cul1•DCN1•Fb2•S2		
9	Cul1•Cand1 + DCN1 ↔ Cul1•Cand1•DCN1	10^6	$\alpha \cdot 1.8$ [(c)]
9a	Cul1•Cand1•Fb1 + DCN1 ↔ Cul1•Cand1•DCN1•Fb1		
	Cul1•Cand1•Fb2 + DCN1 ↔ Cul1•Cand1•DCN1•Fb2		
9b	Cul1•Cand1•Fb1•S1 + DCN1 ↔ Cul1•Cand1•DCN1•Fb1•S1		
	Cul1•Cand1•Fb2•S2 + DCN1 ↔ Cul1•Cand1•DCN1•Fb2•S2		

[(a)] estimated, [(b)] adjusted so that $K_D = 1.8\mu M$ [Monda et al. (2013)], [(c)] α=0.0278

Detailed balance relations

The CRL network contains several thermodynamic cycles two of which are depicted in Fig. S4C. Since each of these cycles comprises only of reversible equilibria there must be no net flux in each cycle at steady state. In physical terms, this means that the change in free energy for the formation of the ternary complexes (Cul1•Cand1•Fb and Cul1•Cand1•DCN1) must not depend on the order in which they are formed. This constraint leads to detailed balance relations between the dissociation constants in each cycle, i.e. $K_1 \cdot K_4 = K_2 \cdot K_3$ and $K_3 \cdot K_9 = K_5 \cdot K_8$. A similar relation also holds for the cycle comprising the reactions 4, 6, 8a, and 9a which leads to $K_4 \cdot K_9 = K_8 \cdot K_6$.

Neddylation reactions

Since DCN1 is required for efficient neddylation of Cul1 [Kurz et al. (2008)] and since Cand1 binding and N8 conjugation cannot occur simultaneously [Liu et al., 2002] we assumed that neddylation can only occur from SCF states where DCN1 is bound to Cul1 *and* Cand1 is not bound to Cul1. In general, Nedd8 (N8) conjugation is catalyzed by an associated E2 enzyme (e.g. UBC12) which is recruited to the Rbx1 domain of an SCF complex. However, the rate constants for E2 binding and N8 conjugation are not known. To keep the number of unknown parameters as small as possible we model neddylation by a first order process (Table T9) with effective neddylation rate constant k_{nedd} which is treated as a variable parameter to be estimated from experiments (cf. Table T15). Also, since the concentration of N8 is much larger than that of the other proteins (cf. Table T1) we assumed that N8 is not limiting for the reaction so that it can be absorbed into the definition of the rate constant.

Table T9

No.	Reactions	$k_{nedd}\ [s^{-1}]$
10	Cul1•DCN1 → N8-Cul1 + DCN1	0.268 (a)
10a	Cul1•DCN1•Fb1 → N8-Cul1•Fb1 + DCN1	
	Cul1•DCN1•Fb2 → N8-Cul1•Fb2 + DCN1	
10b	Cul1•DCN1•Fb1•S1 → N8-Cul1•Fb1•S1 + DCN1	
	Cul1•DCN1•Fb2•S2 → N8-Cul1•Fb2•S2 + DCN1	

(a) estimated

Deneddylation reactions

Deneddylation is mediated by the COP9 signalosome (CSN). Consistent with measurements of the rate constants for CSN-mediated deneddylation of N8-Cul1 [Mosadeghi et al. (2016)] we assumed that CSN first binds reversibly to N8-Cul1 and N8-Cul1•Fb (11 and 11a) and, in a second step, N8 is cleaved leading to the dissociation of CSN (12 and 12a).

Table T10

No.	Reactions	$k_{on}\ [(M \cdot s)^{-1}]$	$k_{off}\ [s^{-1}]$	$k_{cat}\ [s^{-1}]$
11	N8-Cul1 + CSN ↔ N8-Cul1•CSN	$2 \cdot 10^7$ (a)	0.032 (a)	
11a	N8-Cul1•Fb1 + CSN ↔ N8-Cul1•Fb1•CSN			
	N8-Cul1•Fb2 + CSN ↔ N8-Cul1•Fb2•CSN			
12	N8-Cul1•CSN → Cul1 + CSN			1.1 (a)
12a	N8-Cul1•Fb1•CSN → Cul1•Fb1 + CSN			
	N8-Cul1•Fb2•CSN → Cul1•Fb2 + CSN			

(a) measured [Mosadeghi et al., 2016]

Product inhibition of CSN

While neddylated Cul1 is a substrate of the CSN deneddylated Cul1 acts as an inhibitor of CSN activity [Mosadeghi et al. (2016)]. CSN binds to both neddylated and deneddylated Cul1, but with different binding affinity. While the k_{on} is the same for both reactions while the k_{off} for CSN in complex with non-neddylated Cul1 is increased by a factor of ~200. Previous biochemical analysis has shown that, in the presence of Cand1 or substrate, the deneddylation rate is reduced [Emberly et al., 2012]. Moreover, addition of substrate impedes stable association of CSN with SCF [Enchev et al., 2012]. Hence, to model product inhibition of CSN we assumed that CSN only binds to Cul1, Cul1•Fb, Cul1•DCN1 and Cul1•DCN1•Fb states (cf. Table T11).

Table T11

No.	Reactions	$k_{on}\ [(M \cdot s)^{-1}]$	$k_{off}\ [s^{-1}]$
13	Cul1 + CSN ↔ Cul1•CSN	$2 \cdot 10^7$ (a)	6.2 (a)
13a	Cul1•Fb1 + CSN ↔ Cul1•Fb1•CSN		
	Cul1•Fb2 + CSN ↔ Cul1•Fb2•CSN		
13b	Cul1•DCN1 + CSN ↔ Cul1•DCN1•CSN		
13c	Cul1•DCN1•Fb1 + CSN ↔ Cul1•DCN1•Fb1•CSN		
	Cul1•DCN1•Fb2 + CSN ↔ Cul1•DCN1•Fb2•CSN		

(a) measured [Mosadeghi et al., 2016]

Substrate degradation

Substrate degradation by itself is a complex process which involves recruitment of Ub-loaded E2 enzyme to the Rbx1 domain of an SCF complex, subsequent multiple Ub transfers to the substrate and processing by the 26S proteasome. Here, we neglected much of this complexity and assumed that once a substrate-bound SCF complex is neddylated the substrate can be degraded. The latter process was described by first order rate constant k_{deg} which summarizes the above mentioned processes in an effective manner (Table T12). Also, for simplicity we assumed that the degradation rate is the same for S1 (IκBα-P) and background substrate S2. For the human 26S proteasome substrate degradation rates range from less than $0.01\ min^{-1}$ up to $0.7\ min^{-1}$ depending on the substrate and the number of conjugated ubiquitins [Lu et al., 2016]. For CyclinB-NT with 4 conjugated ubiquitins the degradation rate is $0.5\ min^{-1}$ or $0.0083\ s^{-1}$. Based on our measurements we estimated $k_{deg} = 0.0071\ s^{-1}$ (cf. Table T15).

Table T12

No.	Reactions	$k_{deg}\ [s^{-1}]$
14	N8-Cul1•Fb1•S1 → N8-Cul1•Fb1	0.0071 (a)
	N8-Cul1•Fb2•S2 → N8-Cul1•Fb2	

(a) estimated

Background substrate

To match simulations with experiments we had to assume that cells contain a certain amount of CRL substrates. Otherwise, it was not possible to generate the high degree of Cul1 neddylation observed experimentally which is consistent with the fact that substrate favors the neddylated state of CRL ligases [Emberly et al., 2012; Enchev et al., 2012]. To generate auxiliary substrate we assumed a constitutive synthesis term (Table T13). Since the total amount of background CRL substrates in the cell is unknown we treated the synthesis rate as a variable parameter to be determined by comparison with experiments (cf. Table T15). In this way we obtained an estimate of 2261nM for the concentration of background substrate under steady state conditions in wildtype cells assuming that substrates are only degraded via the CRL-mediated pathway.

Table T13

No.	reaction	$k_{synth}^{S2}\ [nM \cdot s^{-1}]$
15	Ø → S2	1.4 (a)

(a) estimated

Simulations were done with the Systems Biology Toolbox of MATLAB [MATLAB 2015b] which was used to translate the model reactions (1-15) into a system of ordinary differential equations using mass-action kinetics. Integrations were performed with the implicit solver *ode15s*.

Parameter estimation

To validate our model we measured different quantities in wildtype (WT) cells as well as in response to different genetic perturbations (cf. Table T14). Conditions listed in **bold font** were used to estimate the values of unknown parameters. Altogether, our model comprises 54 state variables and 35 parameters (rate constants, protein concentrations and scale parameters) from which 22 parameters were either known from previous experiments or measured in this work. Among the 13 remaining parameters 8 parameters could be reasonably estimated or constrained leaving only 5 parameters to be fitted by comparing model simulations with experiments. The 4 scale factors P1 – P4 (Table T15) were estimated based on relative protein abundances and previous measurements of the association of Cand1 with different cullins. The 4 on and off rate constants P5 – P8 had almost no effect on the value of the measured quantities (cf. T14 and Fig. S5B), so we fixed them at the indicated values to reduce the number of variable parameters during the fitting procedure.

Table T14 – Experimental conditions and measured quantities

measured quantity	cell type / perturbation / condition	type of experiment	figure
Cul1.b2.Cand1[(a)]	**WT**[(e)] / WT + MLN4924	steady state	4B
Cul1.b2.Skp1[(b)]	WT / WT + MLN4924 / DKO[(f)]	steady state	4B
Cul1.b2.N8[(c)]	**WT** / WT + Cul1 / **DKO** / DKO + Cul1	steady state	4E
β-TrCP.b2.Cul1[(d)]	**WT**	steady state	4D
$t_{1/2}$	**WT** / **DKO** / DKO + Cand1	transient	4C
	WT + β-TrCP / WT + Cul1 / DKO + β-TrCP / DKO + Cul1		4F

[(a)] fraction of Cul1 bound to Cand1, [(b)] fraction of Cul1 bound to Skp1, [(c)] fraction of Cul1 bound to Nedd8, [(d)] fraction of β-TrCP bound to Cul1, [(e)] WT – wildtype, [(f)] DKO – double knockout Cand1$^{-/-}$, Cand2$^{-/-}$

To estimate the values of the 5 remaining parameters in Table T15 (P9-P13) we used nonlinear optimization in combination with a profile likelihood approach as described in [Raue et al., 2009]. To calibrate the model we defined the weighted sum of squared residuals as an objective function

$$\chi^2(\theta) \coloneqq \sum_{k=1}^{6} \frac{\left(y_k - y_k(\theta)\right)^2}{\sigma_k^2} \tag{S9}$$

and numerically determined $\theta = \left(f_{Fb1}, f_{Fb2}, k_{nedd}, k_{deg}, k_{synth}^{S2}\right)$ such that

$$\hat{\theta} = \mathrm{argmin}\,[\chi^2(\theta)].$$

In Eq. (S9) y_k and σ_k^2 denote the values of the measured quantities (cf. T14, bold face) and their respective measurement errors. The quantities $y_k(\theta)$ are the predicted values of the measured quantities obtained from numerical simulations of our model for a particular set of parameter values. Due to limited sample size we were not able to reliably estimate the measurement errors from the data. So, for convenience, we assumed equal variances of $\sigma_k^2 = 0.1 y_k$ (10% from the mean values) for all measurements. However, since all parameters are identifiable (see below) a different choice for the values of the variances would yield qualitatively similar results.

To obtain confidence intervals for the estimated parameter values we numerically computed the profile likelihood for each parameter defined as

$$\chi^2_{PL}(\theta_i) = \min_{\theta_{j\neq i}}[\chi^2(\theta)], \tag{S10}$$

i.e. for each value of θ_i the objective function defined in Eq. (S9) is re-optimized with respect to the remaining parameters $\theta_{j\neq i}$. The resulting plots exhibit a parabolic shape (Fig. S5A) indicating that all parameters are identifiable [Raue et al., 2009]. To obtain finite sample confidence intervals we defined the confidence regions

$$\left\{\theta_i : \chi^2_{PL}(\theta) - \chi^2\left(\hat{\theta}\right) < \Delta_\alpha\right\}, \qquad i = 1, \ldots, 5 \tag{S11}$$

where the threshold $\Delta_\alpha = \chi^2(\alpha, df)$ is the α quantile (confidence level) of the χ^2-distribution with df degrees of freedom. Pointwise confidence intervals are obtained for $df = 1$ while $df = 5$ yields simultaneous confidence intervals for all 5 parameters. Confidence intervals for model predictions (cf. Fig. 4) were computed by running simulations for parameters sampled from the confidence region defined by Eq. (S11) with the threshold $\Delta_\alpha = \chi^2(0.95,5)$ (Fig. S5A, upper horizontal line).

Table T15 – List of estimated parameters

parameter		value	expected range	defined in	fixed / variable
P1	f_{DCN1}	6	$5-6$	Eq. (S1)	fixed
P2 P3	$f_{DCN1,WT}$ $f_{CSN,WT}$	0.23		Eqs. (S2) – (S4)	fixed
P4	$f_{Cand1,WT}$	0.54			fixed
P5	k_{on}^{S1}	$10^7\ (Ms)^{-1}$	$10^6-10^7\ (Ms)^{-1}$	Table T6	fixed
P6	k_{on}^{S2}	$10^7\ (Ms)^{-1}$	$10^6-10^7\ (Ms)^{-1}$	Table T7	fixed
P7	k_{off}^{S2}	$0.01 s^{-1}$	$0.0001-0.01\ s^{-1}$	Table T7	fixed
P8	k_{on}^{DCN1}	$10^6\ (Ms)^{-1}$	$10^6-10^7\ (Ms)^{-1}$	Table T8	fixed
P9	f_{Fb1}	0.247	$0.102-0.490$ (a)	Eq. (S7)	variable
P10	f_{Fb2}	6.514	$2.978-17.461$ (a)	Eq. (S7)	variable
P11	k_{nedd}	$0.268\ s^{-1}$	$0.134\ -0.626\ s^{-1}$ (a)	Table T9	variable
P12	k_{deg}	$0.0071\ s^{-1}$	$0.0055-0.0091\ s^{-1}$ (a)	Table T12	variable
P13	k_{synth}^{S2}	$1.40\ nM \cdot s^{-1}$	$1.09-1.85\ nM \cdot s^{-1}$ (a)	Table T13	variable

(a) simultaneous confidence intervals to a 95% confidence level with 10% assumed measurement errors.

Response coefficients

To quantify how small changes in one of the parameters (P5 – P13) would impact the predicted values for the measured quantities (cf. T14) we computed the matrix of response coefficients (Fig. S5B) according to

$$R_{ij} := \frac{\Delta Q_i / Q_i^{ref}}{\Delta P_j / P_j^{ref}} \tag{S12}$$

where $\Delta P_j = P_j - P_j^{ref}$ denotes the change of parameter P_j relative to a reference value P_j^{ref} and $\Delta Q_i = Q_i - Q_i^{ref}$ represents the corresponding change of the predicted quantity Q_i. Depending on whether Q_i increases or decreases upon a parameter change ΔP_j the response coefficient R_{ij} may be positive or negative, respectively. Its magnitude quantifies the fractional change of Q_i upon a fractional change of P_j. The fact that almost all response coefficients satisfy $|R_{ij}| < 1$ means that our system exhibits only a weak sensitivity to most of the parameters at the respective reference point. This is particularly true for the 4 on and off rate constants P5 – P8 which have almost no effect on the predicted values of the measured quantities except for k_{on}^{DCN} which weakly affects the half-life for substrate degradation in DKO. To reduce the number of fitting parameters we have, therefore, fixed P5 – P8 during parameter estimation.

From the entries of the response matrix for the remaining parameters (P9 – P13) we can make some interesting observations: The fractions of Cul1 bound to Cand1, Skp1 and Nedd8 (first three rows) are mainly determined by the ratio between substrate synthesis (k_{synth}^{S2}) and degradation (k_{deg}). If the substrate synthesis rate is increased the neddylated fraction of Cul1 increases and more Skp1•F-box proteins are recruited to Cul1 leading to a reduction of the fraction of Cul1 associated with Cand1. Increasing k_{deg} has the opposite effect. However, the latter also affects the half-life for IκBα degradation while k_{synth}^{S2} has only a minor effect on $t_{1/2}$. Interestingly the total concentration of Skp1•F-box proteins (FbT) has a strong positive effect on the half-life for IκBα degradation in DKO cells because increasing the total pool of F-box proteins reduces the amount of Cul1 available for binding to β-TrCP.

Protein fractions in terms of state variables

To relate the measured quantities defined in Table T14 to state variables in our model (cf. Table 2) we used the following relations: The fraction of Cul1 bound to Nedd8 was computed as

$$\begin{aligned}\mathrm{Cul1.b2.N8} = {} & \frac{[\text{N8-Cul1}] + [\text{N8-Cul1} \bullet \text{Fb1}] + [\text{N8-Cul1} \bullet \text{Fb2}]}{\mathrm{Cul1_T}} \\ & + \frac{[\text{N8-Cul1} \bullet \text{Fb1} \bullet \text{S1}] + [\text{N8-Cul1} \bullet \text{Fb2} \bullet \text{S2}] + [\text{N8-Cul1} \bullet \text{CSN}]}{\mathrm{Cul1_T}} \\ & + \frac{[\text{N8-Cul1} \bullet \text{Fb1} \bullet \text{CSN}] + [\text{N8-Cul1} \bullet \text{Fb2} \bullet \text{CSN}]}{\mathrm{Cul1_T}}\end{aligned}$$

where $Cul1_T$ denotes the total concentration of Cul1 defined in Table T1. To define the fractions of Cul1 bound to Cand1 (Cul1.b2.Cand1) and Cul1 bound to Skp1•F-box (Cul1.b2.Skp1) we had to take into account that higher-order complexes involving Cand1 and Fb1 or Fb2 are unstable and, thus, cannot be detected in our pull-down assays. For example, the complexes Cul1•Cand1•Fbi•Si would rapidly decay into Cul1•Fbi•Si and Cand1 or Cul1•Cand1 and Fbi•Si (Fig. S5C). The corresponding probabilities are given by

$$a_i = \frac{k_{off,2}^{Si}}{k_{off,2}^{Si} + k_{off,4}} \quad \text{and} \quad b_i = 1 - a_i = \frac{k_{off,4}}{k_{off,2}^{Si} + k_{off,4}}, \quad i = 1,2 \tag{S13}$$

where the rate constants $k_{off,2}^{Si}$ and $k_{off,4}$ are defined in Tables T3-T5. For the decay of complexes involving Cand1, DCN1 and Fb1 or Fb2 we considered three decay channels as the dissociation of Cand1 and DCN1 from Cul1•Cand1•DCN1•Fbi•Si or Cul1•Cand1•DCN1•Fbi occurs with similar rates. The respective probabilities are given by

$$c_i = \frac{k_{off,2}^{Si}}{k_{off,2}^{Si} + k_{off,6} + k_{off,9}}, \quad d_i = \frac{k_{off,6}}{k_{off,2}^{Si} + k_{off,6} + k_{off,9}}, \quad e_i = 1 - (c_i + d_i), \quad i = 1,2 \tag{S14}$$

where the rate constants $k_{off,6}$ and $k_{off,9}$ are defined in Tables T5 and T8, respectively. With the help of these probabilities the protein fractions Cul1.b2.Cand1 and Cul1.b2.Skp1 (which we set equal to Cul1.b2.Fb1+Cul1.b2.Fb2) are defined by

$$\begin{aligned}\mathrm{Cul1.b2.Cand1} = {} & \frac{[\mathrm{Cul1 \bullet Cand1}] + a_1([\mathrm{Cul1 \bullet Cand1 \bullet Fb1}] + [\mathrm{Cul1 \bullet Cand1 \bullet Fb1 \bullet S1}])}{\mathrm{Cul1_T}} \\ & + \frac{a_2([\mathrm{Cul1 \bullet Cand1 \bullet Fb2}] + [\mathrm{Cul1 \bullet Cand1 \bullet Fb2 \bullet S2}]) + [\mathrm{Cul1 \bullet Cand1 \bullet DCN1}]}{\mathrm{Cul1_T}} \\ & + \frac{(a_1 e_1 + c_1)([\mathrm{Cul1 \bullet Cand1 \bullet DCN1 \bullet Fb1}] + [\mathrm{Cul1 \bullet Cand1 \bullet DCN1 \bullet Fb1 \bullet S1}])}{\mathrm{Cul1_T}} \\ & + \frac{(a_2 e_2 + c_2)([\mathrm{Cul1 \bullet Cand1 \bullet DCN1 \bullet Fb2}] + [\mathrm{Cul1 \bullet Cand1 \bullet DCN1 \bullet Fb2 \bullet S2}])}{\mathrm{Cul1_T}}\end{aligned}$$

and

$$\begin{aligned}\mathrm{Cul1.b2.Fbi} = {} & \frac{[\mathrm{Cul1 \bullet Fbi}] + [\mathrm{Cul1 \bullet Fbi \bullet Si}] + [\mathrm{Cul1 \bullet DCN1 \bullet Fbi}]}{\mathrm{Cul1_T}} \\ & + \frac{b_i([\mathrm{Cul1 \bullet Cand1 \bullet Fbi}] + [\mathrm{Cul1 \bullet Cand1 \bullet Fbi \bullet Si}])}{\mathrm{Cul1_T}} \\ & + \frac{(b_i e_i + d_i)([\mathrm{Cul1 \bullet Cand1 \bullet DCN1 \bullet Fbi}] + [\mathrm{Cul1 \bullet Cand1 \bullet DCN1 \bullet Fbi \bullet Si}])}{\mathrm{Cul1_T}} \\ & + \frac{[\mathrm{N8\text{-}Cul1 \bullet Fbi}] + [\mathrm{N8\text{-}Cul1 \bullet Fbi \bullet Si}] + [\mathrm{N8\text{-}Cul1 \bullet Fbi \bullet CSN}]}{\mathrm{Cul1_T}} \\ & + \frac{[\mathrm{Cul1 \bullet DCN1 \bullet Fbi \bullet CSN}] + [\mathrm{Cul1 \bullet Fbi \bullet CSN}] + [\mathrm{Cul1 \bullet DCN1 \bullet Fbi \bullet Si}]}{\mathrm{Cul1_T}}\end{aligned}$$

for $i = 1,2$. The fraction of β-TrCP bound to Cul1 (β-TrCP.b2.Cul1) is given by

$$\mathrm{\beta\text{-}TrCP.b2.Cul1} = \mathrm{Cul1.b2.Fb1}\,\frac{\mathrm{Cul1_T}}{\mathrm{Fb1_T}}$$

where $\mathrm{Fb1_T}$ equals the total β-TrCP concentration listed in Table T1.

Simulation protocols

To simulate IκBα degradation of we started simulations from steady state by adding the reaction

No.	reaction	$k_{phos}\ [s^{-1}]$	initial condition
16	IκBα → IκBα-P (S1)	$\ln(2)/(60 \cdot 14)$	[IκBα]=647nM

which describes the phosphorylation of IκBα by IκBα kinase. Phosphorylated IκBα (IκBα-P) is generated with a half-life of 14min serving as a substrate of the SCF$^{\beta\text{-TrCP}}$ ligase ($\mathrm{Cul1} \bullet \mathrm{Fb1}$).

To simulate the conditions and perturbations listed in Table T14 we used the protocols defined in Table T16. Inhibition of Nedd8 conjugation as well as Cand1$^{-/-}$, Cand2$^{-/-}$ double knockout were simulated by setting the neddylation rate constant and the total Cand1 concentration to zero, respectively. To simulate Cul1 overexpression we computed a scale factor assuming that Cul1 competes with other cullins for access to Rbx1. Similarly, to simulate β-TrCP overexpression we computed a scale factor assuming that β-TrCP competes with auxiliary SRs for access to Skp1. In the case of Cul1 overexpression we also had to recompute the scale factors that account for sequestration of DCN1, CSN and Cand1 by other cullins. In both cases the overexpression factors (f_{Cul1} and $f_{\beta\text{-TrCP}}$) account for both endogenous and exogenous proteins.

Table T16

perturbation	protocol	remark
WT + MLN4924	set $k_{nedd} = 0$ at $t = 0$	Inhibition of Nedd8 conjugation
DKO	set $[Cand1] = 0$ at $t = 0$	Cand1$^{-/-}$, Cand2$^{-/-}$ double knockout
WT / DKO + Cul1	set $[Cul1]_{OE} = f_{OE,Cul1} \cdot {[Cul1]_{WT}}^{(a)}$ with $${f_{OE,Cul1}}^{(b)} = \frac{f_{Cul1}[Rbx1]}{[Rbx1] + (f_{Cul1} - 1)[Cul1]_{WT}}$$ and recompute scale factors in Eqs. (S2) – (S4) $${f_{DCN1,OE}}^{(c)} = \frac{[Cul1]_{OE}}{[Cul1]_{OE} + [Rbx1] - [Cul1]_{WT} + [Cul5]}$$ $${f_{Cand1,OE}}^{(d)} = min\left(1, f_{Cand1,WT}\frac{f_{DCN1,OE}}{f_{DCN1,WT}}\right)$$	Cul1 overexpression in WT or DKO
WT / DKO + β-TrCP	set $[Fb1]_{OE} = f_{OE,\beta\text{-TrCP}} \cdot {[Fb1]_{WT}}^{(e)}$ with $${f_{OE,\beta\text{-TrCP}}}^{(f)} = \frac{f_{\beta\text{-TrCP}}[FbT]_{WT}}{[FbT]_{WT} + \left(f_{\beta\text{-TrCP}} - 1\right)[Fb1]_{WT}}$$ set $[FbT]_{OE} = [FbT]_{WT} - [Fb1]_{OE}$	β-TrCP overexpression in WT or DKO

(a) $[Cul1]_{WT} = 522nM$, (b) $f_{Cul1} = 6.6$ in WT and $f_{Cul1} = 5$ in DKO, (c) $f_{CSN,OE} = f_{DCN1,OE}$, (d) not applicable in DKO, (e) $[Fb1]_{WT} = 64nM$, (f) $f_{\beta\text{-TrCP}} = 5.5$ in WT and $f_{\beta\text{-TrCP}} = 8$ in DKO, $[FbT]_{WT} = 2107nM$

Computation of the cycle time

To compute the cycle time for the cyclic reaction chain depicted in Fig. 7 we assigned to each reversible reaction an effective forward rate constant using the concept of net rate constants [Cleland, 1975]. The latter are denoted by $k_1,\ldots,k_6$ in Fig. S5D (highlighted in red color). For irreversible reactions such as neddylation (k_{10}) and deneddylation (k_{12}) the net rate constant is identical with the rate constant. Then the net rate constant k_6 is given by

$$k_6 = k_{on,11}[CSN]\frac{k_{12}}{k_{12}+k_{off,11}} \tag{S15}$$

where $[CSN] = 82nM$ denotes the concentration of free (unbound) CSN under steady state conditions (with [S1]=0). The other 5 net rate constants are defined recursively as

$$k_5 = k_{off,6}\frac{k_{10}}{k_{10}+k_{on,6}[Cand1]} \tag{S16}$$

$$k_4 = k_{on,2}([Fb1]+[Fb2]+[Fb2 \bullet S2])\frac{k_5}{k_5+k_{off,2}} \tag{S17}$$

$$k_3 = k_{on,9}[DCN1]\frac{k_4}{k_4+k_{off,9}} \tag{S18}$$

$$k_2 = k_{off,2}\frac{k_3}{k_3+k_{on,2}[Fb1]} \tag{S19}$$

$$k_1 = k_{on,4}[Cand1]\frac{k_2}{k_2+k_{off,4}}. \tag{S20}$$

The concentrations for Cand1, Fb1 (β-TrCP), Fb2 (auxiliary SR), Fb2•S2 and DCN1 are steady state concentrations that were obtained by integrating the model equations using the parameter set for WT cells (Tables T2-T13, T15) without substrate for Fb1. Note that in Eq. (S14) the factor in front of the fraction represents the effective “on rate” for binding of any free Skp1•F-box protein to Cul1•Cand1•DCN1 while in Eq. (S16) we used the on rate for binding of a particular F-box protein (Fb1) to bind to Cul1•Cand1. Combining the expressions in Eq. (S15) – (S20) yields the cycle time

$$t_{cycle} = \frac{1}{k_1}+\frac{1}{k_2}+\frac{1}{k_3}+\frac{1}{k_4}+\frac{1}{k_5}+\frac{1}{k_6}+\frac{1}{k_{10}}+\frac{1}{k_{12}}. \tag{S21}$$